

INFORMATION TO USERS

This was produced from a copy of a document sent to us for microfilming. While the most advanced technological means to photograph and reproduce this document have been used, the quality is heavily dependent upon the quality of the material submitted.

The following explanation of techniques is provided to help you understand markings or notations which may appear on this reproduction.

- 1. The sign or "target" for pages apparently lacking from the document photographed is "Missing Page(s)". If it was possible to obtain the missing page(s) or section, they are spliced into the film along with adjacent pages. This may have necessitated cutting through an image and duplicating adjacent pages to assure you of complete continuity.**
- 2. When an image on the film is obliterated with a round black mark it is an indication that the film inspector noticed either blurred copy because of movement during exposure, or duplicate copy. Unless we meant to delete copyrighted materials that should not have been filmed, you will find a good image of the page in the adjacent frame.**
- 3. When a map, drawing or chart, etc., is part of the material being photographed the photographer has followed a definite method in "sectioning" the material. It is customary to begin filming at the upper left hand corner of a large sheet and to continue from left to right in equal sections with small overlaps. If necessary, sectioning is continued again—beginning below the first row and continuing on until complete.**
- 4. For any illustrations that cannot be reproduced satisfactorily by xerography, photographic prints can be purchased at additional cost and tipped into your xerographic copy. Requests can be made to our Dissertations Customer Services Department.**
- 5. Some pages in any document may have indistinct print. In all cases we have filmed the best available copy.**

**University
Microfilms
International**

300 N. ZEEB ROAD, ANN ARBOR, MI 48106
18 BEDFORD ROW, LONDON WC1R 4EJ, ENGLAND

8008515

RANA, INAM ELAHI

THEORY AND DESIGN OF PRINTED ANTENNAS

University of California, Los Angeles

PH.D.

1979

University
Microfilms
International

300 N. Zeeb Road, Ann Arbor, MI 48106

18 Bedford Row, London WC1R 4EJ, England

PLEASE NOTE:

In all cases this material has been filmed in the best possible way from the available copy. Problems encountered with this document have been identified here with a check mark ✓.

1. Glossy photographs _____
2. Colored illustrations _____
3. Photographs with dark background _____
4. Illustrations are poor copy _____
5. Print shows through as there is text on both sides of page _____
6. Indistinct, broken or small print on several pages _____ throughout

7. Tightly bound copy with print lost in spine _____
8. Computer printout pages with indistinct print ✓ _____
9. Page(s) _____ lacking when material received, and not available from school or author _____
10. Page(s) _____ seem to be missing in numbering only as text follows _____
11. Poor carbon copy _____
12. Not original copy, several pages with blurred type _____
13. Appendix pages are poor copy _____
14. Original copy with light type _____
15. Curling and wrinkled pages _____
16. Other _____

University
Microfilms
International

300 N. ZEEB RD., ANN ARBOR MI 48106 (313) 761-4700

Reproduced with permission of the copyright owner. Further reproduction prohibited without permission.

UNIVERSITY OF CALIFORNIA
Los Angeles

Theory and Design
of
Printed Antennas

A dissertation submitted in partial satisfaction of the
requirements for the degree Doctor of Philosophy
in Engineering

by

Inam Elahi Rana

1979

The dissertation of Inam Elahi Rana is approved.

John M. Dawson
John M. Dawson

Robert S. Elliott
Robert S. Elliott

Stanley J. Osher
Stanley J. Osher

Cavour W. Yeh
Cavour W. Yeh

Nicolaos G. Alexopoulos
Nicolaos G. Alexopoulos, Committee Chairman

University of California, Los Angeles

1979

بِسْمِ اللَّهِ الرَّحْمَنِ الرَّحِيمِ

In the name of ALLAH, Most Gracious, Most Merciful.

TABLE OF CONTENTS

	<u>Page</u>
LIST OF SYMBOLS.....	vi
LIST OF TABLES.....	x
LIST OF FIGURES.....	xi
ACKNOWLEDGEMENT.....	xv
VITA.....	xvi
ABSTRACT OF THE DISSERTATION.....	xviii
CHAPTER I: INTRODUCTION.....	1
CHAPTER II: PRINTED WIRE DIPOLE.....	6
2.1 GREEN'S FUNCTION.....	8
2.2 CURRENT DISTRIBUTION OVER PRINTED WIRE DIPOLE.....	15
2.3 EVALUATION OF THE SOMMERFELD TYPE INTEGRALS.....	19
2.4 INPUT IMPEDANCE.....	26
2.5 RADIATION PATTERN.....	27
2.6 NUMERICAL RESULTS.....	28
CHAPTER III: PRINTED ARRAY PARAMETERS.....	42
3.1 CURRENT DISTRIBUTION OVER A PAIR OF PARALLEL PRINTED DIPOLES.....	42
3.2 MUTUAL IMPEDANCE COMPUTATIONS.....	45
3.3 FIELD EXCITED BY A PRINTED DIPOLE ALONG AIR DIELECTRIC INTERFACE.....	46
3.4 NUMERICAL RESULTS.....	49
CHAPTER IV: PRINTED PARASITIC ARRAYS.....	69
4.1 PRINTED YAGI-UDA ARRAY.....	70
4.2 COLLINEAR ARRAY.....	82

Table of Contents (continued)

	Page
4.3 THE MICROSTRIP PATCH.....	86
4.4 FURTHER APPLICATIONS.....	90
CHAPTER V: CONCLUSIONS.....	92
BIBLIOGRAPHY.....	94
APPENDIX A: INTEGRAL REPRESENTATION OF Π_{xi}	98
APPENDIX B: SOMMERFELD'S PROOF.....	101
APPENDIX C: REDUCTION OF POCKLINGTON'S EQUATION (33) USING SINUSOIDAL EXPANSION FUNCTIONS TO THE FORM (38) ...	105
APPENDIX D: PRINCIPAL VALUE INTEGRATION.....	110
APPENDIX E: TWO SURFACE WAVE MODES.....	114
APPENDIX F: TAIL CONTRIBUTION OF INTEGRALS (39) AND (40) 116	
APPENDIX G: FAR ZONE FIELDS.....	120
APPENDIX H: DYADIC GREEN'S FUNCTION.....	124
APPENDIX I: COMPUTER PROGRAM FOR CURRENT DISTRIBUTION AND INPUT IMPEDANCE OF A PRINTED WIRE DIPOLE.....	126
APPENDIX J: COMPUTER PROGRAM FOR MUTUAL IMPEDANCE BETWEEN TWO PRINTED DIPOLES.....	146

LIST OF SYMBOLS

a	radius of the wire
A	constant defined by (52)
$A(\theta)$	array factor
A_f	magnitude of array factor for $\theta=-45^\circ$
A_b	magnitude of array factor for $\theta=+45^\circ$
A_{\min}	minimum magnitude of the array factor
B	thickness of the substrate
C	integration constant
D	displacement between two dipoles in echelon configuration as defined in Fig. 23
$D_e(\lambda)$	factor defining TE modes of surface waves
$D_m(\lambda)$	factor defining TM modes of surface waves
$D_e(\theta, \phi)$	factor defined by (G.7) for $\theta=\alpha$
$D_m(\theta, \phi)$	factor defined by (G.8) for $\theta=\alpha$
E_x	x component of the electric field
E_θ, E_ϕ	far zone components of the electric field
F(λ)	amplitude coefficient of the x component of Hertz vector \bar{H} scattered from the substrate
$F_e(\lambda)$	amplitude coefficient of the x component of Hertz vector \bar{H}_e transmitted into the substrate
f(λ)	function defined by (D.15)
f(λ_0)	function defined by (D.16)
G	separation between two dipoles in collinear configuration as defined in Fig. 19
$\bar{G}(r, r')$	dyadic Green's function

G_x , G_y	vector Green's functions for Hertzian dipoles oriented in \hat{x} and \hat{y} directions, respectively
$H_0(x)$, $H_1(x)$	Hankel functions of zeroth and first order
I_{in}	input current of the printed dipole as shown in Fig. 2 for 1.0 volt input excitation
I_x	integral defined by (59)
$I(x')$	current distribution on a printed dipole
I_1	input current of dipole #1 as shown in Fig. 14
I_2	current flowing across the short circuited input terminals of dipole #2 as shown in Fig. 14
\bar{J}	vector current density of source in region I
J_e	vector current density of source in region II
$J_0(x)$, $J_1(x)$	Bessel functions of zeroth and first order
k	wave number for free space
k_e	wave number for dielectric medium
L	length of the printed dipole
L_1	length of driven dipole as defined in Fig. 14
L_2	length of parasitic dipole as defined in Fig. 14
$Ln(x)$	natural Logarithmic function
L_{dir}	length of the director dipole in λ_0
L_{exc}	length of the exciter dipole in λ_0
L_{ref}	length of the reflector dipole in λ_0
L_r	resonant length of the printed dipole
N	number of segments of the printed dipole
N_1	number of segments of the driven dipole
N_2	number of segments of the parasitic dipole

P_1	pulse function as defined in Section 3.1
P_2	pulse function as defined in Section 3.1
P_i	pulse function as defined in Appendix C
P_{C_1}	position vector defined in Section 4.3
P_{τ_1}	position vector defined in Section 4.3
r_1, r_2	distances defined in Fig. 3
R, X	resistive and reactive parts of input impedance
R_{12}, X_{12}	resistive and reactive parts of mutual impedance
XL, XT, XC	constants defined in Appendix E
x, y, z	coordinates of the field point
x', y', z'	coordinates of the source point
$\hat{x}, \hat{y}, \hat{z}$	unit vectors defining a cartesian coordinate system
Z_{in}	input impedance of the printed dipole
Z_{12}	mutual impedance between two printed dipoles
Z_{11}	input impedance of driven dipole when parasitic dipole is open circuited
$\bar{\Pi}_s$	Hertz vector of the wave scattered from the substrate
$\bar{\Pi}_e$	Hertz vector of the wave transmitted into the substrate
Π_{xs}	x component of Hertz vector $\bar{\Pi}_s$
Π_{zs}	z component of Hertz vector $\bar{\Pi}_s$
Π_{xe}	x component of Hertz vector $\bar{\Pi}_e$
Π_{ze}	z component of Hertz vector $\bar{\Pi}_e$
μ	radical factor defined by $\mu = \sqrt{\lambda^2 - k^2}$

ρ, ϕ, z	coordinates of a point in cylindrical coordinate system
r, ϕ, θ	coordinates of a point in spherical coordinate system
θ_1, θ_2	angles defined in Fig. 3
$\delta(y')$	Dirac delta function
λ	integration variable
λ_0	free space wavelength
θ_{\min}	angle corresponding to the minimum value of $A(\theta)$
ω	angular frequency
μ_0	permeability of free space
ϵ_0	permittivity of free space
ϵ_r	relativity permittivity of the substrate
Φ	scalar potential function
$\Phi(\lambda)$	amplitude coefficient of the z component of Hertz vector, scattered from the substrate
$\Phi_e(\lambda)$	amplitude coefficient of the z component of Hertz vector, transmitted into the sustrate

LIST OF TABLES

Number	Title	Page
I	Printed dipole parameters for different values of B and ϵ_r	35
II	Front to back ratio for different values of displacement d.....	73

LIST OF FIGURES

Number	Title	Page
1.	Hertzian Dipole on a Grounded Substrate geometry.	7
2.	Printed Wire Dipole geometry.....	14
3.	Complex λ -plane geometry.....	21
4.	Path of Integration.....	22
5.	Current Distribution on a Printed Wire Dipole Re[I] and Im[I] vs x (in λ_0), ($B=0.1016\lambda_0, \epsilon_r=3.25$) ..	29
6.	Current Distribution on a Printed Wire Dipole Re[I] and Im[I] vs x (in λ_0), ($B=0.1016\lambda_0, \epsilon_r=1.0$) ..	30
7.	Current Distribution on a Printed Wire Dipole Re[I] and Im[I] vs x (in λ_0), ($B=0.127\lambda_0, \epsilon_r=3.25$) ..	32
8.	Current Distribution on a Printed Wire Dipole Re[I] and Im[I] vs x (in λ_0), ($B=0.15\lambda_0, \epsilon_r=8.5$)	33
9.	Input Impedance of a Printed Wire Dipole vs L (in λ_0), ($B=0.1016\lambda_0, \epsilon_r=3.25, a=0.00005\lambda_0$).....	36
10.	Input Impedance of a Printed Wire Dipole vs L (in λ_0), ($B=0.127\lambda_0, \epsilon_r=3.25, a=0.00005\lambda_0$).....	37
11.	Input Impedance of a Printed Wire Dipole vs L (in λ_0), ($B=0.15\lambda_0, \epsilon_r=8.5, a=0.000025\lambda_0$).....	38
12.	E-plane Radiation plot of a Printed Wire Dipole, ($L=0.333\lambda_0, B=0.1016\lambda_0, \epsilon_r=3.25$)	40
13	H-plane Radiation plot of a Printed Wire Dipole, ($L=0.333\lambda_0, B=0.1016\lambda_0, \epsilon_r=3.25$)	41
14.	A Printed Wire Dipole pair (Driven and Parasitic)	43

List of Figures (continued)

Number	Title	Page
15.	Electric Flux Lines emanating from Printed Wire Dipole (plan view).....	48
16.	Mutual Impedance between two Broadside Dipoles vs S (in λ_0), ($L=0.33\lambda_0, B=0.1016\lambda_0, \epsilon_r=3.25$).....	51
17.	Mutual Impedance between two Broadside Dipoles vs S (in λ_0), ($L=0.417\lambda_0, B=0.1016\lambda_0, \epsilon_r=3.25$).....	52
18.	Mutual Impedance between two Broadside Dipoles vs S (in λ_0), ($L=0.5\lambda_0, B=0.1016\lambda_0, \epsilon_r=3.25$).....	53
19.	Mutual Impedance between two Collinear Dipoles vs G (in λ_0), ($L=0.25\lambda_0, B=0.1016\lambda_0, \epsilon_r=3.25$).....	54
20.	Mutual Impedance between two Collinear Dipoles vs G (in λ_0), ($L=0.33\lambda_0, B=0.1016\lambda_0, \epsilon_r=3.25$).....	55
21.	Mutual Impedance between two Collinear Dipoles vs G (in λ_0), ($L=0.417\lambda_0, B=0.1016\lambda_0, \epsilon_r=3.25$).....	56
22.	Mutual Impedance between two Collinear Dipoles vs G (in λ_0), ($L=0.417\lambda_0, B=0.1016\lambda_0, \epsilon_r=1.0$).....	57
23.	Mutual Impedance between two Dipoles in Echelon vs D (in λ_0), ($L=0.33\lambda_0, B=0.1016\lambda_0, \epsilon_r=3.25, S=0.25\lambda_0$).	58
24.	Mutual Impedance between two Dipoles in Echelon vs D (in λ_0), ($L=0.417\lambda_0, B=0.1016\lambda_0, \epsilon_r=3.25, S=0.25\lambda_0$).	59
24.	Mutual Impedance between two Dipoles in Echelon vs D (in λ_0), ($L=0.5\lambda_0, B=0.1016\lambda_0, \epsilon_r=3.25, S=0.25\lambda_0$)...	60
26.	Mutual Impedance between two Collinear Dipoles vs G (in λ_0), ($L=0.3\lambda_0, B=0.127\lambda_0, \epsilon_r=3.25$).....	62

List of Figures (continued)

Number	Title	Page
27.	Mutual Impedance between two Collinear Dipoles vs G (in λ_0), ($L=0.4\lambda_0$, $B=0.127\lambda_0$, $\epsilon_r=3.25$)	63
28.	Mutual Impedance between two Collinear Dipoles vs G (in λ_0), ($L=0.25\lambda_0$, $B=0.15\lambda_0$, $\epsilon_r=8.5$)	64
29.	Mutual Impedance between two Collinear Dipoles vs G (in λ_0), ($L=0.3\lambda_0$, $B=0.15\lambda_0$, $\epsilon_r=8.5$)	65
30.	Mutual Impedance between two Broadside Dipoles vs S (in λ_0), ($L=0.25\lambda_0$, $B=0.15\lambda_0$, $\epsilon_r=8.5$)	67
31.	Mutual Impedance between two Broadside Dipoles vs S (in λ_0), ($L=0.3\lambda_0$, $B=0.15\lambda_0$, $\epsilon_r=8.5$)	68
32.	Driven and Parasitic Dipole pair.....	71
33.	H-plane Radiation Pattern of a Dipole Parasitic pair $0.1\lambda_0$ distance apart, ($L=0.333\lambda_0$, $B=0.1016\lambda_0$, $\epsilon_r=3.25$)	75
34.	Current Distribution on 3-element Printed Yagi- Uda Array vs x (in λ_0), ($B=0.1016\lambda_0$, $\epsilon_r=3.25$)	77
35.	Radiation Pattern of 3-element Printed Yagi-Uda Array, ($B=0.1016\lambda_0$, $\epsilon_r=3.25$)	78
36.	Radiation Pattern of 4-element Printed Yagi-Uda Array, ($B=0.1016\lambda_0$, $\epsilon_r=3.25$)	80
37.a	Vector Diagram of Single Director Yagi Array.....	81
37.b	Vector Diagram of Double Director Yagi Array.....	81
38.	Collinear Array and its Radiation Pattern, ($L=0.3\lambda_0$, $B=0.127\lambda_0$, $\epsilon_r=3.25$)	83

List of Figures (continued)

Number	Title	Page
39.	Current Distribution on Collinear Dipole Array....	85
40.	Adjacent Triangles with common side BC.....	88
41.	Printed Patch Antenna approximated by Triangular Patches.....	88
42.	Path of Integration for Integral (D.1).....	112

ACKNOWLEDGEMENT

"Praise be to Allah, Lord of the worlds, the Beneficient, the Merciful," Who enabled the author to complete this research work.

The author wishes his sincere gratitude to Professor Alexopoulos for proposing the topic and for his encouragement which greatly aided the author in completing this research.

The author's thanks are also due to Suparco, Karachi, Pakistan which financially supported a part of the study program.

The author also likes to thank the U.S. Army contract no: DAAG29-79-C-0050 for partially supporting the research.

I would also like to thank Professors J.M. Dawson, R.S. Elliott, S.J. Osher and C.W. Yeh for serving on my committee.

Lastly, but not the least, I am highly indebted to my parents who have been a constant source of encouragement during this period.

VITA

December 14, 1949--Born, Pasrur, Pakistan

1973--B.Sc., Electrical Engineering (Commun. & Electronics)
University of Engineering and Technology Lahore,
Pakistan

1975--1976--Assistant Engineer Suparco, Karachi, Pakistan

1976--1977--Suparco Fellowship

1977--M.S., University of California, Los Angeles

1978--1979--Teaching Assistant, Department of Electrical
Sciences and Engineering, UCLA

PUBLICATIONS

Rana, I.E. and Alexopoulos, N.G. "On the Current Distribution
on Printed Parasitic Thin Wire Arrays," Digest of
National Radio Science Meeting, University of Washington,
Seattle, Washington, June 18-22, 1979.

Alexopoulos, N.G. and Rana, I.E. "On the Solution to
Pocklington's Equation for Antennas Printed on Grounded
Substrate," IEEE AP International Symposium Digest, June
18-22, 1979.

Alexopoulos, N.G. Uzunoglu, N.K. and Rana, I.E. "Radiation
by Microstrip Patches," IEEE AP International Symposium

Digest, June 18-22, 1979.

Rana, I.E. and Alexopoulos, N.G. "On Theory of Printed Wire
Antennas," 9th European Microwave Conference, Brighton
England, sept. 17-21, 1979.

Rana, I.E. and Alexopoulos, N.G. "Printed Wire Antennas,"
Printed Circuit Antennas Technology Workshop, Oct. 17-19
1979, Las Cruces, New Mexico.

ABSTRACT OF THE DISSERTATION

Theory and Design of Printed Antennas

by

Inam Elahi Rana

Doctor of Philosophy in Engineering

University of California, Los Angeles, 1979

Professor Nicolaos G. Alexopoulos, Chairman

This dissertation deals with the theory and design of antennas printed on a grounded substrate. A Green's function approach has been employed which involves improper Sommerfeld integrals. By considering Pocklington's integral equation with proper choice of expansion and testing functions, solution for current distribution and input impedance is obtained, with resulting proper but slowly convergent integrals. The integrals are evaluated by a real axis integration technique which involves analytical and numerical steps.

As an example printed wire antenna is analyzed. Numerical results illustrating the effect of substrate thickness and dielectric constant on the current distribution and input impedance are presented herein.

An array of printed wire dipoles is also considered. The pertinent array parameters, such as, current distribution, input impedance and mutual impedance are computed. An extensive discussion on the surface waves

generation and their role in determining mutual impedance characteristic is undertaken and it has been shown that in collinear configuration mutual coupling is dominantly due to surface waves. Computations for mutual impedance between dipoles in broadside, collinear and echelon arrangements are presented. These results could be used in designing printed dipole arrays.

Next, attention is directed to parasitic arrays, such as Printed Yagi-Uda array and Printed Collinear array. A procedure is laid out for designing Printed Yagi-Uda array. Lastly, the methodology is extended which enables one to analyze Microstrip Patch Antennas also.

Chapter I

INTRODUCTION

Printed (also known as microstrip) antennas play an increasingly important role in aerospace technology because they offer many advantages, such as light weight, low cost and negligible volume. They are also naturally adaptive for operation in a conformal environment.

The radiation characteristics of this class of antennas have been analyzed for certain geometries by several authors. Munson [1] developed a transmission line model for use in designing rectangular microstrip patch antennas. Howell [2] gave a qualitative description of the square and circular disc microstrip antennas using a dielectric loaded cavity model. Derneryd [3] modelled the rectangular patch representing it as two slots separated by a low impedance line. Recently Lo, Solomon and Richards [4] have extended the cavity model to other microstrip antennas, such as circular segment, as well as the ring and elliptical shapes. All the aforementioned authors used the resonant cavity model. To retain the validity of the model, the thickness of the substrate is assumed small compared to the wavelength λ in the substrate. This assumption implies that the antenna is (a) a good resonator rather than a good radiator (low radiation efficiency), (b) narrow in bandwidth and (c) low power. To improve the radiation efficiency, bandwidth and power handling capability, the substrate thickness should be

increased. In such a case, the resonator model does not show agreement between theory and experiment. The resonator model does not take into account either the radiated power or the power launched in the dielectric guide as surface waves. The surface waves are significant in the determination of some of the antenna characteristics, notably antenna current distribution and input impedance.

Agrawal and Bailey [5], in their effort to solve the microstrip antenna problem, adopted an experimental and numerical technique. They experimented to find the amount of fractional shift in the resonance frequency and the reflection coefficient at resonance from the unloaded to the infinitely loaded (antenna immersed in the dielectric medium) case. Making use of the wire grid modelling technique, they modelled the patch antenna in an infinite dielectric medium, and modified the results to account for finite dielectric discontinuity. This technique involves experimental investigations which are troublesome and expensive.

An attempt to solve the microstrip dipole problem was carried out by Uzunolgu, Alexopoulos and Fikioris [6], who employed a Green's function approach. They used a two dimensional plane wave spectrum analysis which resulted in an expensive two dimensional numerical integration technique. Furthermore, they assumed a sinusoidal current distribution over the antenna which gave first order

results. These results are valid when the substrate is exceedingly small as compared to the wavelength in the dielectric medium and more generally when the microstrip dipole is resonant.

Most of the work reported so far has been concentrated on single microstrip elements. However, some workers made ingenious attempts to design microstrip arrays. James and Hall [7] designed a microstrip array using open circuited microstrip lines as radiating elements. Derneryd [8] and William [9] used microstrip patches and dipoles as radiating elements, respectively. The basic assumption undertaken by all of them is that the surface wave coupling is negligible. James and Hall [7], however, pointed out that surface waves can provide an unwanted source of coupling between the distant part of the microstrip array and also a source of ill defined radiation. This is because the surface wave is a guided mode of the structure and decays slowly. Therefore, ignoring the presence of the surface wave in an array design may lead to crude results.

There is a need for an exact analysis and a design technique which can shed light on the printed dipole antenna properties and will establish rules for optimum design. Therefore, in this dissertation, a methodology is presented which can treat in general the area of printed antennas and in particular printed dipole or wire antennas, including arrays. In the following, a step by step exposition of the

methodology for the design of printed wire antenna and printed wire arrays is given.

The Green's function which takes into account the dielectric air boundary as well as the radiation condition at infinity is developed in Section 2.1 by solving the problem of a printed horizontal Hertzian dipole. The obtained Green's function is in terms of Sommerfeld integrals and their derivatives are improper in nature.

The formulation of the integral equation for the unknown current distribution $I(x)$ is presented in Section 2.2. The integral equation is solved by method of moments [10]. With proper choice of expansion functions the resulting Green's function integrals become proper, but slowly convergent. The success of this method depends upon an efficient evaluation of the Green's function. A real axis analytical numerical technique is presented in Section 2.3, which computes the Green's function very efficiently. Numerical results followed by discussion conclude Chapter II.

Mutual impedance is a very important design parameter for a printed array design. This topic is discussed in Chapter III. Computations for dipoles in broadside, echelon and collinear arrangements are presented. These computations yield physical insight into the surface wave propagation. Many useful results are inferred from them and are discussed in this chapter.

Application to practical problems such as a printed Yagi-Uda array and a printed Collinear array are investigated in Chapter IV.

Chapter II

PRINTED WIRE DIPOLE

This chapter presents a technique which is applicable to the study of the printed antennas. Specific application of this method is made to the printed wire dipole antenna.

The method relies on the development of the Green's function for the horizontal Hertzian dipole which takes into account the air dielectric boundary while satisfying the radiation condition. The obtained Green's function is in terms of Sommerfeld integrals; these integrals are slowly convergent, and their derivatives are improper integrals in nature. An efficient numerical-analytical integration technique has been developed which computes the Green's function for all distances from the source. The E-type integral equation is formulated for unknown antenna current distribution. Solution of this integral equation is obtained using method of moments which yield evaluation of the current distribution and the input impedance of the printed dipole.

Next, the stationary phase method is used to develop a formula for the radiated fields of the printed dipole antenna. Computations based on this formula lead to the E-plane and H-plane plots of the antenna. Numerical results illustrating the effect of the dielectric constant and thickness of the substrate on the current distribution and input impedance are presented in the concluding section of

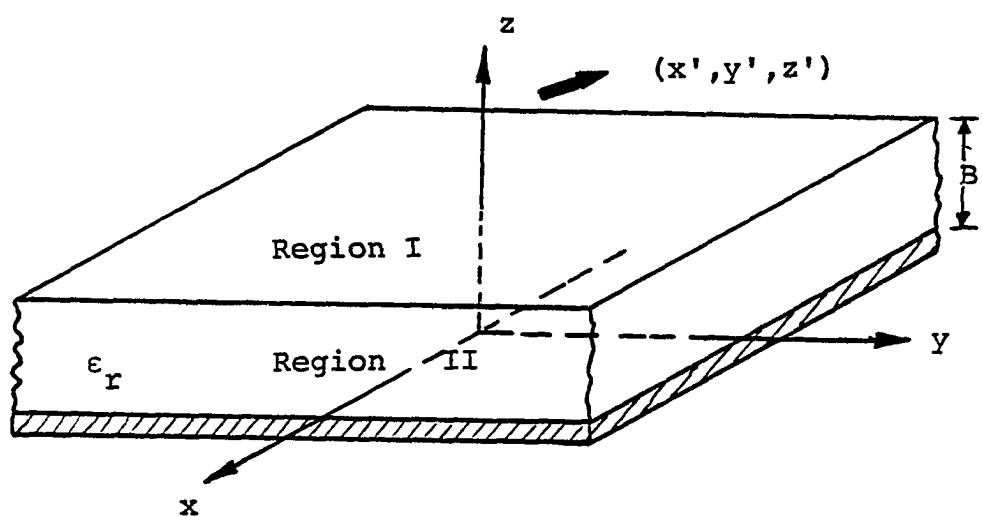


Fig. 1. Hertzian Dipole on a Grounded Substrate geometry

this chapter.

2.1 GREEN'S FUNCTION:

A horizontal Hertzian dipole, as shown in Fig. 1, is held at point (x',y',z') over a grounded dielectric substrate of thickness B . The substrate has relative permittivity ϵ_r which may be complex to account for loss. Assuming $\exp(-j\omega t)$ time dependency Maxwell's equations for region I (i.e., $z>B$), can be written as,

$$\nabla \times \bar{E} = j\omega\mu_0\bar{H} \quad (1.a)$$

$$\nabla \times \bar{H} = \bar{J} - j\omega\epsilon_0\bar{E} \quad (1.b)$$

$$\nabla \cdot \bar{E} = \rho/\epsilon_0 \quad (1.c)$$

$$\nabla \cdot \bar{H} = 0 \quad (1.d)$$

where \bar{J}, ρ are sources in region I.

Defining a vector potential function $\bar{\Pi}$ as follows,

$$\bar{H} = -j\omega\epsilon_0\nabla \times \bar{\Pi} \quad (2)$$

and since $\nabla \cdot \nabla \times \bar{\Pi} = 0$, (1.d) is satisfied. By substituting (2) into the curl equation for \bar{E} one obtains,

$$\nabla \times (\bar{E} - \omega^2\mu_0\epsilon_0\bar{\Pi}) = 0 \quad .$$

Since $\nabla \times \nabla \Phi = 0$, the above result can be integrated at once to give,

$$\bar{E} = \omega^2\mu_0\epsilon_0\bar{\Pi} - \nabla\Phi \quad (3)$$

where Φ is the scalar potential function.

So far, two of Maxwell's equations are satisfied. It remains to find the relation between Φ and \bar{H} , and the condition on them so that the remaining equations are also satisfied.

The curl equation for \bar{H} gives,

$$\nabla \times \nabla \times \bar{H} = \nabla \nabla \cdot \bar{H} - \nabla^2 \bar{H} = \frac{\bar{J}}{j\omega\epsilon_0} + \omega^2\epsilon_0\mu_0\bar{H} - \nabla\Phi. \quad (4)$$

Since Φ and \bar{H} are arbitrary, therefore let

$$\nabla \cdot \bar{H} = -\Phi. \quad (5)$$

This is known as the Lorentz condition. Using (5), (4) reduces to

$$\nabla^2 \bar{H} + k^2 \bar{H} = \frac{\bar{J}}{j\omega\epsilon_0}, \quad (6)$$

where $k = \omega\sqrt{\epsilon_0\mu_0}$, is the free space wave number.

Making use of (3) and (5) in order to satisfy the divergence equation for \bar{E} , the result is,

$$\nabla^2 \Phi + k^2 \Phi = -\frac{\bar{J}}{\epsilon_0}. \quad (7)$$

Using the Lorentz condition, the fields may be written in terms of vector potential \bar{H} alone as follows,

$$\bar{E} = k^2 \bar{H} + \nabla \nabla \cdot \bar{H} \quad (8)$$

$$\bar{H} = -j\omega\epsilon_0 \nabla \times \bar{H} \quad (9)$$

where \bar{H} is the solution of the inhomogeneous equation (6) for a known source current distribution, \bar{J} , in homogeneous region I. The solution for the unbounded region is given by

$$\bar{H} = \frac{1}{j\omega\epsilon_0} \int_V \bar{J}(x', y', z') \cdot \frac{e^{-jk|r-r'|}}{|r-r'|} dv'. \quad (10)$$

Equations (1) through (10) are also valid for region II ($0 < z < B$) if the free space permittivity ϵ_r is replaced by the permittivity of the dielectric medium $\epsilon_r \epsilon_0$. However, since the substrate is a nonmagnetic dielectric material, its permeability remains the same as for free space, i.e. μ_0 . The field equations for region II are,

$$\mathbf{E} = k_e^2 \bar{\mathbf{A}}_e + \nabla \times \bar{\mathbf{H}}_e \quad (11)$$

and

$$\bar{\mathbf{H}} = -j\omega \epsilon_0 \epsilon \nabla \times \bar{\mathbf{A}}_e. \quad (12)$$

In these equations, $\bar{\mathbf{A}}_e$ is the vector potential for region II and it satisfies,

$$\nabla^2 \bar{\mathbf{A}}_e + k_e^2 \bar{\mathbf{A}}_e = \frac{\bar{\mathbf{J}}_e}{j\omega \epsilon_0 \epsilon}, \quad (13)$$

where $\bar{\mathbf{J}}_e$ is the current distribution inside the substrate and $k_e = \omega/\sqrt{\mu_0 \epsilon_0 \epsilon_r}$ is the wave number for region II.

Now the pertinent Green's function is developed. A Hertzian dipole is considered in region I ($\bar{\mathbf{J}}_e = 0$, no sources in the substrate), and it is oriented in the x-axis direction. The Hertzian source is expressed as,

$$\bar{\mathbf{J}} \cdot d\mathbf{V} = \delta(\mathbf{r} - \mathbf{r}') \cdot \hat{\mathbf{x}}, \quad (14)$$

where the dipole moment is assumed unity, i.e., $\mathbf{M}_d = 1$.

Substituting the above equation in (10), one obtains,

$$\bar{\mathbf{A}} = \frac{1}{j\omega \epsilon_0} \frac{e^{-jk|\mathbf{r}-\mathbf{r}'|}}{|\mathbf{r}-\mathbf{r}'|} \quad (15)$$

This is known as the Hertz vector potential $\bar{\mathbf{A}}$, which is the solution of (6) for the Hertzian source. This solution

can be transformed into cylindrical co-ordinates, which are more convenient for the geometry of the problem (see Appendix A). The incident wave on the substrate is given by,

$$\Pi_{xi} = u \int_0^{\infty} J_0(\rho\lambda) \cdot e^{-\mu|z-z'|} \frac{\lambda d\lambda}{\mu}, \quad (15)$$

where $u = \frac{1}{j\omega 4\pi \epsilon_0}$, $\rho = \sqrt{(x-x')^2 + (y-y')^2}$ and $\mu = \sqrt{\lambda^2 - k^2}$.

Sommerfeld [11] has shown that the Hertzian vector of the scattered wave from the substrate and the transmitted wave into the substrate must have a z component as well as an x component (the proof is reproduced in Appendix B). The Hertz vector of the scattered and the transmitted waves in their respective regions are,

$$\begin{aligned}\bar{\Pi}_s &= \Pi_{xs} \hat{x} + \Pi_{zs} \hat{z} & z > B \\ \bar{\Pi}_e &= \Pi_{xe} \hat{x} + \Pi_{ze} \hat{z} & 0 < z < B\end{aligned}$$

respectively.

The x and z components of these vectors are expressible in the form,

$$\Pi_{xs} = u \int_0^{\infty} J_0(\rho\lambda) \cdot F(\lambda) \cdot e^{-j\mu(z+z')} \lambda d\lambda \quad (16)$$

$$\Pi_{zs} = u \cdot \cos\phi \int_0^{\infty} J_1(\rho\lambda) \cdot \Phi(\lambda) \cdot e^{-\mu(z+z')} \lambda^2 d\lambda \quad (17)$$

$$\Pi_{xe} = u \int_0^{\infty} J_0(\rho\lambda) \cdot F_e(\lambda) \cdot e^{-j\mu z'} \sinh\mu_e z \cdot \lambda d\lambda \quad (18)$$

and

$$\Pi_{ze} = u \cdot \cos\phi \int_0^\infty J_1(\rho\lambda) \cdot \Phi_e(\lambda) \cdot e^{-j\mu z'} \cosh \mu_e z \cdot \lambda^2 d\lambda. \quad (19)$$

The parameters $F(\lambda)$, $F_e(\lambda)$, $\Phi(\lambda)$ and $\Phi_e(\lambda)$ are unknown coefficients to be determined by matching the boundary conditions at the air-dielectric interface $z=B$. The choice of $\cosh \mu_e z$ and $\sinh \mu_e z$ is such that the boundary conditions [11] at $z=0$,

$$\Pi_{xe} = 0, \quad \frac{\partial \Pi_{xe}}{\partial z} = 0, \quad (20)$$

are satisfied.

The boundary conditions for the air dielectric interface are [11],

$$\Pi_x = n^2 \Pi_{xe}, \quad (21.a)$$

$$\Pi_z = n^2 \Pi_{ze}, \quad (21.b)$$

$$\frac{\partial \Pi_x}{\partial z} = n^2 \frac{\partial \Pi_{xe}}{\partial z} \quad (21.c)$$

$$\text{and } \frac{\partial \Pi_z}{\partial z} - \frac{\partial \Pi_{ze}}{\partial z} = \frac{\partial \Pi_{xe}}{\partial x} - \frac{\partial \Pi_x}{\partial x}, \quad (21.d)$$

where $\Pi_x = \Pi_{xi} + \Pi_{xs}$ and $\Pi_z = \Pi_{zs}$.

By making use of equations (21.a) through (21.d) the unknown coefficients can be obtained, i.e.,

$$F(\lambda) = \frac{(\mu - \mu_e \coth \mu_e B)}{(\mu + \mu_e \coth \mu_e B)} e^{2\mu B} \quad (22)$$

$$F_e(\lambda) = \frac{2 \cdot \operatorname{cosech} \mu_e B}{n^2 (\mu + \mu_e \coth \mu_e B)} e^{\mu B} \quad (23)$$

$$\Phi(\lambda) = \frac{2(1 - n^2)}{(\mu + \mu_e \coth \mu_e B) \cdot (\mu n^2 + \mu_e \tanh \mu_e B)} e^{2\mu B} \quad (24)$$

and

$$\Phi_e(\lambda) = \frac{(1 - n^2) \cdot \operatorname{sech} \mu_e B}{n^2 (\mu + \mu_e \coth \mu_e B) \cdot (\mu n^2 + \mu_e \tanh \mu_e B)} e^{\mu B}. \quad (25)$$

When these results are substituted in (16) through (19) and collected with (15), the Green's function for a horizontal electric dipole at $z' = B$, i.e. on the substrate is obtained as,

$$\Pi_x = 2 \cdot u \int_0^\infty J_0(\rho \lambda) \cdot e^{-\mu(z+z'-2B)} \cdot \frac{\lambda d\lambda}{D_e(\lambda)}, \quad (26)$$

$$\Pi_z = 2 \cdot u(1-n^2) \int_0^\infty J_1(\rho \lambda) \cdot e^{-\mu(z+z'-2B)} \cdot \frac{\cos \phi \cdot \lambda^2 d\lambda}{D_e(\lambda) \cdot D_m(\lambda)}, \quad (27)$$

$$\Pi_{xe} = \frac{2 \cdot u}{n^2} \int_0^\infty J_0(\rho \lambda) \cdot e^{-\mu(z'-B)} \cdot \frac{\sinh \mu_e z \cdot \lambda d\lambda}{\sinh \mu_e B \cdot D_e(\lambda)} \quad (28)$$

and

$$\Pi_{ze} = \frac{2 \cdot u(1-n^2)}{n^2} \int_0^\infty J_1(\rho \lambda) \cdot e^{-\mu(z'-B)} \cdot \frac{\cosh \mu_e z \cdot \lambda^2 d\lambda}{\cosh \mu_e B \cdot D_e(\lambda) \cdot D_m(\lambda)}, \quad (29)$$

where

$$D_e(\lambda) = \mu + \mu_e \coth \mu_e B \quad (30)$$

and

$$D_m(\lambda) = \mu n^2 + \mu_e \tanh \mu_e B. \quad (31)$$

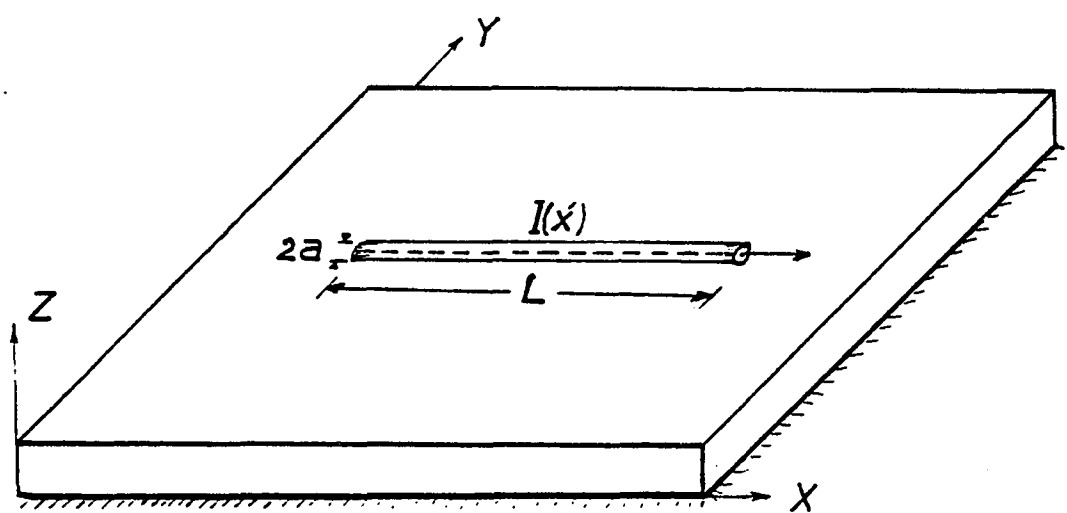


Fig. 2. Printed Wire Dipole Geometry

2.2 CURRENT DISTRIBUTION OVER A PRINTED WIRE DIPOLE:

A thin wire dipole of length L and diameter $2a$, printed on a grounded substrate, is shown in Fig. 2. It is assumed that the radius of the wire is very small as compared to the free space wavelength ($a \ll \lambda_0$), and therefore the thin wire approximation can be used. The current on the wire does not have circumferential symmetry, due to the presence of the grounded substrate. The antenna current may have a circumferential component in addition to the axial component, yet for a thin wire only the axial component is of significance. As shown by Tulyathan and Newman [12], only the axial component is dominant in the determination of the radiation and impedance characteristics. It follows that the thin wire approximation which computes mainly the axial current component is a valid approximation.

The axial component of the electric field at any point (x, y, z) due to a source of lineal current density $J(x', y', z')\hat{x}$ is given by (8) i.e.,

$$E_x(x, y, z) = \int_{V'} J(x', y', z') \hat{x} \cdot \left[k^2 + \nabla \nabla \cdot \right] \bar{H} \hat{x} dV'. \quad (32)$$

For a printed wire dipole, the current density $J(x', y', z')$ can be expressed as,

$$J(x', y', z') = I(x') \cdot \delta(y') \cdot \delta(z' - B),$$

where $I(x')$ is the net dipole current at any point on the wire.

Substituting the above equation in (32) and simplifying, one obtains the axial component of the electric field, $E_x(x,y,z)$, due to the wire current $I(x')$ as,

$$E_x(x,y,z) = \int_L I(x') \cdot \left[k^2 \Pi_x + \frac{\partial^2 \Pi_x}{\partial x^2} + \frac{\partial^2 \Pi_z}{\partial x \partial z} \right] dx', \quad (33)$$

where

$$\Pi_x = 2 \cdot u \int_0^\infty J_0(\rho \lambda) \cdot e^{-\mu(z-B)} \frac{\lambda d\lambda}{D_e(\lambda)} \quad (34)$$

and

$$\Pi_z = 2 \cdot u(1-n^2) \int_0^\infty J_1(\rho \lambda) \cdot e^{-\mu(z-B)} \frac{\cos \phi \cdot \lambda^2 d\lambda}{D_e(\lambda) \cdot D_m(\lambda)} \quad (35)$$

with $\rho = \sqrt{(x-x')^2 + (y-y')^2}$.

Equation (33) is known as Pocklington's Equation in which the unknown antenna current $I(x')$ is under the integral sign. The wire antenna is unloaded at the ends, hence the antenna current must satisfy the following boundary conditions,

$$I(0) = I(L) = 0. \quad (36)$$

In order to solve (33) for the antenna current $I(x')$, the method of moments [10] is used. Accordingly, the wire is divided into N equal segments. As it is usual in method of moments, the proper choice of current expansion functions must be made. The sinusoidal expansion functions offer many advantages [13], [14], and have been used by many authors [15], [16]. The advantages are: (1) boundary conditions (36) for the antenna current $I(x')$ are

automatically satisfied; (2) a closed form expression for the fields is obtained and as will be shown latter, (3) the improprieness in the Green's function integrals is removed as $z \rightarrow B$. The form of the i th expansion function centered about x_i is simply,

$$I(x') = \begin{cases} \frac{\sin k(d - |x' - x_i|)}{\sin kd} & |x' - x_i| \leq d \\ 0 & \text{otherwise.} \end{cases} \quad (37)$$

where d is the length of each wire segment given by,

$$d = L/N.$$

Substituting the $N-1$ term current expansion series into (33), and by making use of $\frac{\partial}{\partial x} = -\frac{\partial}{\partial x}$, identity, it can be shown (Appendix C), that the x component of the electric field \bar{E} is given at any point (x, y, B) on the substrate by,

$$\begin{aligned} E_x(x, y, B) = & \frac{k}{\sin kd} \sum_{i=2}^N I_i \left[\Pi_x \Big|_{x_{i-1}} + \Pi_x \Big|_{x_{i+1}} - 2 \cdot \cos kd \cdot \Pi_x \Big|_{x_i} + \right. \\ & 2 \cdot \cos kd \left[\Pi_x \Big|_{x_i} - \Pi_x \Big|_{x_{i-1}} - \Pi_x \Big|_{x_{i+1}} + k \left[\int_{x_{i-1}}^{x_i} \sin k(x' - x_{i-1}) \cdot \Pi \cdot dx' + \right. \right. \\ & \left. \left. \int_{x_i}^{x_{i+1}} \sin k(x_{i+1} - x') \cdot \Pi \cdot dx' \right] \right], \end{aligned} \quad (38)$$

where

$$\Pi_x = 2 \cdot u \int_0^\infty J_0(\rho \lambda) \cdot e^{-\mu(z-B)} \frac{\lambda d\lambda}{D_e(\lambda)} \quad (39)$$

$\lim_{z \rightarrow B}$

and

$$\Pi = 2 \cdot (n^2 - 1) \cdot u \int_0^\infty J_0(\rho\lambda) \cdot e^{-\mu(z-B)} \frac{\lambda \mu d\lambda}{D_e(\lambda) \cdot D_m(\lambda)} \quad (40)$$

$\lim_{z \rightarrow B}$

$$\text{with } \rho = \sqrt{(x-x')^2 + y^2}.$$

Note that (38) does not involve derivatives of Π_x and Π_z . These derivatives yield improper integrals for $z=B$. Furthermore, the expression for E_x is in closed form, as it involves integrals (39) and (40), which are convergent in nature.

For numerical convergence, sinusoidal functions have also been chosen as testing functions. This choice of the functions is equivalent to the reaction concept [17] and the variational method [18]. Therefore each side of (38) is multiplied by the testing functions given by (37), with the subscript i replaced by j and variable x' by x . The integration with respect to x reduces the problem to the matrix form,

$$[v] = [I][z] \quad (41)$$

where I is related to the currents on the subsections and V to the electromagnetic excitation column. Depending upon the feeding point, the corresponding excitation voltage is set to unity in the excitation column.

Matrix inversion is a simple process for high speed computers, and hence the current distribution can be determined once a well conditioned impedance matrix $[z]$ is

obtained. The ease and speed of evaluation of the matrix elements is of considerable importance. Evaluation of the matrix elements involves calculation of the following integrals,

$$I_1 = \int_{x_{j-1}}^{x_j} \sin k(x-x_{j-1}) \cdot \Pi_x dx + \int_{x_j}^{x_{j+1}} \sin k(x_{j+1}-x) \cdot \Pi_x dx \quad (42)$$

$$I_2 = \int_{x_{j-1}}^{x_j} \sin k(x-x_{j-1}) \cdot dx \left[\int_{x_{i-1}}^{x_i} \sin k(x'-x_{i-1}) \cdot \Pi \cdot dx' + \int_{x_i}^{x_{i+1}} \sin k(x_{i+1}-x') \cdot \Pi \cdot dx' \right] + \int_{x_j}^{x_{j+1}} \sin k(x_{j+1}-x) \cdot dx \left[\int_{x_{i-1}}^{x_i} \sin k(x'-x_{i-1}) \cdot \Pi \cdot dx' + \int_{x_i}^{x_{i+1}} \sin k(x_{i+1}-x') \cdot \Pi \cdot dx' \right] \quad (43)$$

where Π_x and Π are the integrals defined by (39) and (40).

The double integration with respect to x and x' is performed very efficiently by a numerical technique which makes use of the overlapping nature of the Green's function and removes redundancy in the calculation of the integrand. The integrals (39) and (40) are of the Sommerfeld type; they require special treatment which is described in the next section.

2.3 EVALUATION OF THE SOMMERFELD TYPE INTEGRALS:

Integrals (39) and (40) are written in the form,

$$\Pi_x = 2 \cdot u \int_0^\infty J_0(\lambda \rho) \cdot \frac{e^{-\mu(z-B)} \lambda d\lambda}{(\mu + \mu_e \coth \mu_e B)}$$
(44)

$$\Pi = 2 \cdot (1 - n^2) \int_0^\infty J_0(\rho \lambda) \cdot \frac{e^{-\mu(z-B)} \mu \lambda d\lambda}{(\mu + \mu_e \coth \mu_e B) \cdot (\mu_e n^2 + \mu_e \tanh \mu_e B)}$$
(45)

where $\mu = \sqrt{\lambda^2 - k^2}$ and $\mu_e = \sqrt{\lambda^2 - n^2 k^2}$.

Note that the integrands contain two radicals $\mu = \sqrt{\lambda^2 - k^2}$ and $\mu_e = \sqrt{\lambda^2 - k^2 n^2}$ which are double valued functions of the complex variable λ . However, the sign of the radical μ_e does not effect the single-valuedness of the integrands, as the terms involving the radical μ_e are even functions. Therefore, the branch points contributed by the radical μ are only considered. In order that the integrals represent a field solution properly, the integrand must be single-valued all along the path of integration. This is accomplished by drawing branch cuts through the branch points $\lambda = \pm k$. The choice of the branch cuts is arbitrary as far as single valuedness is concerned; however, the convergence of the integrals is another matter. The convergence of the integrals and outgoing wave propagating character require,

$$\operatorname{Re}[\lambda] > 0$$

and (47)

$$\operatorname{Im}[\lambda] < 0$$

respectively.

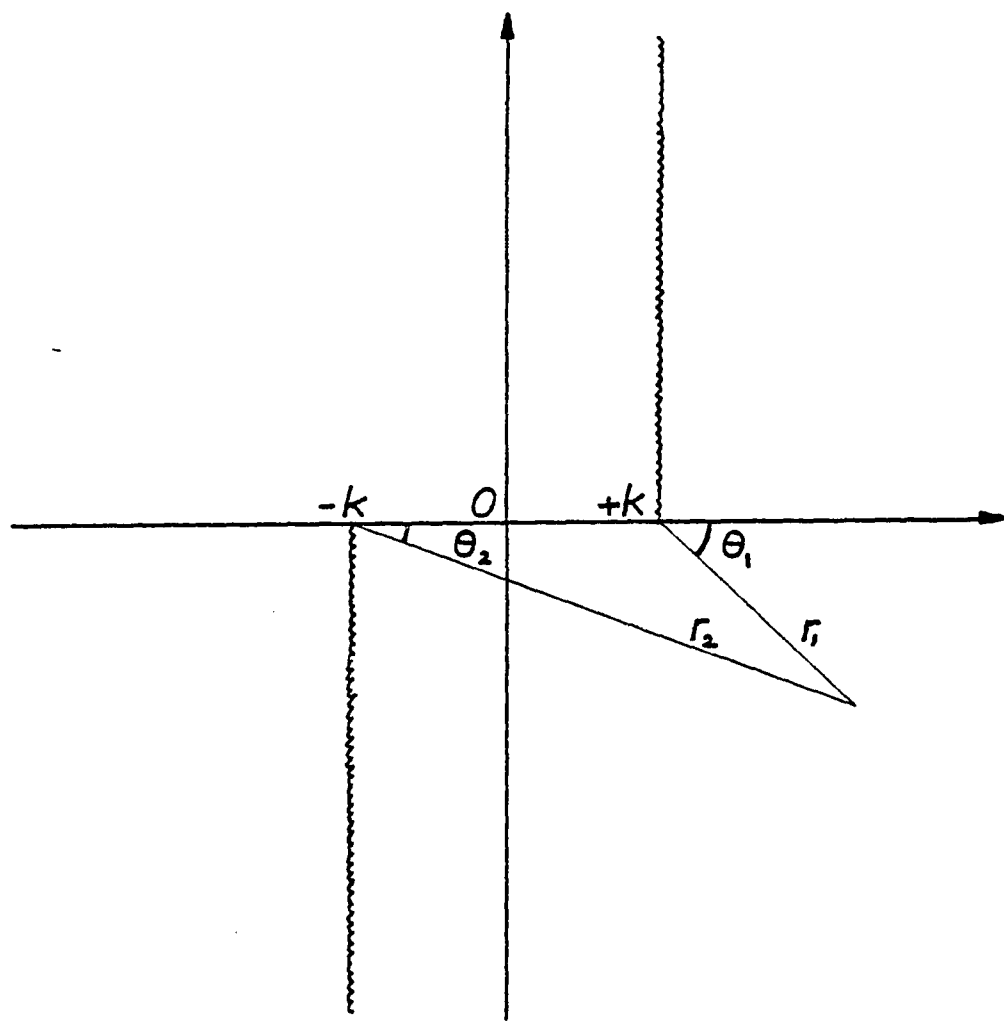


Fig. 3 Complex λ -plane Geometry

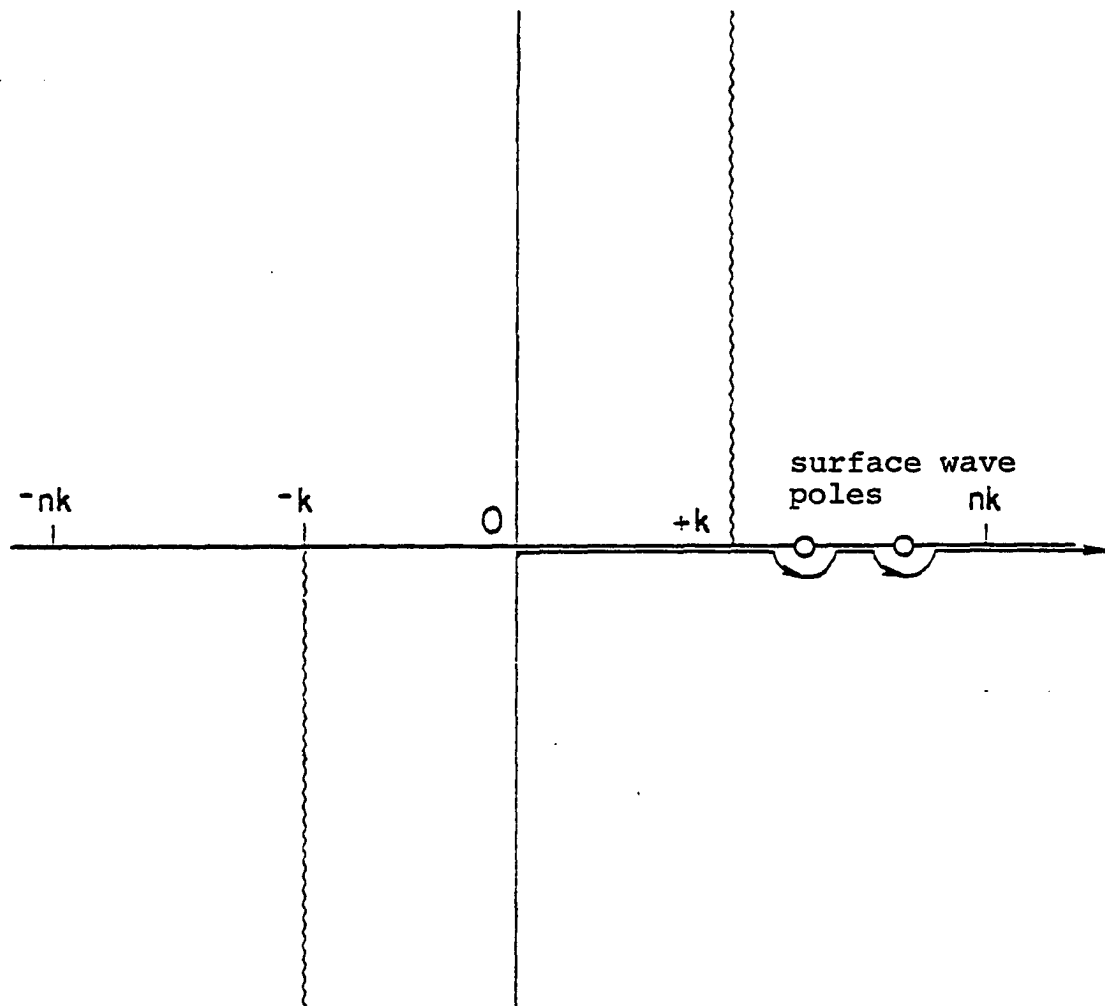


Fig. 4. Path of Integration

The choice of the branch cuts is governed by these two conditions. One possible construction of the branch cuts is shown in Fig. 3. μ can be written as,

$$\mu = r_1 r_2 e^{j(\theta_1 + \theta_2)/2} . \quad (48)$$

Then for all points in the complex λ -plane such that $\text{Re}[\lambda] > k$ and $\text{Im}[\lambda] < 0$, $\theta_1 < 0^\circ$ and $\theta_2 < 0^\circ$. Therefore it follows from (48) that $\text{Re}[\lambda] > 0$ and $\text{Im}[\lambda] < 0$.

Similarly for all points in the complex λ -plane such that $\text{Re}[\lambda] > k$ and $\text{Im}[\lambda] < 0$, θ_1 lies in the range $-90^\circ < \theta_1 < -180^\circ$, while θ_2 is always less than zero. Therefore it can be shown that for this set of points, conditions (47) are satisfied.

Thus, the choice of the branch cuts, as shown in Fig. 3, satisfy conditions (47). The path of integration is shown in Fig. 4.

Now these integrals can be solved by two methods. The first one is the conventional complex plane integration method, while the other is the numerical integration method. In the complex plane integration method, by analytical continuation, the path of integration is extended from 0 to ∞ , to $-\infty$ to ∞ , and then this path is deformed to the steepest descent path, passing through the saddle point. This only gives good results for the intermediate and the far zone. In the evaluation of the current distribution by method of moments, field computations very close to the

source are required, in which case the solution diverges. On the other hand, numerical evaluation of these integrals is valid for all distances and can yield accurate results [19].

The numerical integration of the integrals given by (44) and (45) has been performed by real axis integration over the $0-\infty$ interval. The convergence of these integrals can be enhanced due to the presence of the factor $\exp(-\mu(z-B))$ in the integrands. For antennas printed on the substrate $z=B$, this factor tends to unity. Integrals (44) and (45) become slowly convergent, but still remain proper. Simpson's rule has been used to carry out numerical integration. Numerical integration is stopped when $\lambda=A$, where A satisfies the relation $\coth(B.A) \approx 1.0$. The tail contribution is evaluated analytically.

The integration interval $(0,\infty)$ is divided into the following subintervals:

- 1) $0 < \lambda < k$: Integration over this interval is performed numerically. The integrals contribute to the radiation resistance and to the reactive part of the input impedance.
- 2) $k < \lambda < nk$: The integrands have poles in this interval. The poles correspond to the surface wave modes excited by the antenna. The number of modes excited depends upon the thickness B of the substrate, its dielectric constant ϵ_r and the frequency of operation. The modes are zeros of the factors,

$$D_e(\lambda) = \mu + \mu_e \coth \mu_e B ; \quad \text{TM modes}, \quad (49)$$

$$D_m(\lambda) = n^2 \mu + \mu_e \tanh \mu_e B ; \quad \text{TE modes}. \quad (50)$$

Using the singularity extraction technique, the integral can be written as,

$$\int_k^{nk} \frac{f(\lambda)}{(\lambda - \lambda_0)} d\lambda = \int_k^{nk} \frac{f(\lambda) - f(\lambda_0)}{(\lambda - \lambda_0)} d\lambda + \int_k^{nk} \frac{f(\lambda_0)}{(\lambda - \lambda_0)} d\lambda . \quad (51)$$

The first integral on the right hand side of (51) can be evaluated numerically, while the second integral can be integrated analytically, as illustrated in Appendix D. This technique can be extended depending upon the number of modes. The two surface wave modes are treated in Appendix E as an example.

3) $nk < \lambda < A$: Numerical integration is again invoked here. The choice of the number A depends mainly on the thickness of the substrate B and its dielectric constant ϵ_r . The factor A is such that it satisfies,

$$\coth(\sqrt{\lambda^2 - n^2 k^2} \cdot B) \approx 1.0 \quad \text{for all } \lambda > A. \quad (52)$$

4) $A < \lambda < \infty$: The special nature of the integrand is invoked in this interval. The use of (52) simplifies the integrand to a form which involves radicals μ , μ_e . Since $\lambda > k$ and nk , after application of the binomial series expansion to these radicals, the tail part of the integrals can be written as (see Appendix F),

$$2 \int_A^\infty \frac{J_0(\rho\lambda)}{\mu + \mu_e} d\lambda = \int_A^\infty d\lambda \cdot J_0(\rho\lambda) \left[1 + \frac{XL}{\lambda^2} + \frac{XT}{\lambda^4} + \frac{XC}{\lambda^6} + \dots \right] \quad (53)$$

Thus the integrand has been reduced to a highly convergent series. The series is analytic, hence term by term integration can be performed analytically. The constants XL, XT, XC, \dots involve the wave number k and the dielectric constant ϵ_r . They are defined in Appendix F.

2.4 INPUT IMPEDANCE:

In Section 2.2, the problem for the current distribution of the printed dipole has been formulated. The solution described uses sinusoidal subsection currents and Galerkin's method [20], which is also equivalent to the reaction concept [16]. The dipole is excited by an idealized source, the delta gap generator. In actual practice, the excitation is different from the assumed model. In air, it has been found that the input impedance is not critically dependent upon the excitation gap length lg as long as the gap length lg is $< 0.1\lambda_0$. Therefore, neglecting the effect of the incoming exciting line, the input impedance for a small gap between the input terminals will be as seen by the delta gap generator.

In the computations of current distribution, the circumferential variation of the antenna current has been neglected. This is due to the fact that whatever device is used to measure the input impedance, it is insensitive to the circumferential variation of the current, provided the

wire is very thin. Thus the thin wire approximation is in fact, valid [12].

The input impedance of the printed wire dipole for a 1.0 volt input excitation, is given by,

$$Z_{in} = 1.0/I_{in} \quad (54)$$

where I_{in} is the current at the input terminals of the antenna, obtained from the knowledge of the current distribution.

2.5 RADIATION PATTERN OF A PRINTED DIPOLE:

Radiation pattern or far zone fields can be obtained by using a rigorous numerical technique as described in Section 2.3. The numerical technique, although valid for all distances, is quite expensive for the far zone computations. In the calculation of the radiation pattern, the far zone fields above the air dielectric interface are only required. Hence the conventional stationary phase method [21] can be used. The details of the method are covered in Appendix G. The far zone fields component not very close to the interface, i.e., $\theta < 90^\circ$, are given as follows,

$$E_\theta(\theta, \phi) = 2.k^2\Pi_\theta, \quad (55)$$

$$E_\phi(\theta, \phi) = 2.k^2\Pi_\phi \quad (56)$$

$$\Pi_\theta = u_e \frac{e^{jkr}}{r} \cdot \frac{e^{-jkB\cos\theta}}{D_e(\theta, \phi)} \cdot \cos\theta + \frac{n^2-1}{n^2} \cdot \frac{\tan\theta \cdot \sin\theta}{D_m(\theta, \phi)} \cos\phi \cdot I_x \quad (57)$$

and

$$\Pi_{\phi} = -u \cdot \frac{e^{jkr}}{r} \cdot \frac{e^{-jkB\cos\phi}}{D_e(\theta, \phi)} \cdot \sin\phi \cdot I_x \quad (58)$$

where I_x is given by,

$$I_x = \int_S J_s(x', y') \cdot e^{-jk(x'\sin\theta\cos\phi + y'\sin\theta\sin\phi)} dx' dy'. \quad (59)$$

For a printed wire dipole, as shown in Fig. 2, the current distribution can be written as,

$$J_s(x', y') = I(x') \cdot \delta(y') \quad (60)$$

where $I(x')$ is in tabulated form. After substituting (60) in (59) and by integrating with respect to y' (59) reduces to,

$$I_x = \int_L I(x') \cdot e^{-jkx' \cdot \sin\theta \cdot \cos\phi} dx'. \quad (61)$$

The integration with respect to x' is performed numerically and by making use of (55) and (58), the radiation pattern is obtained.

2.6 NUMERICAL RESULTS:

In this section, numerical results are presented for the printed dipole. Numerical computations have been performed for a very thin wire dipole, a typical radius $a = 0.0001\lambda_0$ has been chosen. The dipoles are center fed by an in phase unit voltage delta gap generator. All dimensions presented, are normalized with respect to free space wavelength λ_0 . Due to assumed time dependency, i.e., $e^{j\omega t}$, inductive reactance is taken as negative in all plots.

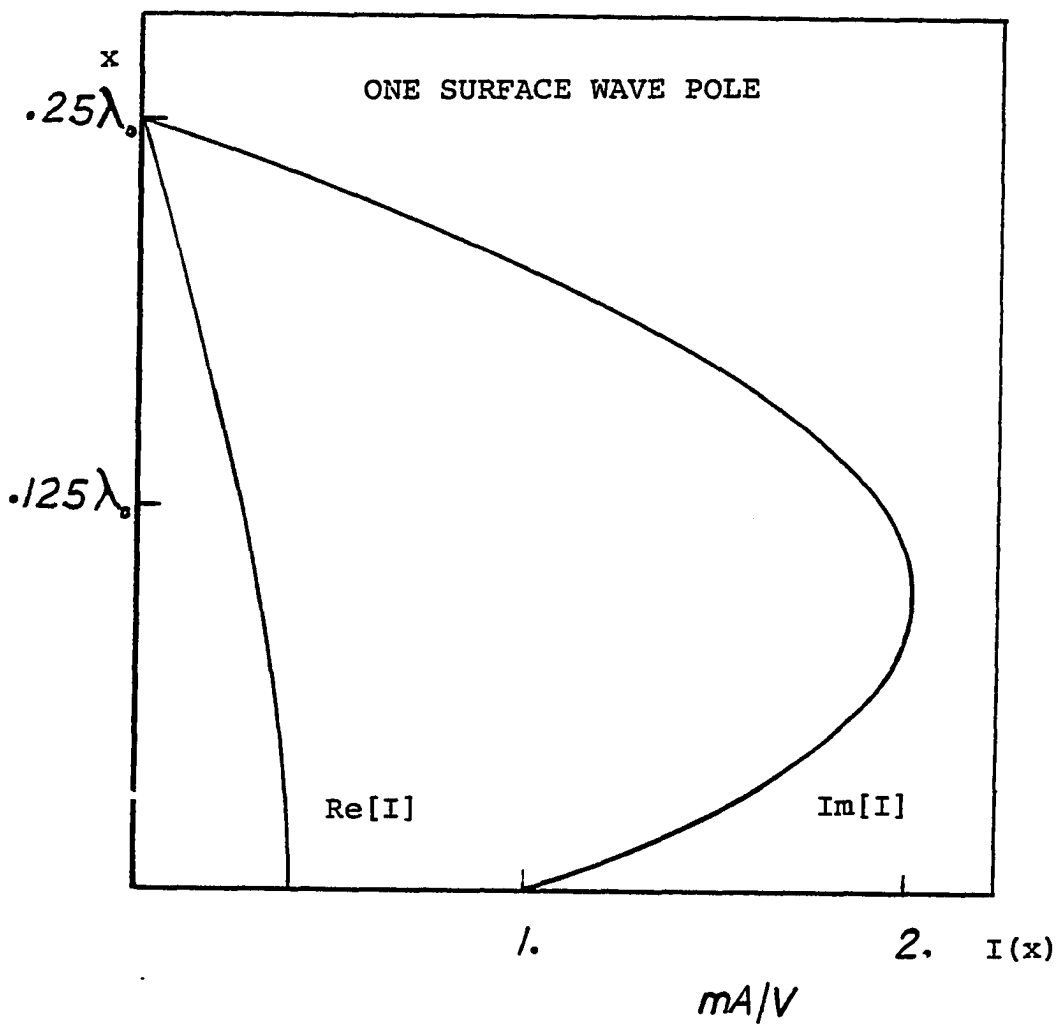


Fig. 5. Current Distribution on a Printed Wire Dipole
 $\text{Re}[I]$ and $\text{Im}[I]$ vs x (in λ_0), ($B=0.1016\lambda_0$, $\epsilon_r=3.25$)

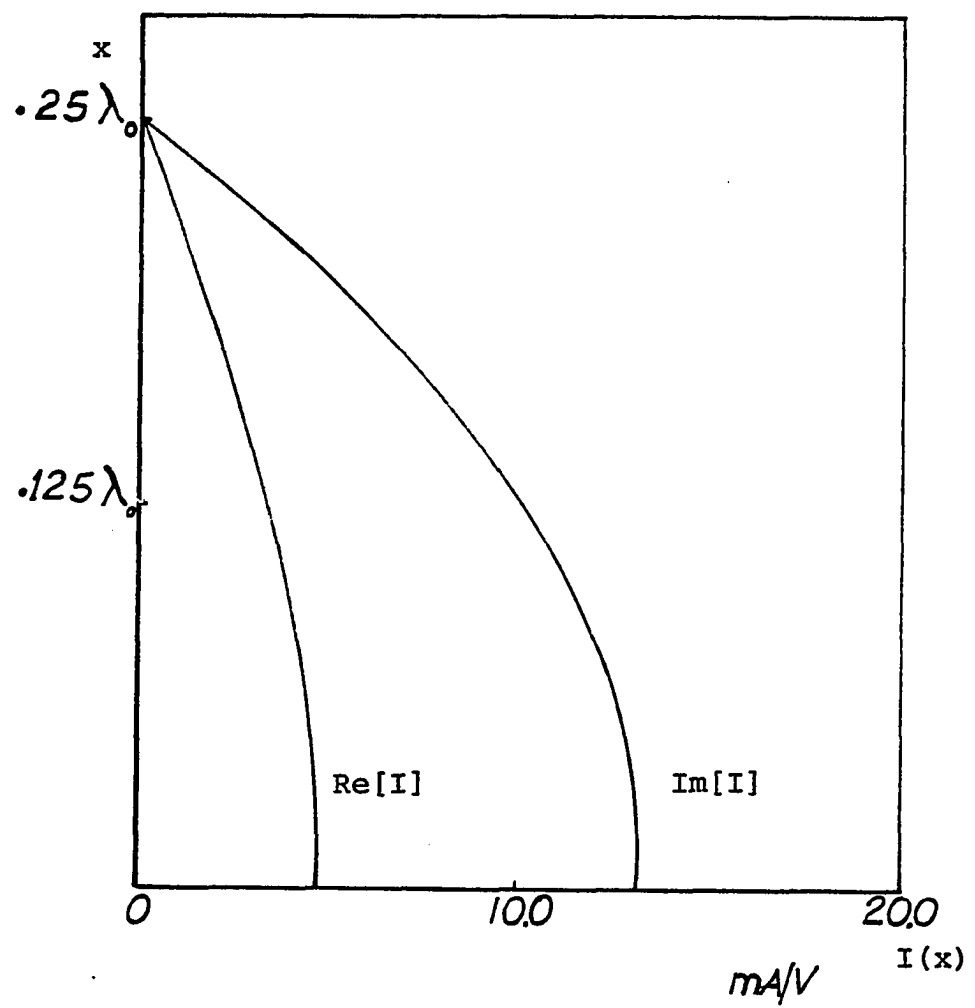


Fig. 6. Current Distribution on a Printed Wire Dipole
 $\text{Re}[I]$ and $\text{Im}[I]$ vs x (in λ_0), ($B=0.1016\lambda_0$, $\epsilon_r=1.0$)

The current distribution over a dipole of length $0.5\lambda_0$, printed on a dielectric substrate of thickness $B = 0.1016\lambda_0$ and dielectric constant $\epsilon_r = 3.25$ is shown in Fig. 5. The $\text{Re}[I]$ and $\text{Im}[I]$ are plotted separately. Due to the presence of the substrate, the electric length of the dipole increases and hence there is a dip in the current distribution curve at the feeding point. For comparison, the current distribution for $\epsilon_r = 1.0$ (while the other parameters remain the same), is shown in Fig. 6. Physically this means that the substrate has been removed. Due to the proximity of the ground plane, $\text{Im}[I]$ is greater than $\text{Re}[I]$. This shows that the dipole radiates less power as compared to a dipole in free space. Comparing Figs. 5 and 6, it is obvious that the current level on the printed dipole is about ten times less than the dipole over a grounded plane.

To see the effect of the substrate thickness B , a computation has been carried out for increased substrate thickness, i.e., $B = 0.127\lambda_0$. The current distribution for this case is shown in Fig. 7. In comparing Fig. 7 with Fig. 5 it can be seen that the substrate thickness does not effect the shape of the distribution very much but that current levels are changed. This means that the input impedance of the dipole is effected. It should be noted that in the above discussion, only one surface wave mode has been allowed.

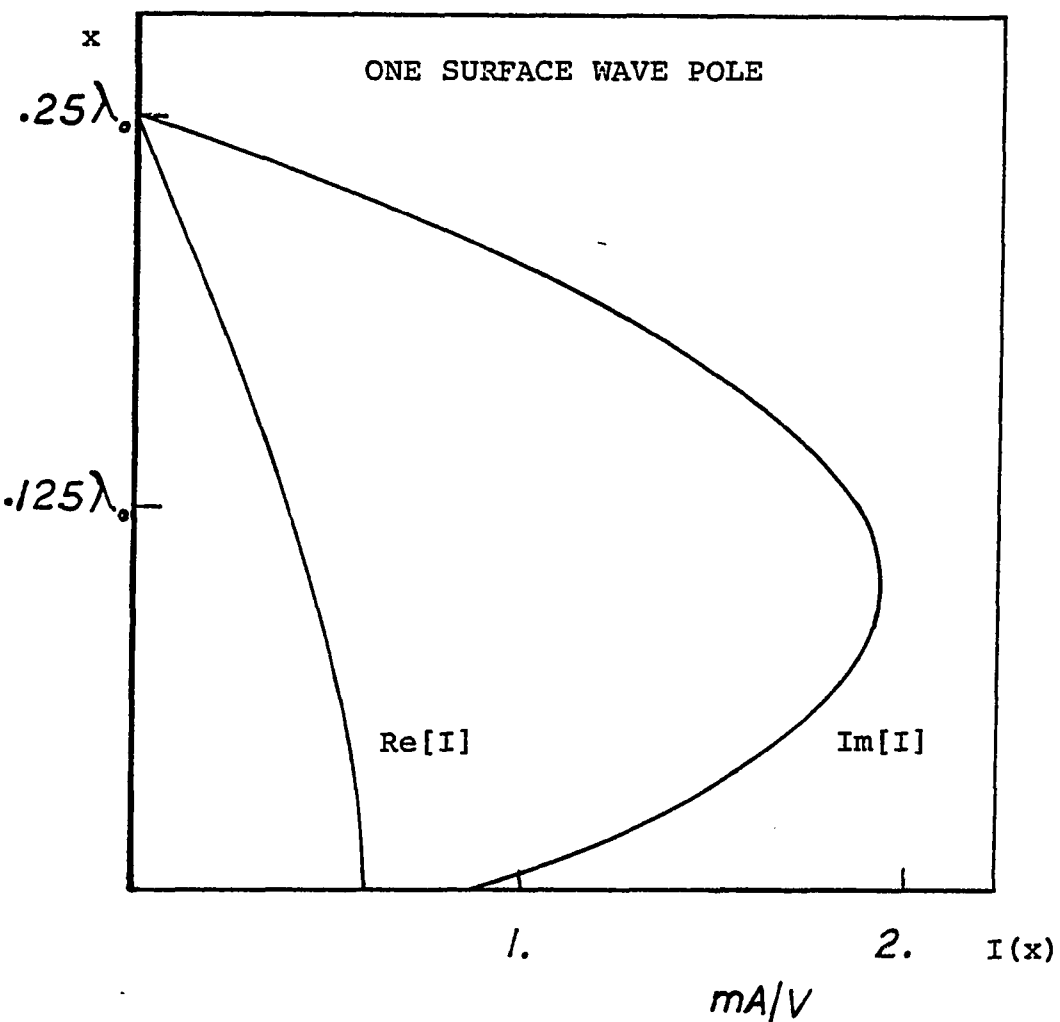


Fig. 7. Current Distribution on a Printed Wire Dipole
 $\text{Re}[I]$ and $\text{Im}[I]$ vs x (in λ_0), ($B=0.127 \lambda_0$ $\epsilon_r=3.25$)

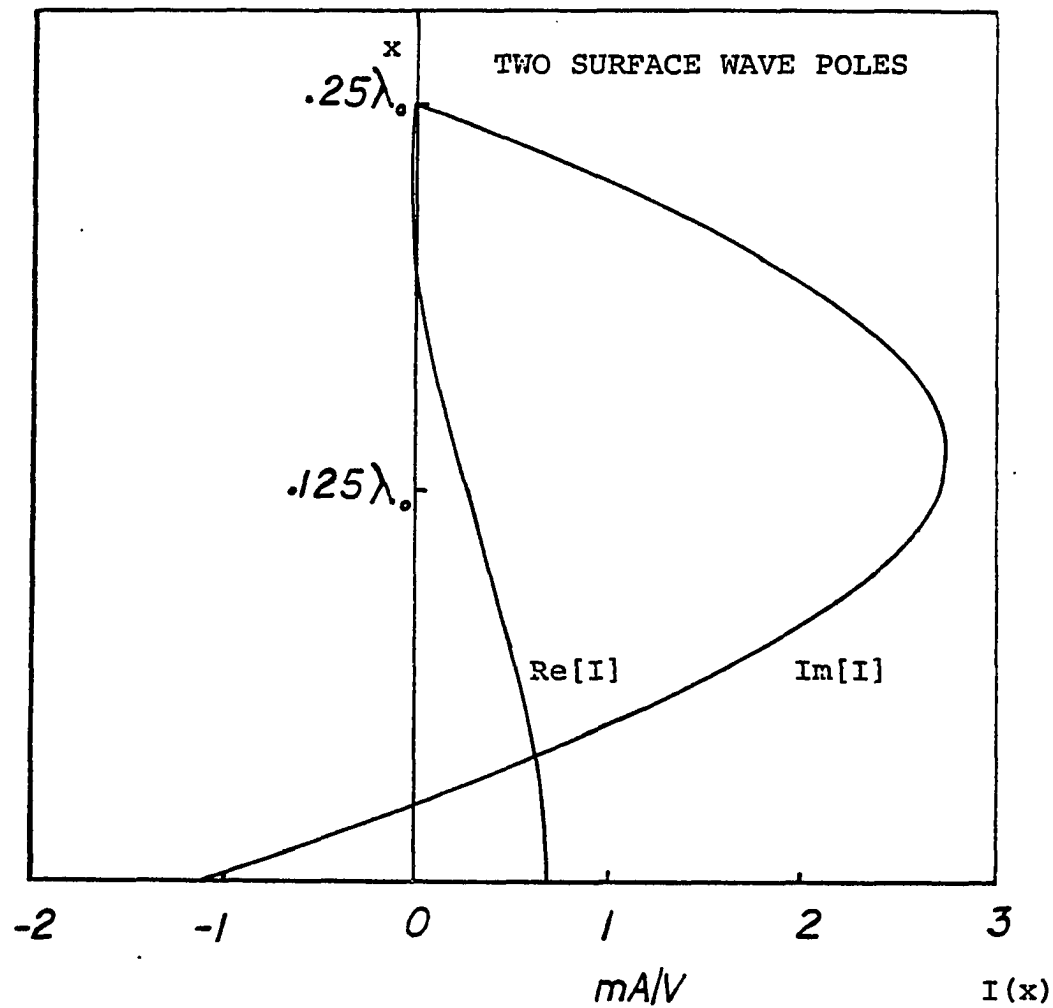


Fig. 8. Current Distribution on a Printed Wire Dipole
 $\text{Re}[I]$ and $\text{Im}[I]$ vs x (in λ_0), ($B=0.15\lambda_0$, $\epsilon_r=8.5$)

The substrate thickness B and dielectric constant has been increased to $0.15\lambda_0$, and 8.5, respectively, in order to allow two propagating surface wave modes. The current distribution is shown in Fig. 8. The following effects are in order:

- 1) The $\text{Re}[I]$ and $\text{Im}[I]$ both change sign.
- 2) The electric length of the dipole increases drastically.

It can be inferred from the above discussion that the impedance level of the printed dipole is higher than the dipole over the grounded plane. This higher impedance level is attributed to the fact that the printed dipole radiates power as space waves and launches a surface wave in the dielectric surface guide. However, this surface wave contributes only to the real part of the input impedance. The higher order nonpropagating modes contribute to the reactive part of the input impedance.

Figs. 9 through 11 show the input impedance of the printed dipole versus its length L , for different substrate thickness and dielectric constants. Comparison of the resonant length L_r and the input impedance Z_{in} for all the above mentioned cases is given in Table I.

The real part of the Z_{in} is the sum of two terms, namely, the radiation resistance and the surface wave launching resistance. By increasing the substrate thickness from $0.1016\lambda_0$ to $0.127\lambda_0$, the resonant impedance increases from 34.5Ω to 60.0Ω . This is because of the following

TABLE I

Printed dipole parameters for different values of B and ϵ_r

# of modes	ϵ_r	B	L_r	Z_{in} (resonant)	Z_{in} (for $L=0.5\lambda_0$)
1	3.25	$0.1016\lambda_0$	$0.317\lambda_0$	$34.5 + j0 \Omega$	$330 - j880 \Omega$
1	3.25	$0.127\lambda_0$	$0.315\lambda_0$	$60.0 + j0 \Omega$	$535 - j788 \Omega$
2	8.50	$0.150\lambda_0$	$0.230\lambda_0$	$50.0 + j0 \Omega$	$418 + j664 \Omega$

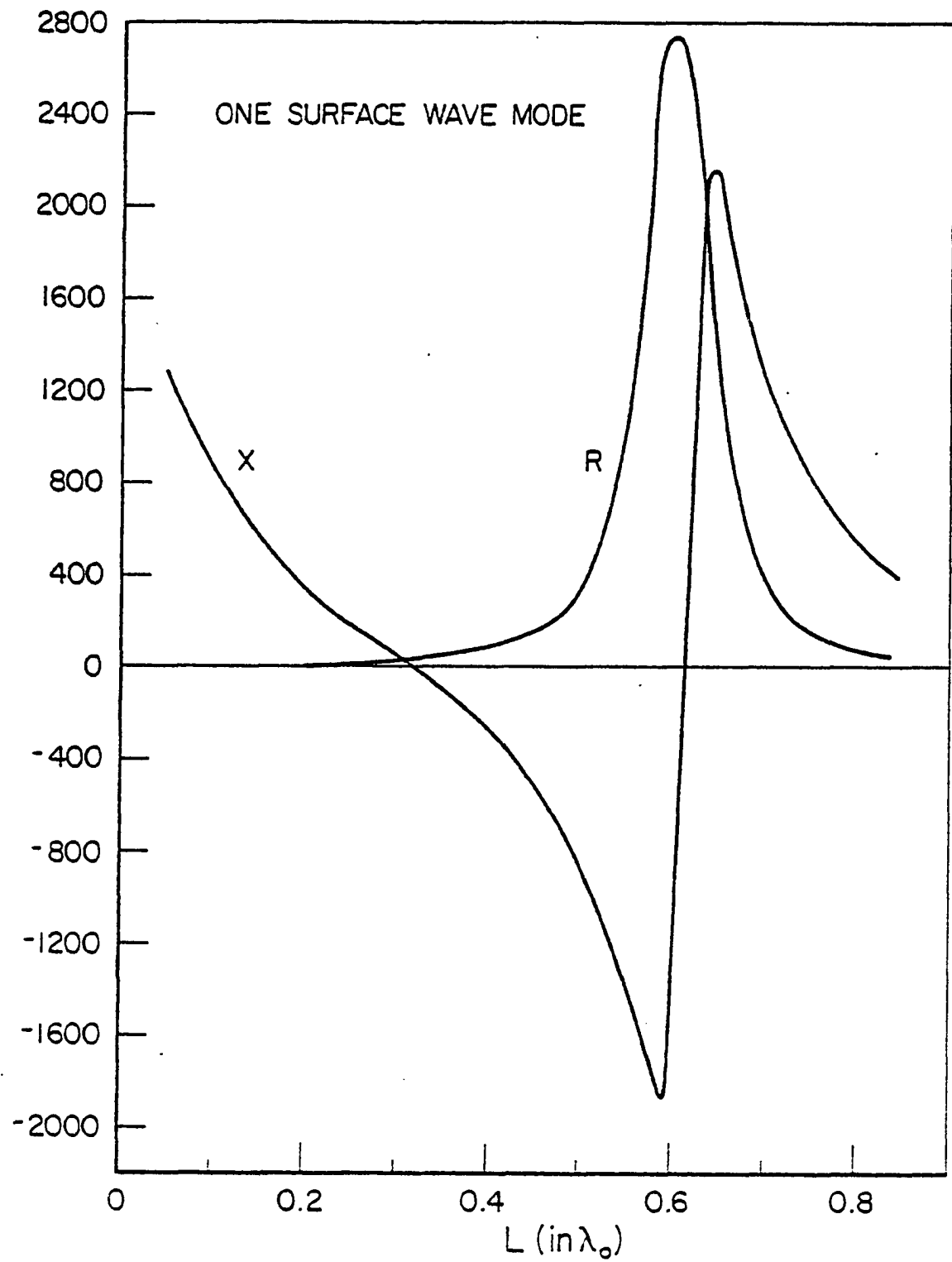


Fig. 9. Input Impedance of a Printed Wire Dipole vs
 L (in λ_0), ($B=0.1016\lambda_0$, $\epsilon_r=3.25$, $a=0.00005\lambda_0$)

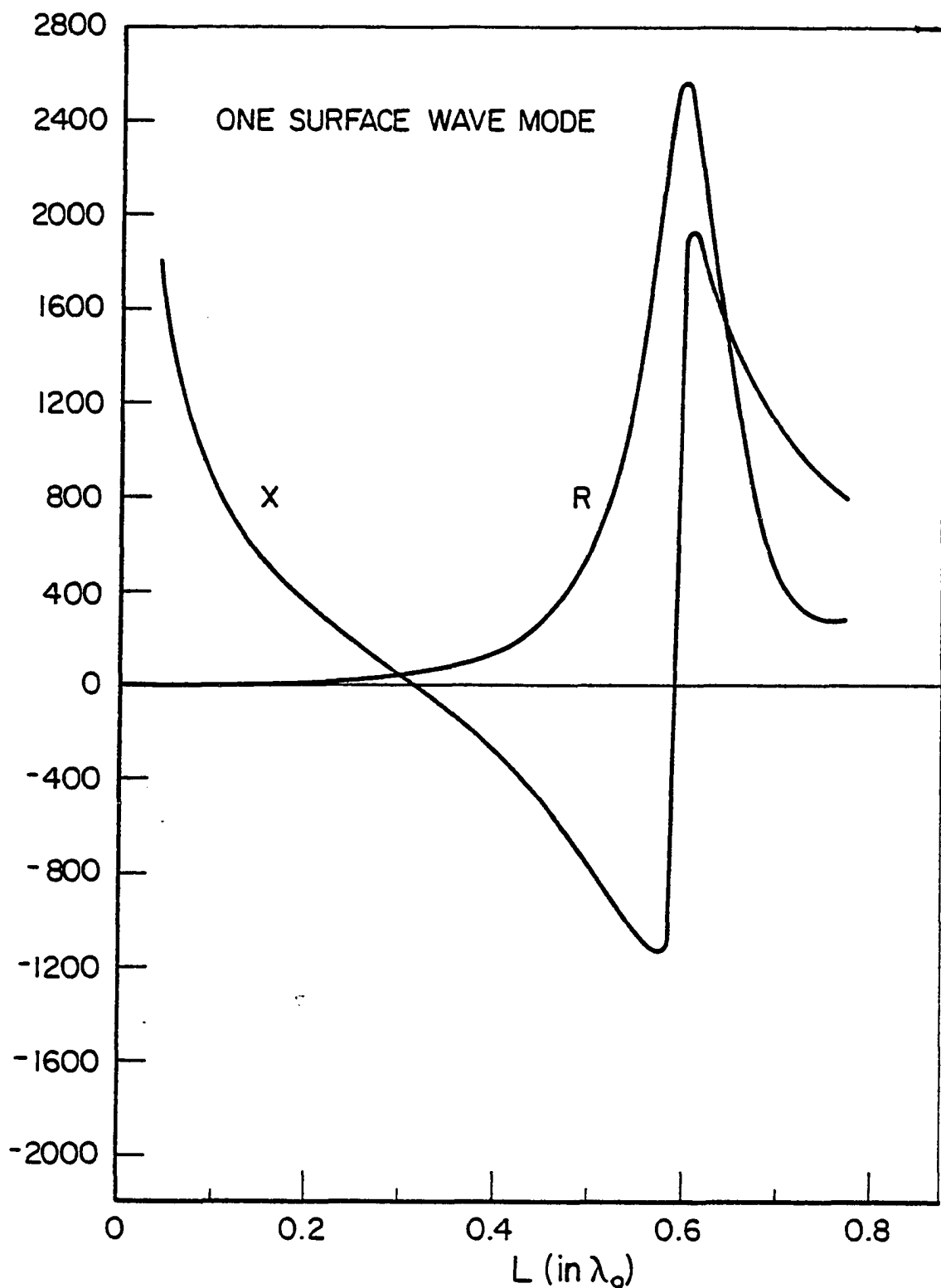


Fig. 10. Input Impedance of a Printed Wire Dipole vs
 L (in λ_0), ($B=0.127\lambda_0$, $\epsilon_r=3.25$, $a=0.00005\lambda_0$)

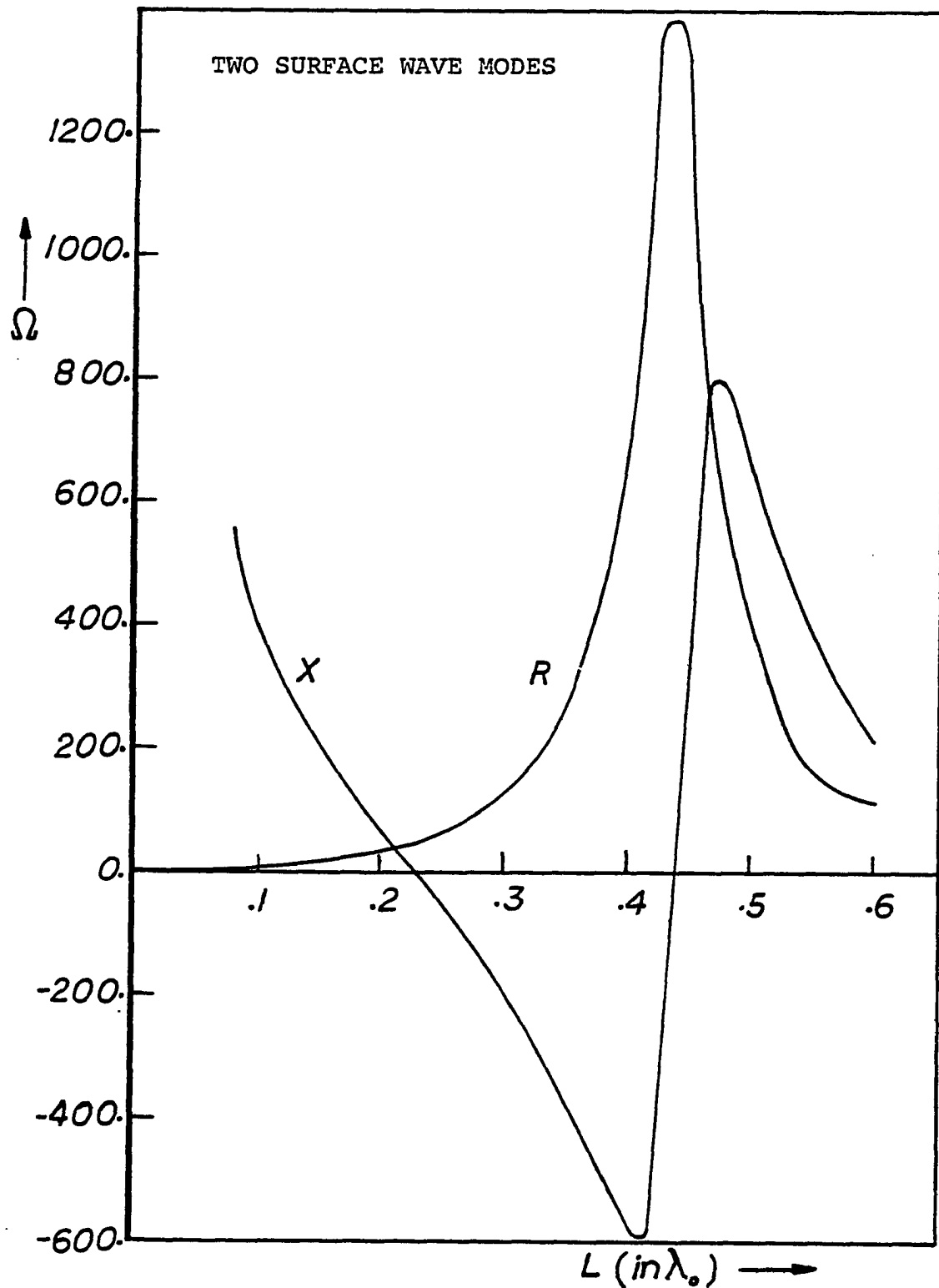


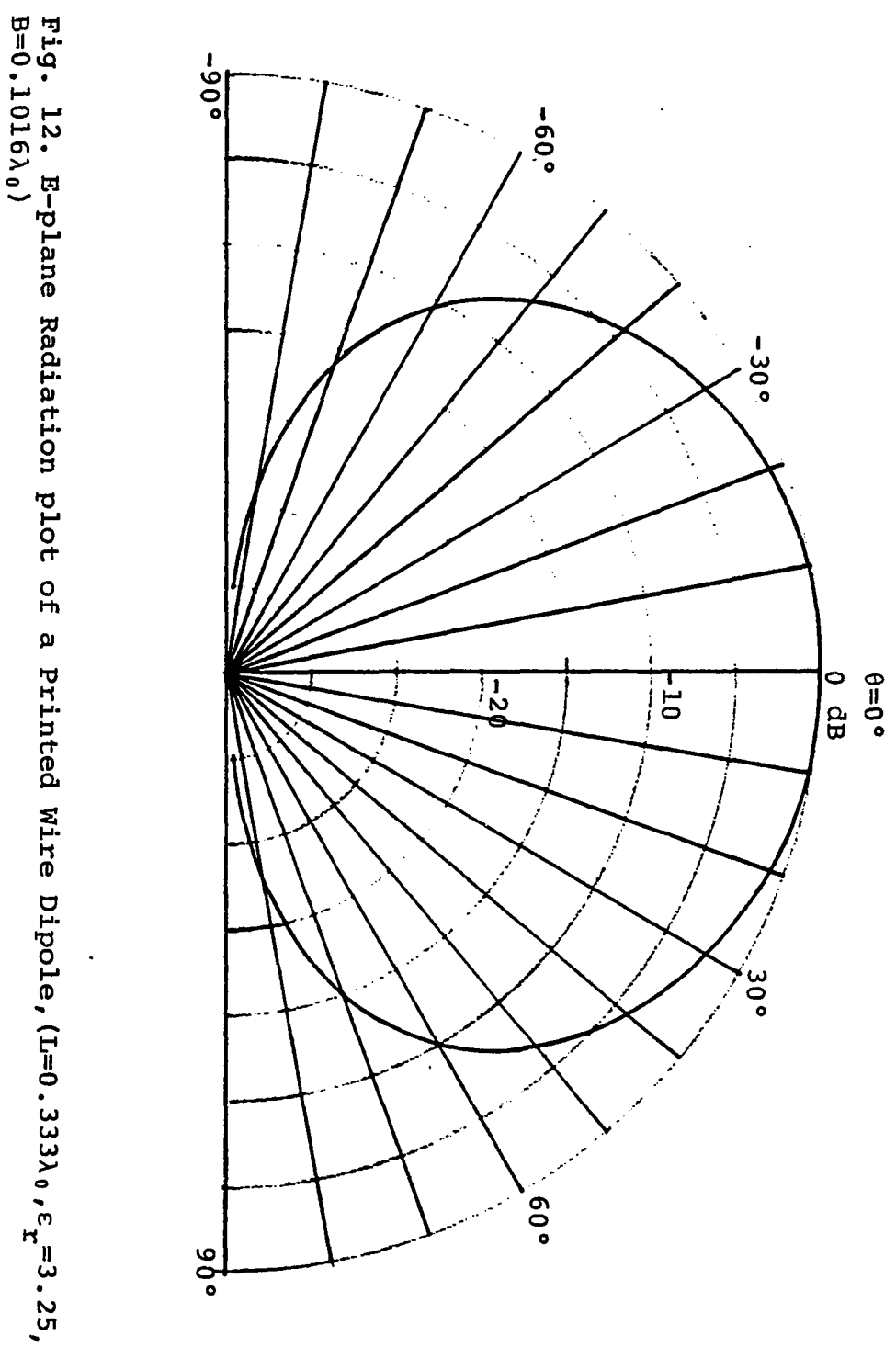
Fig. 11. Input Impedance of a Printed Wire Dipole vs
 L (in λ_0), ($B=0.15\lambda_0$, $\epsilon_r=8.5$, $a=0.000025\lambda_0$)

reason:

- 1) The increased substrate thickness increases the surface wave launching efficiency.
- 2) A little reduction in the proximity from the ground plane, increases the radiation efficiency.

The two propagating surface wave modes also effect the impedance characteristics of the printed dipole. The increased dielectric constant ($\epsilon_r = 8.5$) reduces the radiation resistance (efficiency) of the printed dipole. This is due to the fact that the electric flux lines have greater affinity for the dielectric medium than for free space. Therefore, a major portion of the input power to the dipole is guided as two surface waves modes, rather than being radiated. The printed dipole in this case is not a good radiator.

Lastly, E-plane and H-plane radiation patterns of the printed dipole are shown in Fig.12 and 13. Near the air dielectric interface, i.e., $\theta = \pm 90^\circ$, the radiation plots are not exact since the stationary phase method used in the development of the formula for the radiated fields, is not valid when $\theta = \pm 90^\circ$. However, numerical integration technique can yield exact computation in this region.



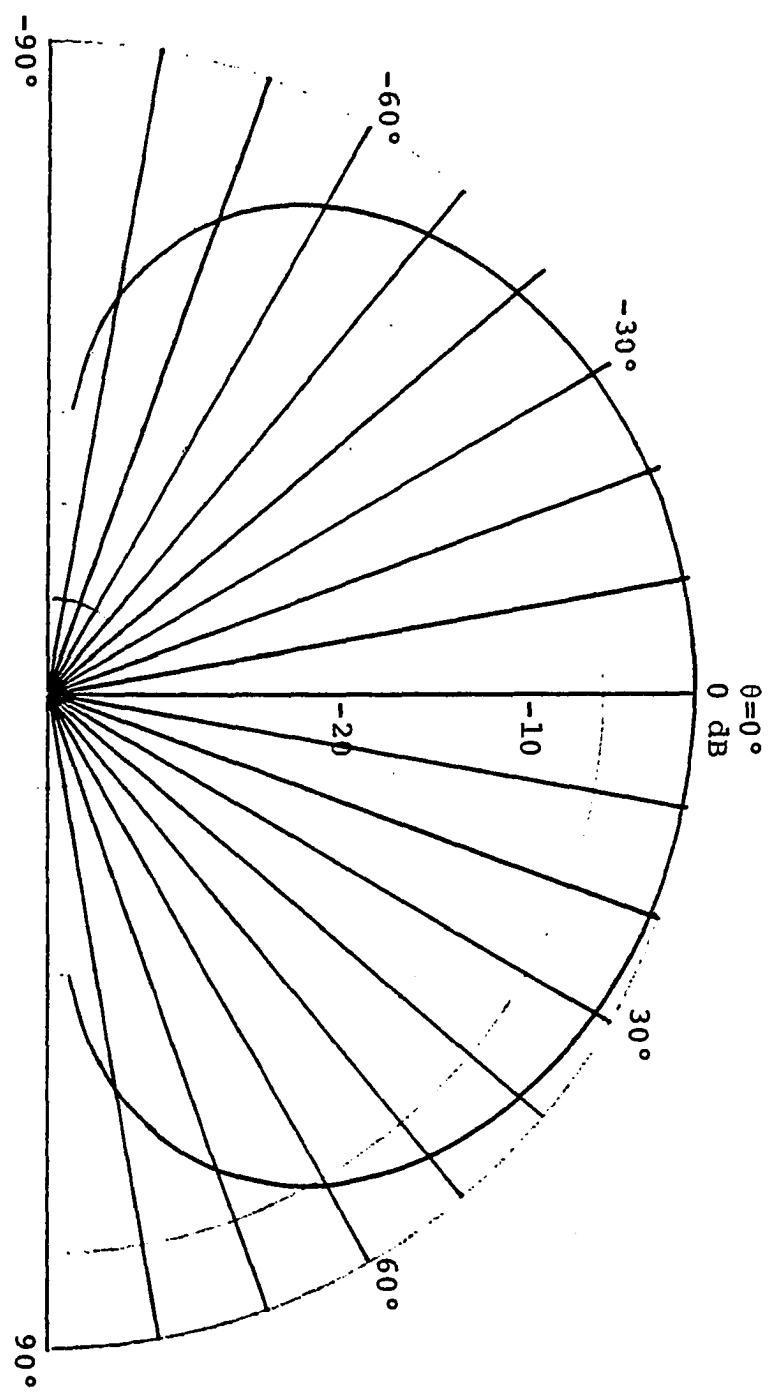


Fig. 13. H-plane Radiation plot of a Printed Wire Dipole, ($L=0.333\lambda_0$, $B=0.1016\lambda_0$, $\epsilon_r=3.25$)

Chapter III

PRINTED ARRAY PARAMETERS

Printed arrays (on a grounded dielectric substrate) have different behavior from arrays in free space. This is due to the fact that each element of the printed array launches a surface wave in addition to the space wave radiation. The surface wave propagates along the grounded substrate which acts as a guiding structure and couples energy with other elements of the array. The surface wave launching efficiency may have spatial dependence. Hence it is required to look at mutual coupling between two printed dipoles in different configurations.

In the computation of the mutual coupling, it is important to know about the exact current distribution over the pair. In Section 3.1, the formulation of the integral equation for the unknown currents $I_1(x')$ and $I_2(x')$ is presented. The current distribution computation is followed by the mutual impedance calculations. Results for the dipoles in broadside, echelon and collinear arrangements are presented. A discussion is undertaken about the surface wave launching. It is indicated that in the collinear configuration mutual coupling is mainly due to the surface waves.

3.1 CURRENT DISTRIBUTION OVER TWO PARALLEL PRINTED DIPOLES:

In Fig. 14, two printed dipoles are shown at a

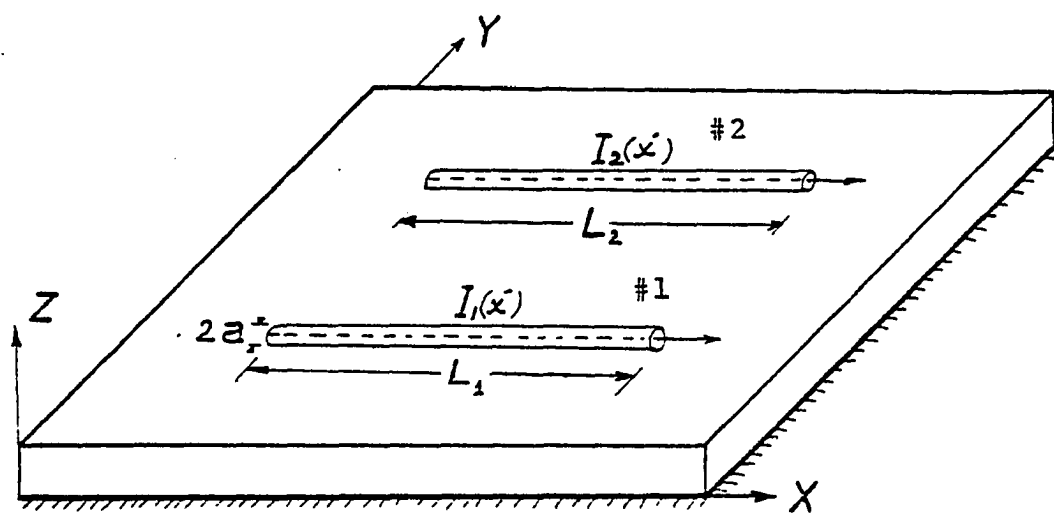


Fig. 14. A Printed Wire Dipole Pair (Driven and Parasitic)

distance S apart. The dipoles are assumed to have lengths and radii (L_1, a) and (L_2, a) , respectively. The radius a of the dipoles is assumed very small compared to the free space wavelength λ_0 (see Section 2.2). Dipole #1 is excited while dipole #2 is short circuited, and is acting as a parasitic. The current distribution over the pair can be expressed as,

$$J(x', y') = [I_1(x') \delta(y') P_1 + I_2(x') \delta(y' - S) P_2] \delta(z' - B) \hat{x} \quad (62)$$

where $I_1(x')$ and $I_2(x')$ are unknown currents, over dipole #1 and #2, respectively. P_1 and P_2 are two unit pulse functions which are zero everywhere except over the lengths of the dipoles L_1 and L_2 . Substituting (62) in (32), the axial component of the electric field E_x at any point over the substrate is given by,

$$E_x = \int_{L_1, y'=0} I_1(x') \left[k^2 \Pi_x + \frac{\partial^2 \Pi}{\partial x^2} + \frac{\partial^2 \Pi}{\partial x \partial z} \right] dx' + \int_{L_2, y'=S} I_2(x') \left[k^2 \Pi_x + \frac{\partial^2 \Pi}{\partial x^2} + \frac{\partial^2 \Pi}{\partial x \partial z} \right] dx' \quad . \quad (63)$$

Repeating the steps illustrated in Section 2.2, i.e., dividing the two dipoles in subsections N_1 and N_2 , and making use of the sinusoidal expansion functions and Galerkin's method, the following matrix equation is obtained,

$$\begin{bmatrix} V_1 \\ V_2 \\ \cdot \\ \cdot \\ V_M \end{bmatrix} = \begin{bmatrix} Z_{11}, Z_{12}, \dots \\ Z_{21}, Z_{22}, \dots \\ \cdot \\ \cdot \\ Z_{M1} \end{bmatrix} \begin{bmatrix} I_1 \\ I_2 \\ \cdot \\ \cdot \\ I_M \end{bmatrix} \quad (64)$$

where $M = N_1 + N_2 - 2$.

Depending upon the location of the generator, the corresponding excitation voltage is set to 1. The inversion of the matrix then gives the current distribution on the dipole parasitic pair. This method can further be extended to any number of printed dipoles parasitic or active. However, the computer storage available, does limit the number of elements which can be handled.

3.2 MUTUAL IMPEDANCE COMPUTATIONS:

In Section 3.1, a method is illustrated to compute the current distribution over a pair of printed dipoles, which are driven and parasitic. The knowledge of the current distribution over the pair will be used in this section to determine the mutual impedance between the printed dipoles. The input impedance of the two dipole printed array is given by,

$$Z_{in} = Z_{11} + Z_{12} \cdot I_2 / I_1 \quad (65)$$

where Z_{11} is the self impedance of the driven dipole when

the parasitic dipole is open circuited. Also, Z_{11} is the mutual impedance between the pair, whereas I_1 and I_2 are the input currents which flow into the input terminal of the driven dipole and across the short circuited input terminals of the parasitic dipole. For unit voltage excitation, i.e., $V = 1.0$ volts, the input impedance of the array is given by,

$$Z_{in} = 1.0/I_1 . \quad (66)$$

The self impedance Z_{11} of the driven dipole is obtained numerically by deleting the $(N_1+N_2/2-1)$ th row and column of the matrix equation (64) and inverting the resultant (N_1+N_2-3) th order matrix. Physically, this operation means open circuiting the parasitic dipole. The input current of the driven dipole I'_1 gives the self impedance Z_{11} as,

$$Z_{11} = 1.0/I'_1 . \quad (67)$$

When (66) and (67) are inserted in (65), the mutual impedance between the two printed dipoles is given by,

$$Z_{12} = 1.0/I_2 - I_1/(I'_1 \cdot I_2) . \quad (68)$$

3.3 FIELDS EXCITED BY A PRINTED DIPOLE ALONG AIR DIELECTRIC INTERFACE:

Mutual coupling between two printed dipoles is dominantly determined by the fields which exist along the air dielectric interface. The fields excited by a printed dipole along the air dielectric interface can be decomposed

into the following components [22]:

- 1) Direct wave $\sim 1/\rho$.
- 2) Higher order wave $\sim 1/\rho^2$.
- 3) Surface waves $\sim 1/\sqrt{\rho}$.
- 4) Leaky wave $\sim \exp(-\lambda\rho)/\sqrt{\rho}$, $\lambda > 0$.

This decomposition can be explained in the context of saddle point integration method. The saddle point and its vicinity contribute to the direct wave, while for small ρ , the integration over the rest of the SDP is significant, and results in higher order waves. The surface and leaky waves are contributed by the poles which the integration contour crosses during its deformation to the SDP.

As ρ increases, the surface waves constitute the dominant contribution because of their cylindrical wave character $1/\sqrt{\rho}$, as oppose to the spherical behavior of the direct wave.

The number of surface wave modes generated by the antenna depends upon the thickness and dielectric constant of the substrate. The lowest order mode is the TM mode with a component of electric field parallel to the direction of propagation. Assuming single propagating mode, the antenna will generate a longitudinal component of the electric field which will be strongest near the tips of the dipole, as shown in Fig. 15. A strong surface wave will therefore be launched along the axis of the printed antenna. In the broadside direction ($\phi = 90^\circ$), a component of the electric

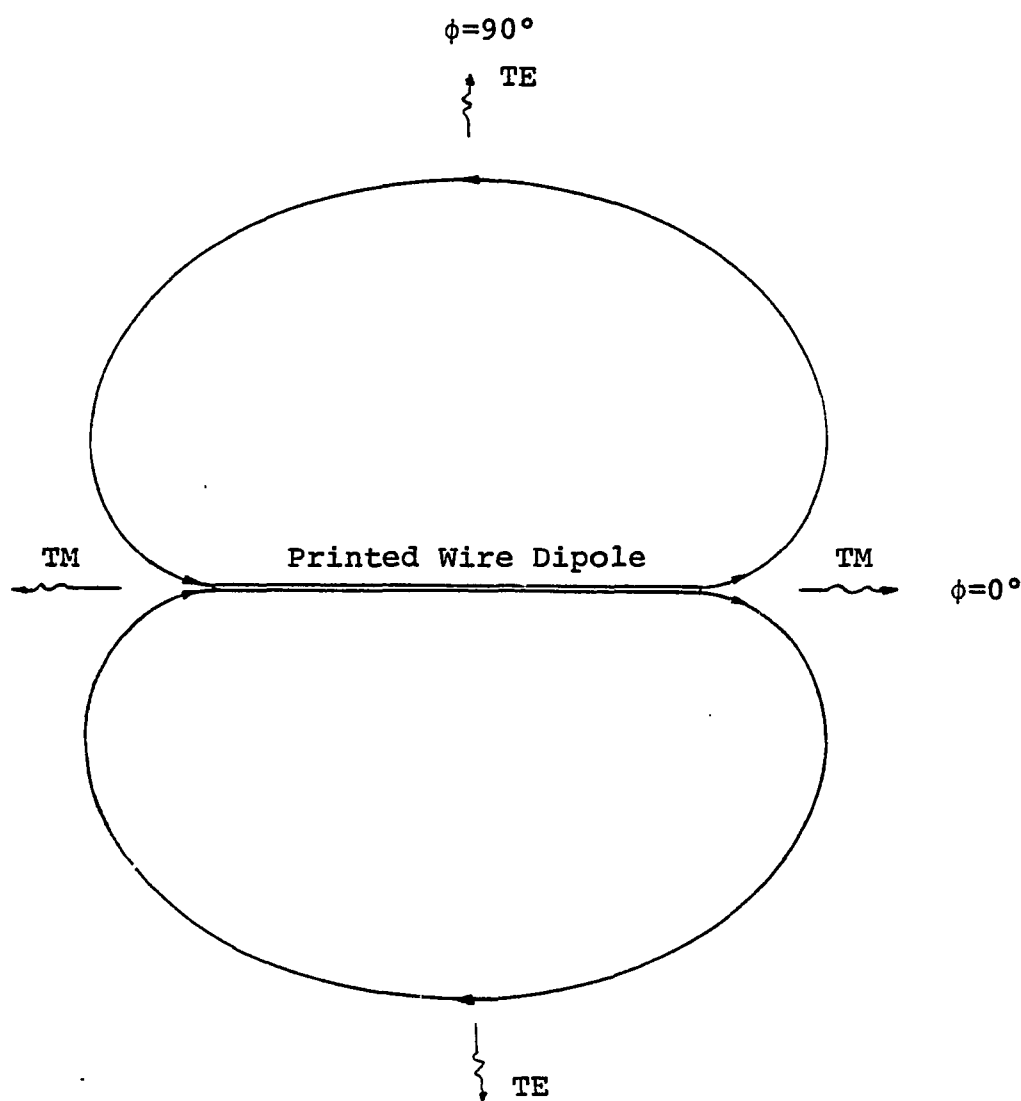


Fig. 15. Electric Flux Lines emanating from Printed Wire Dipole, (plan view)

field exists which is transverse to the direction of propagation. Therefore, the TM mode of the surface wave will not be excited. On the other hand, if the dielectric substrate guide allows two propagating surface wave modes, then in the broadside direction the TE mode of the surface waves is excited.

Mathematically, this spatial dependence can be viewed as follows. The lowest order TM mode is contributed by the factor $D_m(\lambda)$ which is present only in expression (27) for the component Π_z of the Hertz vector $\vec{\Pi}$. The expression for Π_z contains a factor $\cos\phi$ which determines the spatial variation of the surface wave.

From the above discussion, one concludes that for single propagating mode, the mutual coupling in broadside arrangement is mainly due to the direct, higher order and leaky waves, while in the collinear arrangement, dominant coupling is due to the TM mode of the surface waves. However, for two propagating modes, dominant coupling in the broadside configuration is due to the TE mode of the surface waves, while in the collinear configuration, it is due to the TM mode.

3.4 NUMERICAL RESULTS:

Mutual impedance computations between two printed dipoles have been performed in three configurations,

- 1) broadside 2) collinear 3) echelon.

As it is discussed in Section 3.3, the lowest order surface wave mode i.e., TM, has a launching pattern $\cos\phi$. This means that when two dipoles are in broadside configuration ($\phi=90^\circ$), the part of the total coupling due to the surface wave will be minimum. The coupling in this configuration will be mainly due to direct, higher order and leaky waves excited by the antenna.

Figs. 16 through 18 show broadside coupling between the two printed dipoles as a function of separation S for different antenna lengths. The rapid fall in mutual coupling for small separation ($S < 0.4\lambda_0$) confirms that the coupling is mainly due to higher order modes, while for ($S > 0.8\lambda_0$) direct wave takes over. In the intermediate zone ($0.4\lambda_0 < S < 0.8\lambda_0$), leaky wave modes are dominant.

The printed dipole launches a surface wave with maximum efficiency along the axial direction ($\phi = 0^\circ$). Also, the radiation pattern of a dipole in free space has nulls along the axial directions ($\phi=0^\circ$ and $\phi=180^\circ$). Therefore, based on these arguments, it can be concluded that in the collinear arrangement, the mutual coupling will be mainly due to the surface wave. The surface wave decay as $1/\sqrt{\rho}$. Hence, mutual coupling should decay slowly, in this configuration.

Figs. 19-21 show mutual impedance for the collinear case plotted versus separation G, for different dipole lengths. The mutual coupling decay very slowly with G. The

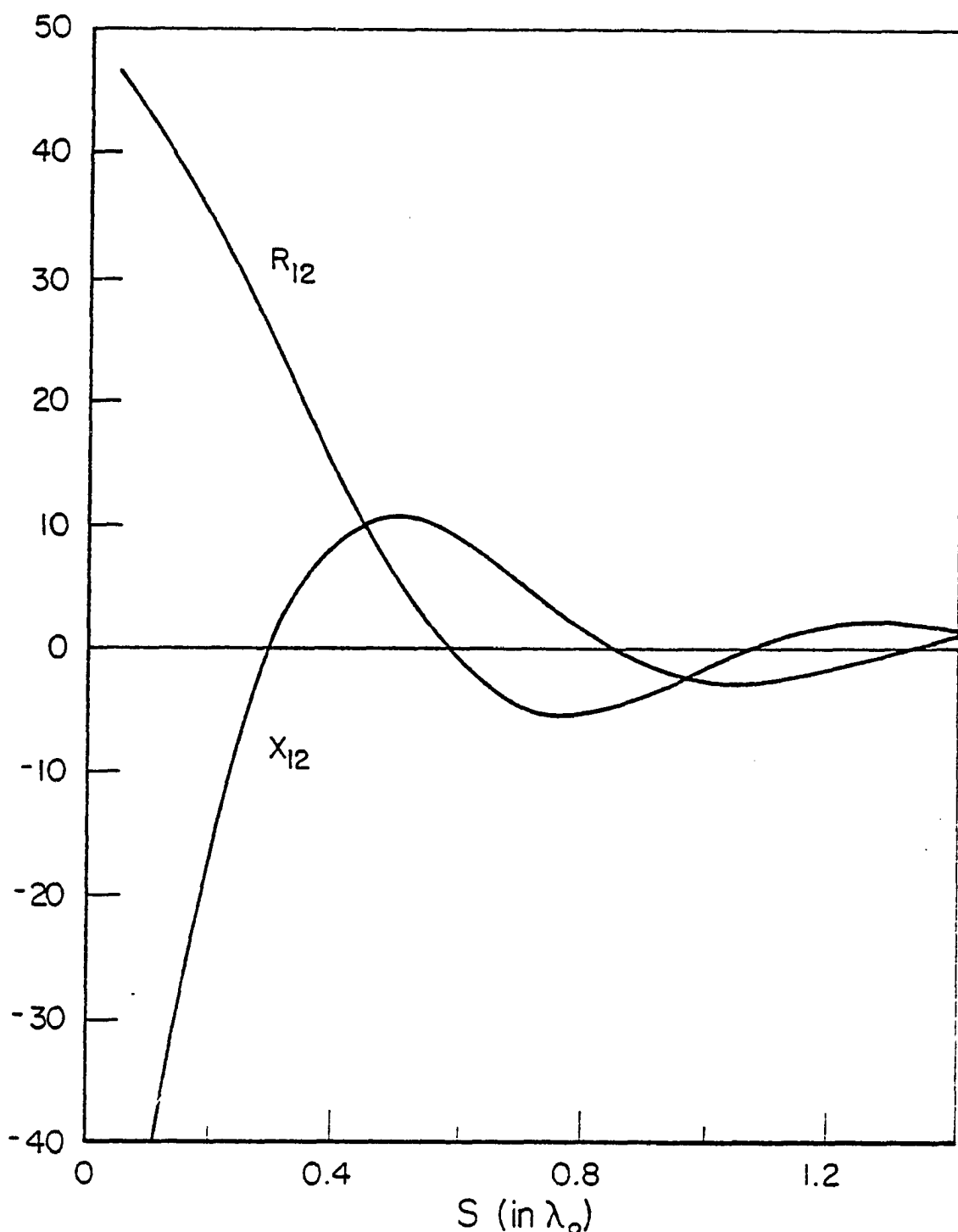


Fig. 16. Mutual Impedance between two Broadside Dipoles vs S (in λ_0), ($B=0.1016\lambda_0$, $\epsilon_r=3.25$, $L=0.333\lambda_0$)

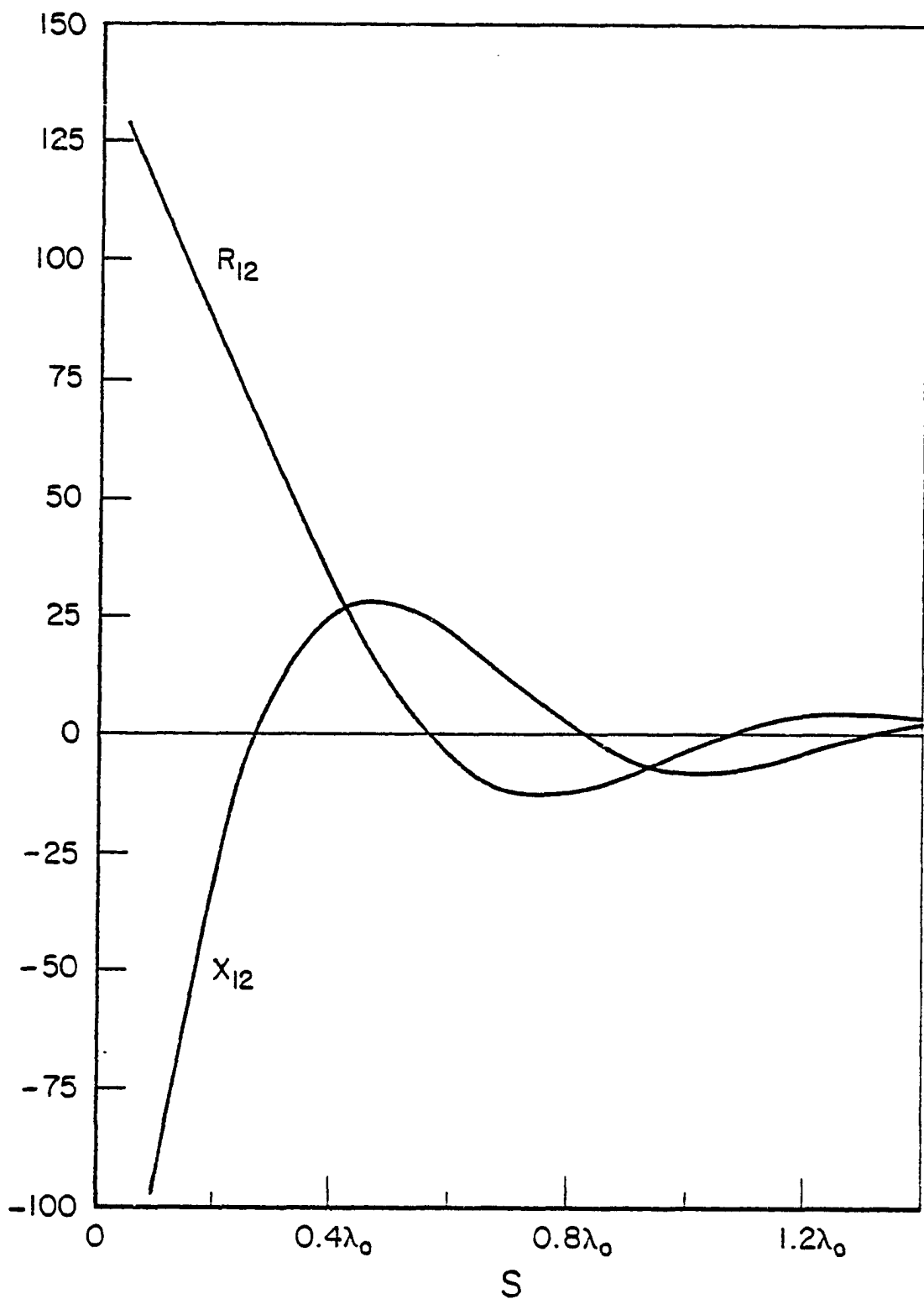


Fig. 17. Mutual Impedance between two Broadside Dipoles vs S (in λ_0), ($B=0.1016\lambda_0$, $\epsilon_r=3.25$, $L=0.4167\lambda_0$)

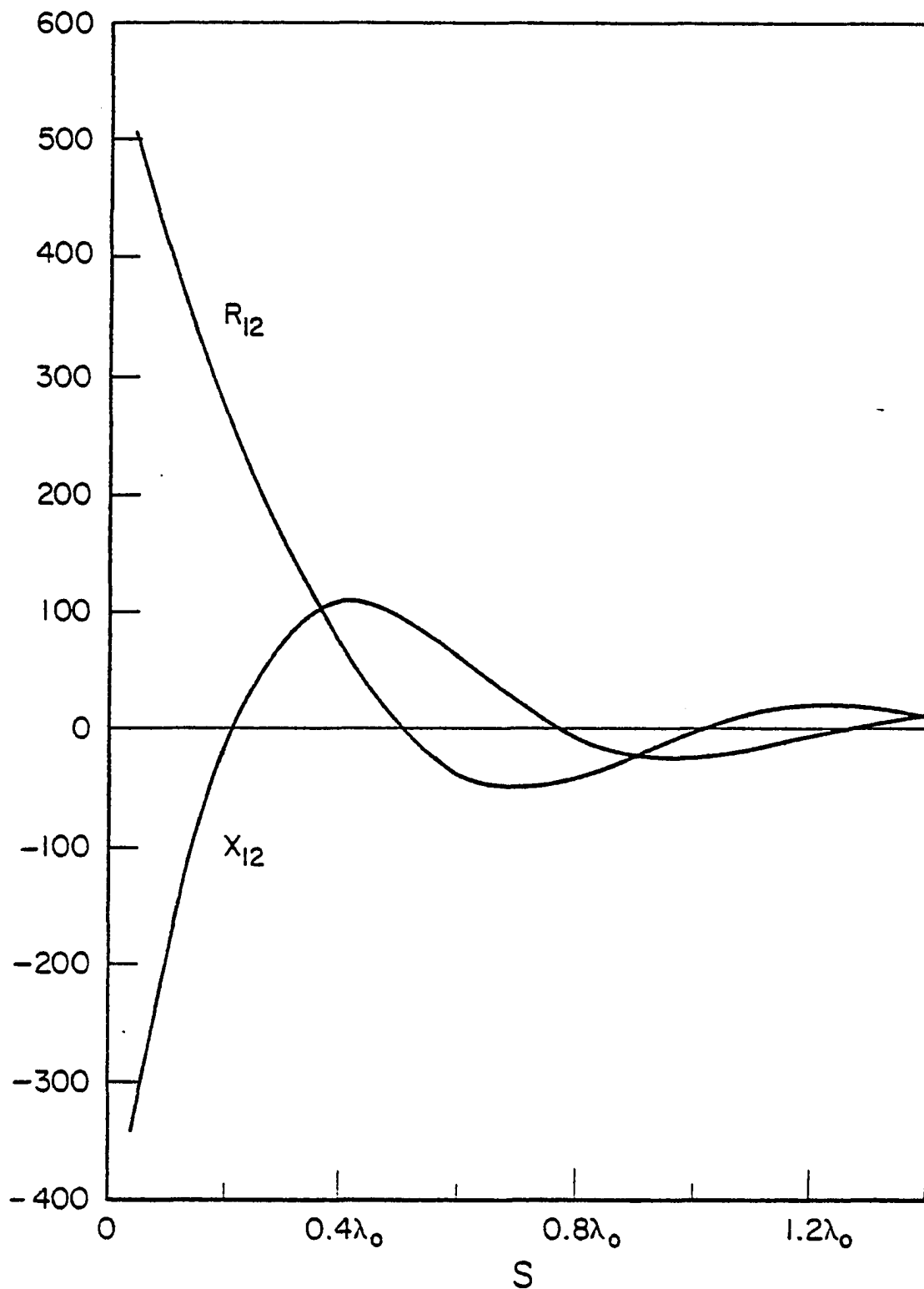


Fig. 18. Mutual Impedance between two Broadside Dipole vs
 S (in λ_0), ($B=0.1016\lambda_0$, $\epsilon_r=3.25$, $L=0.5\lambda_0$)

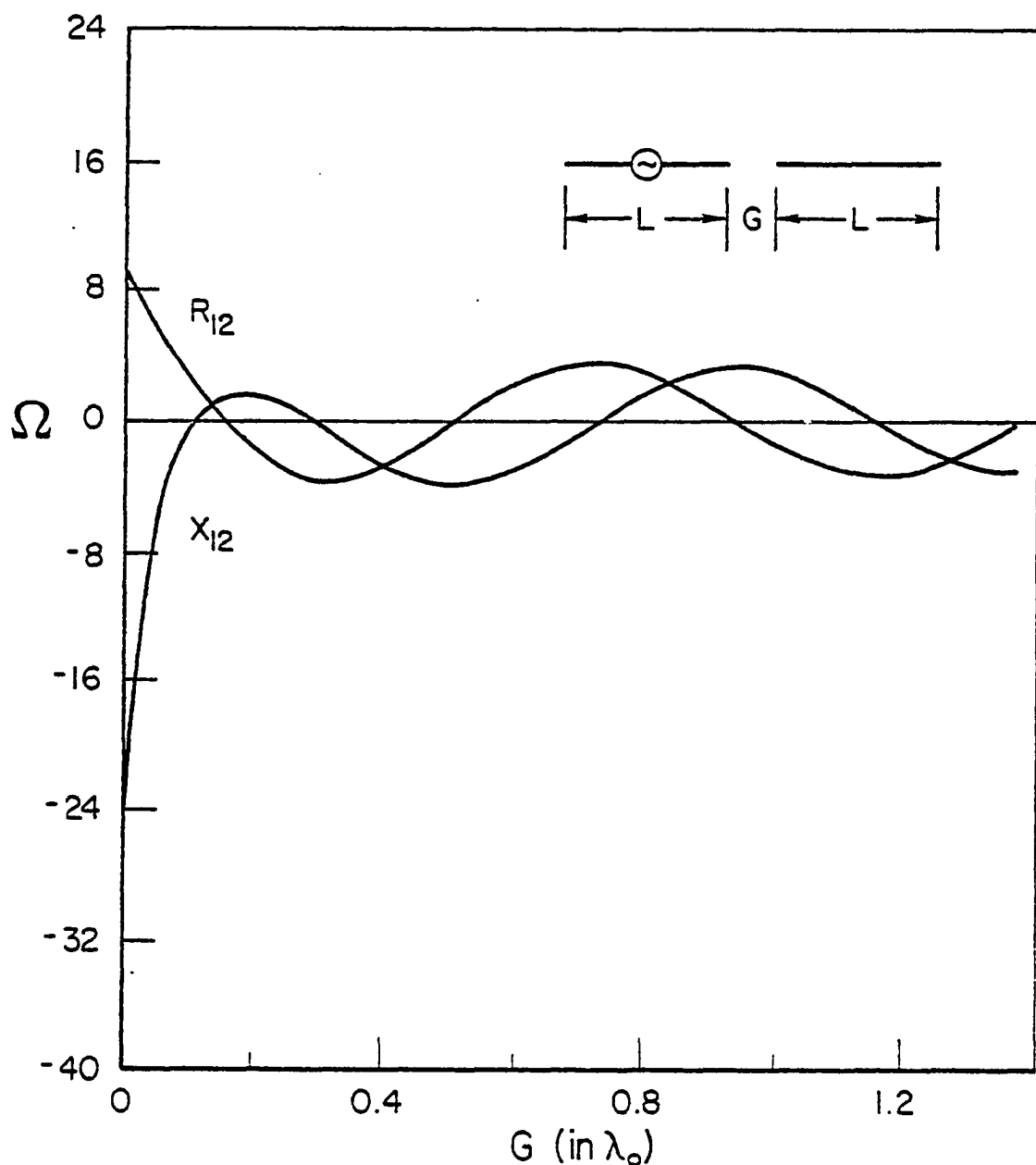


Fig. 19. Mutual Impedance between two Collinear Dipoles vs G (in λ_0), ($B=0.1016\lambda_0$, $\epsilon_r=3.25$, $L=0.25\lambda_0$)

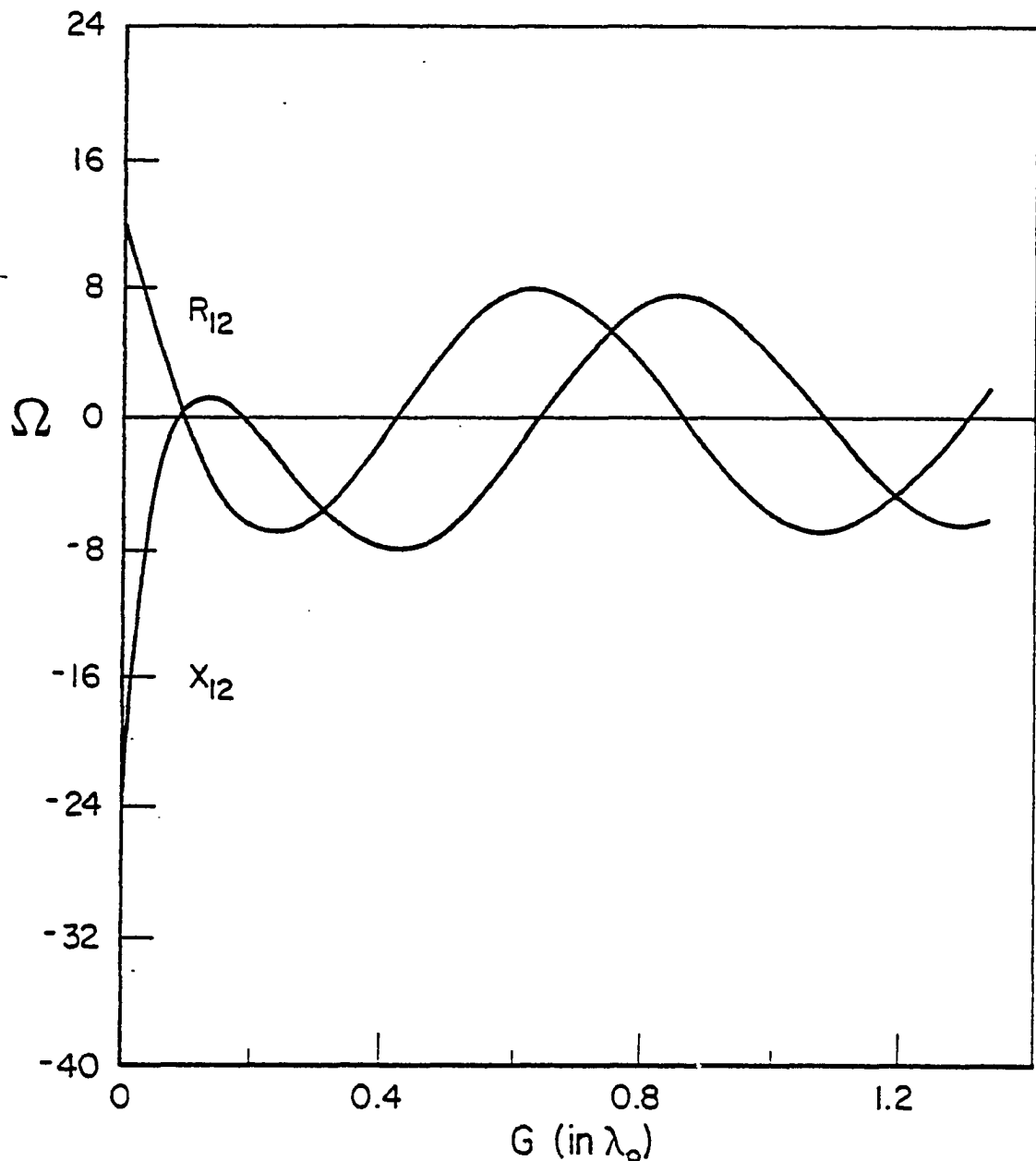


Fig. 20. Mutual Impedance between two Collinear Dipoles vs
 G (in λ_0), ($B=0.1016\lambda_0$, $\epsilon_r=3.25$, $L=0.33\lambda_0$)

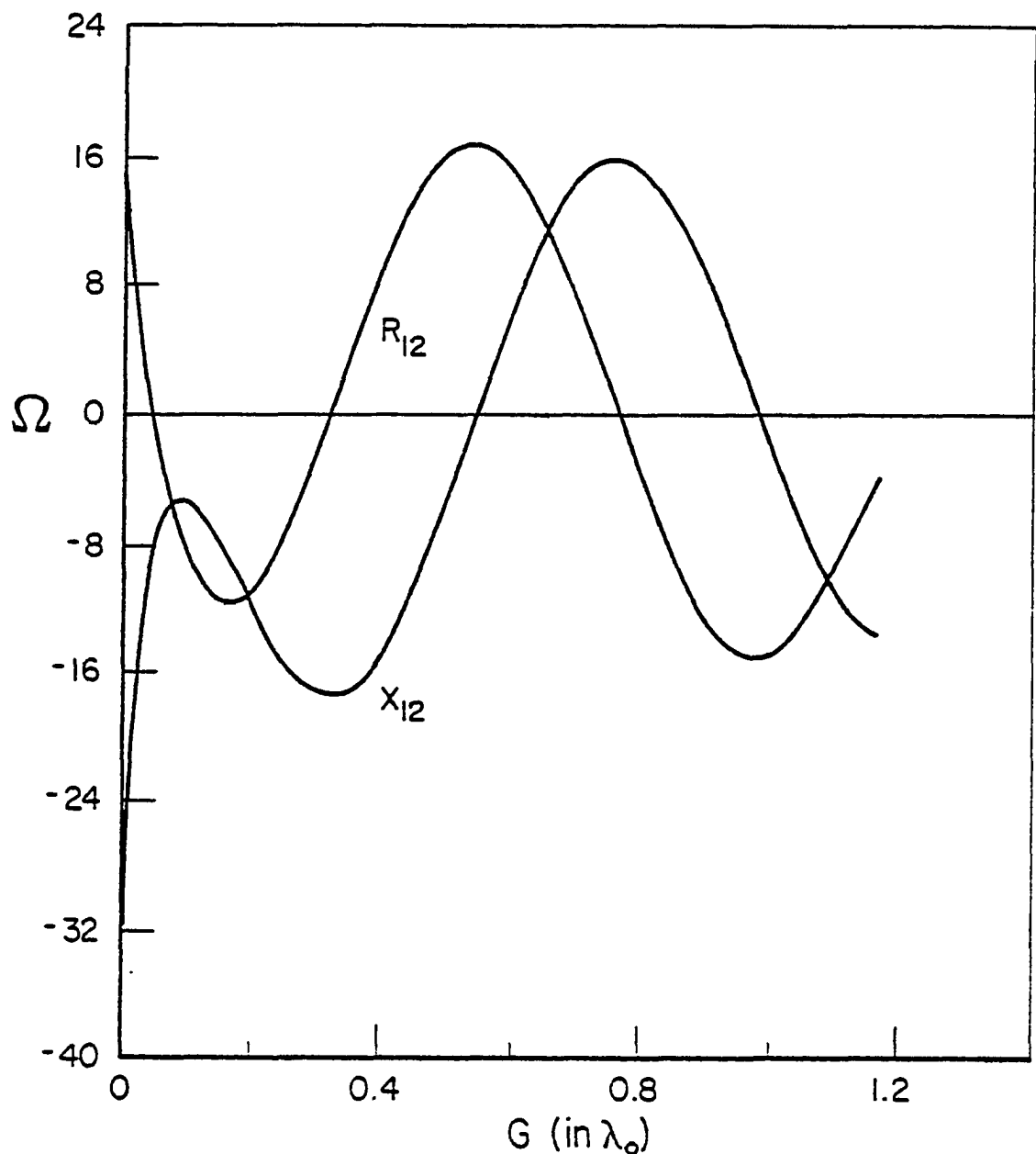


Fig. 21. Mutual Impedance between two Collinear Dipoles vs G (in λ_0), ($B=0.1016\lambda_0$, $\epsilon_r=3.25$, $L=0.4167\lambda_0$)

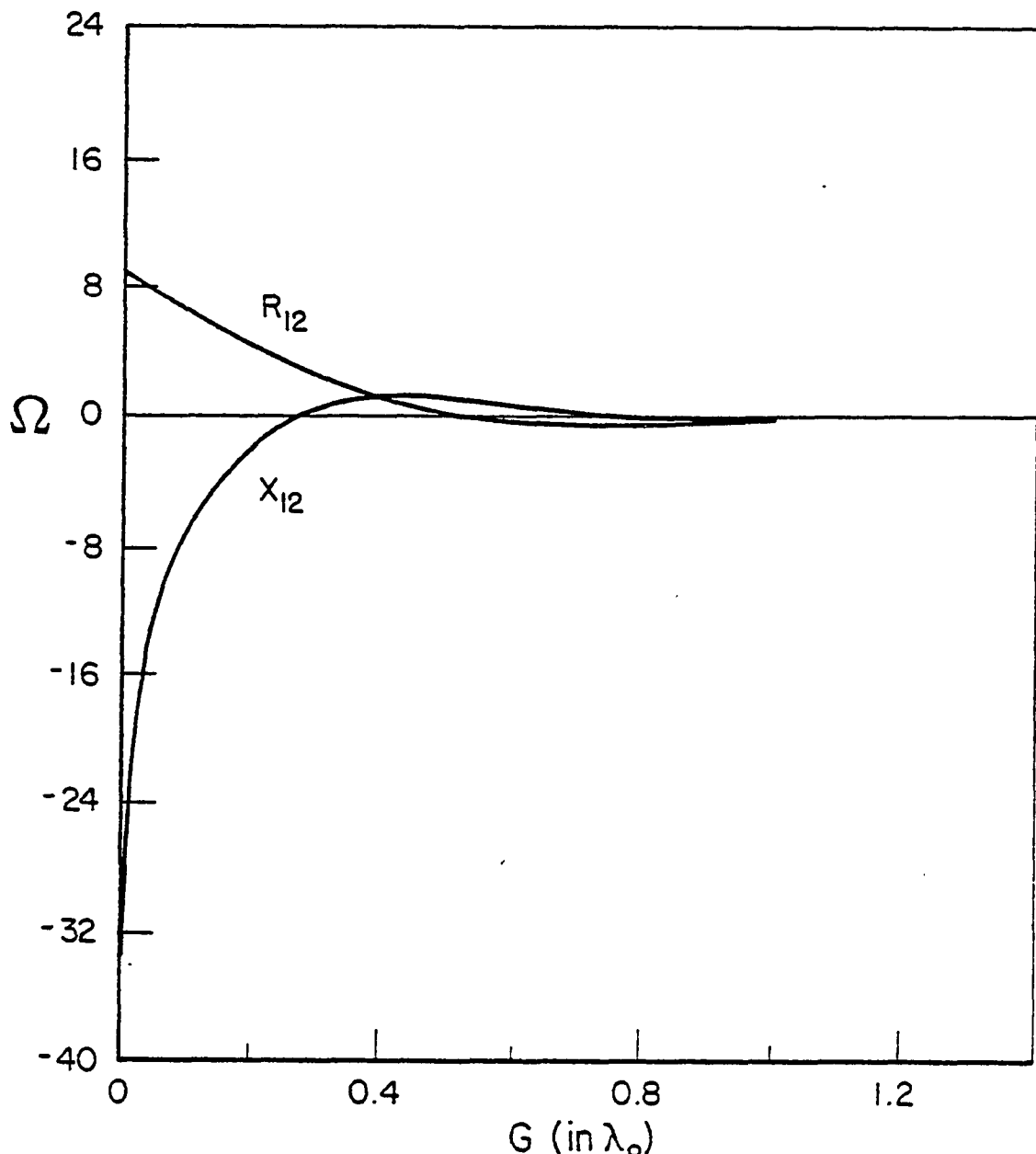


Fig. 22. Mutual Impedance between two Collinear Dipoles vs G (in λ_0), ($B=0.1016\lambda_0$, $\epsilon_r=1.0$, $L=0.4167\lambda_0$)

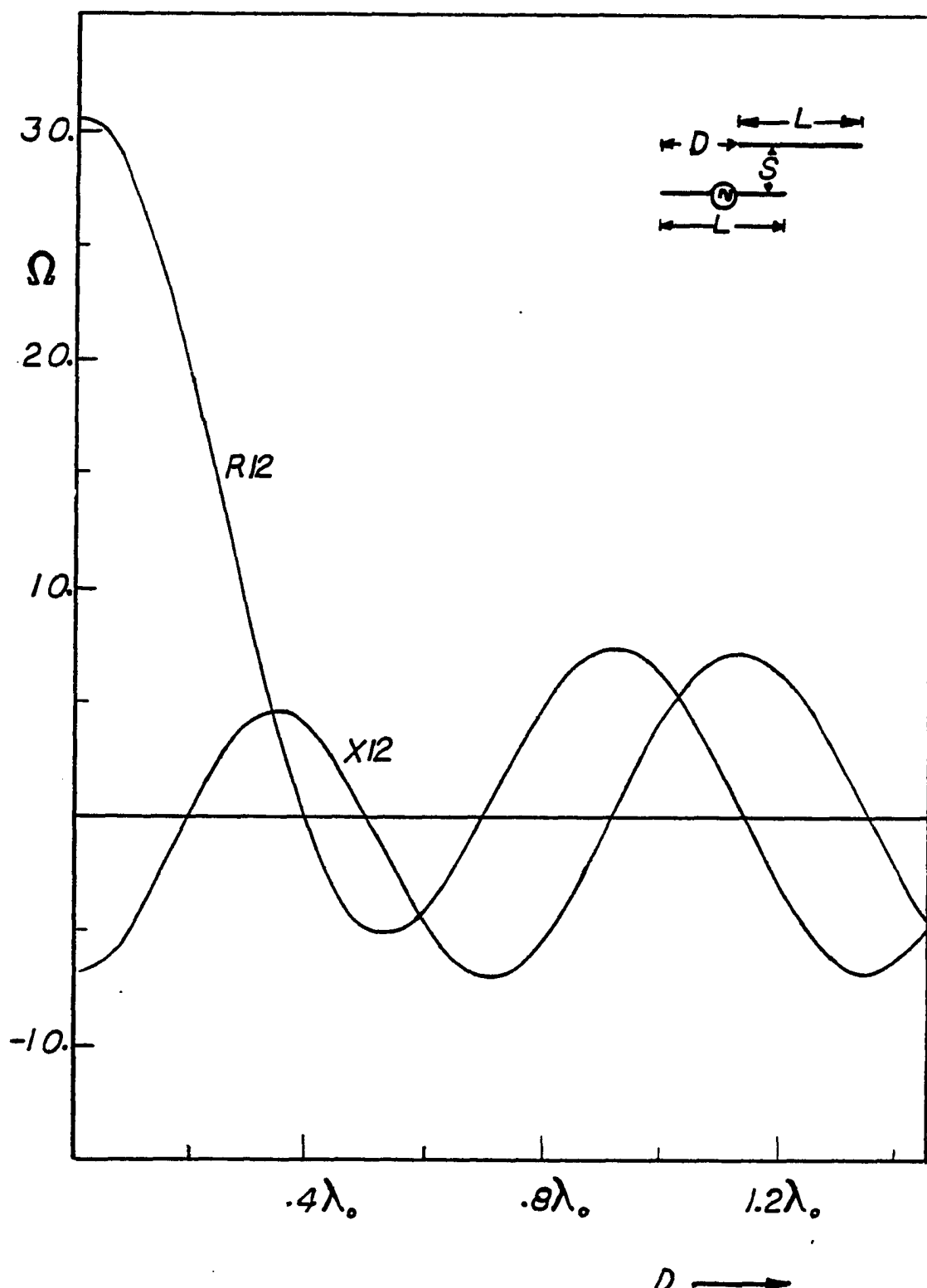


Fig. 23. Mutual Impedance between two Dipoles in Echelon vs D (in λ_0), ($B=0.1016\lambda_0$, $\epsilon_r=3.25$, $L=0.333\lambda_0$, $S=0.25\lambda_0$)

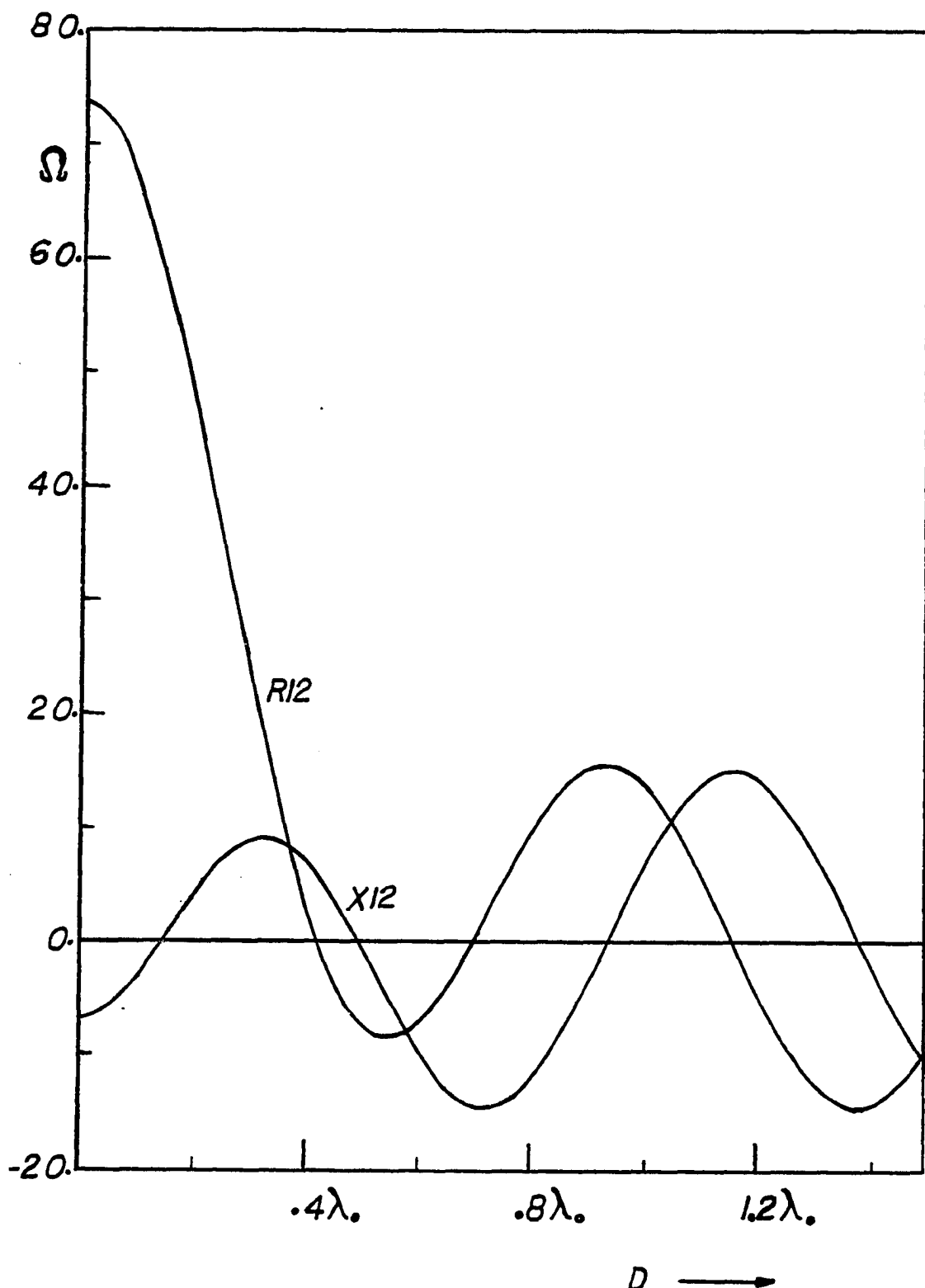


Fig. 24. Mutual Impedance between two Dipoles in Echelon vs D (in λ_0), ($B=0.1016\lambda_0$, $\epsilon_r=3.25$, $L=0.4167\lambda_0$, $S=0.25\lambda_0$)

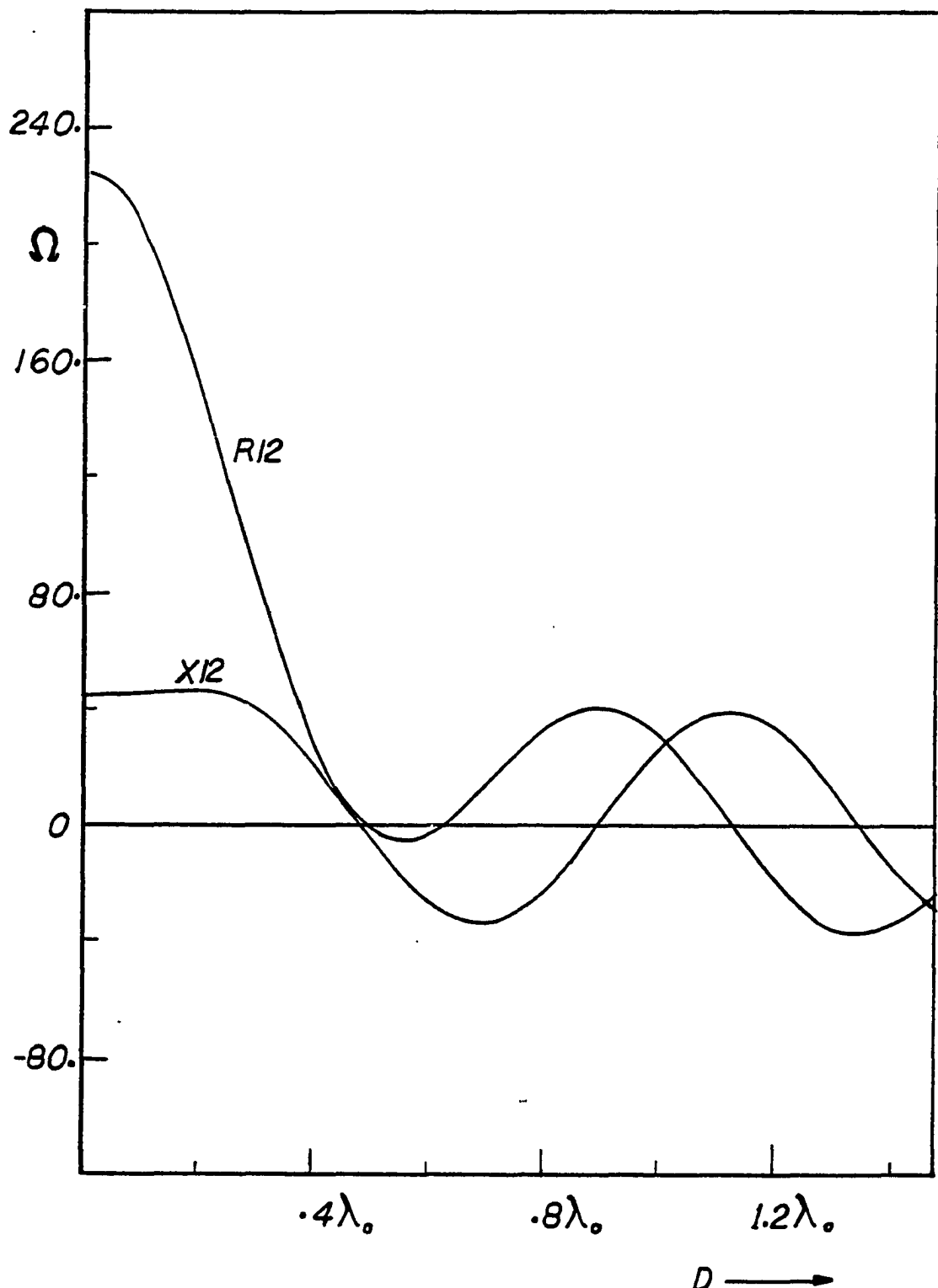


Fig. 25. Mutual Impedance between two Dipoles in Echelon vs D (in λ_0), ($B=0.1016\lambda_0$, $\epsilon_r=3.25$, $L=0.5\lambda_0$, $S=0.25\lambda_0$)

period of oscillation of the mutual impedance as obtained from Fig. 19 is $0.88\lambda_0$, while the wavelength of the excited surface wave as obtained from the computer program is $0.8811\lambda_0$. This agreement is excellent and confirms that mutual coupling for the collinear configuration is only due to the TM mode of the surface waves. The initial behavior for small G is due to the near zone field of the dipoles, as is clear from Fig. 22.

In the echelon configuration, mutual impedance computations versus displacement D are shown in Figs. 23 through 25 for different dipole lengths. For $D=0\lambda_0$, the dipoles are in the broadside configuration, while for D large, the dipoles are approximately collinear. As D increases, Z_{12} decreases rapidly from the broadside value and ultimately shows the same behavior, as shown by the dipoles in collinearity.

The efficiency of the surface wave excitation depends upon the thickness of the substrate B (i.e., aperture size), for a given dielectric constant ϵ_r . To observe this effect, the substrate thickness is next increased from $0.1016\lambda_0$ to $0.127\lambda_0$, and computations for mutual impedance between the dipoles in collinear arrangement are performed. The results are shown in Figs. 26 and 27. These results are compared with the ones shown in Figs. 20 and 21. The comparison indicates that the surface wave launching efficiency increases with the thickness of the substrate.

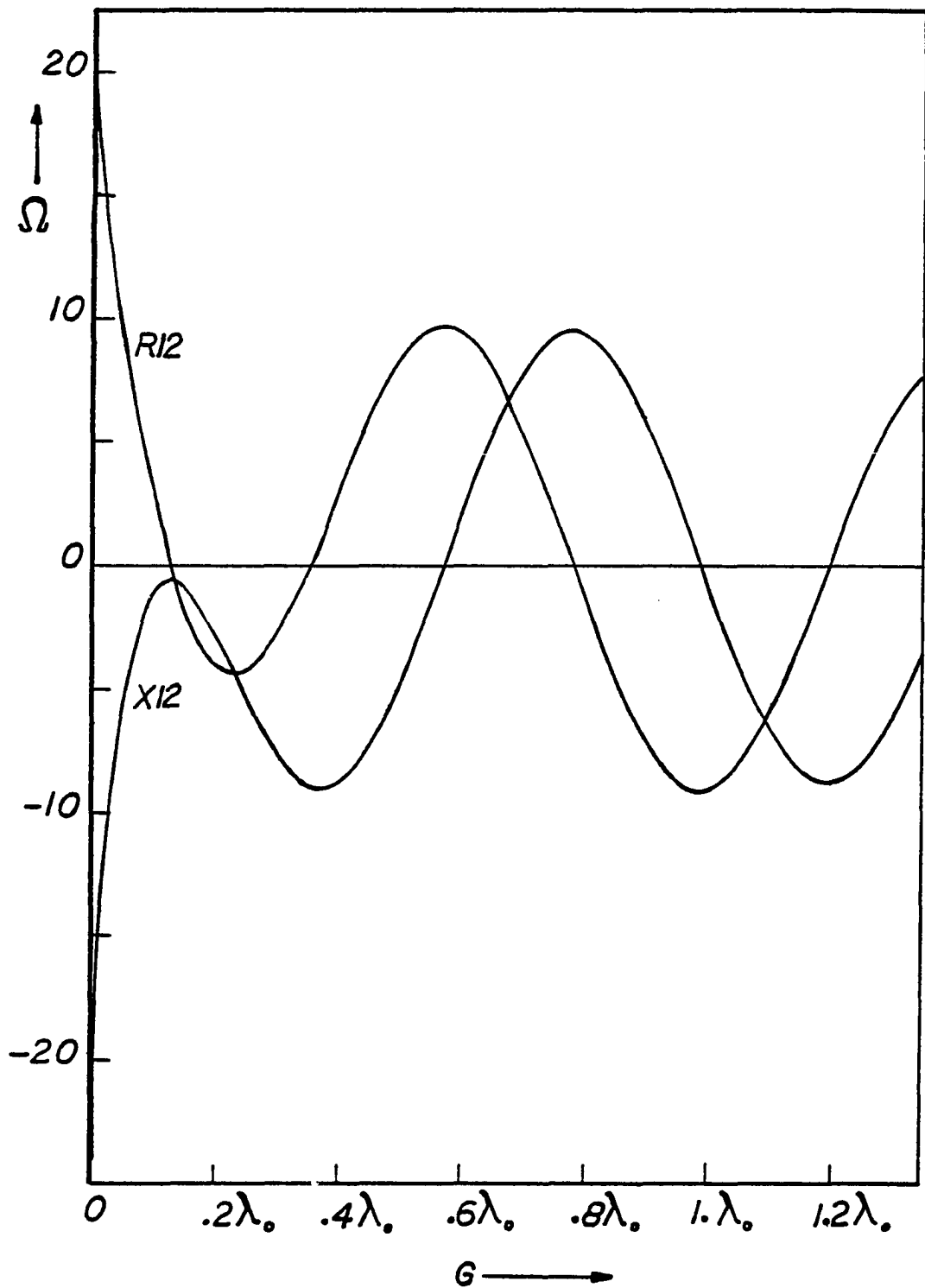


Fig. 26. Mutual Impedance between two Collinear Dipoles vs
 G (in λ_0), ($B=0.1016\lambda_0$, $\epsilon_r=3.25$, $L=0.3\lambda_0$)

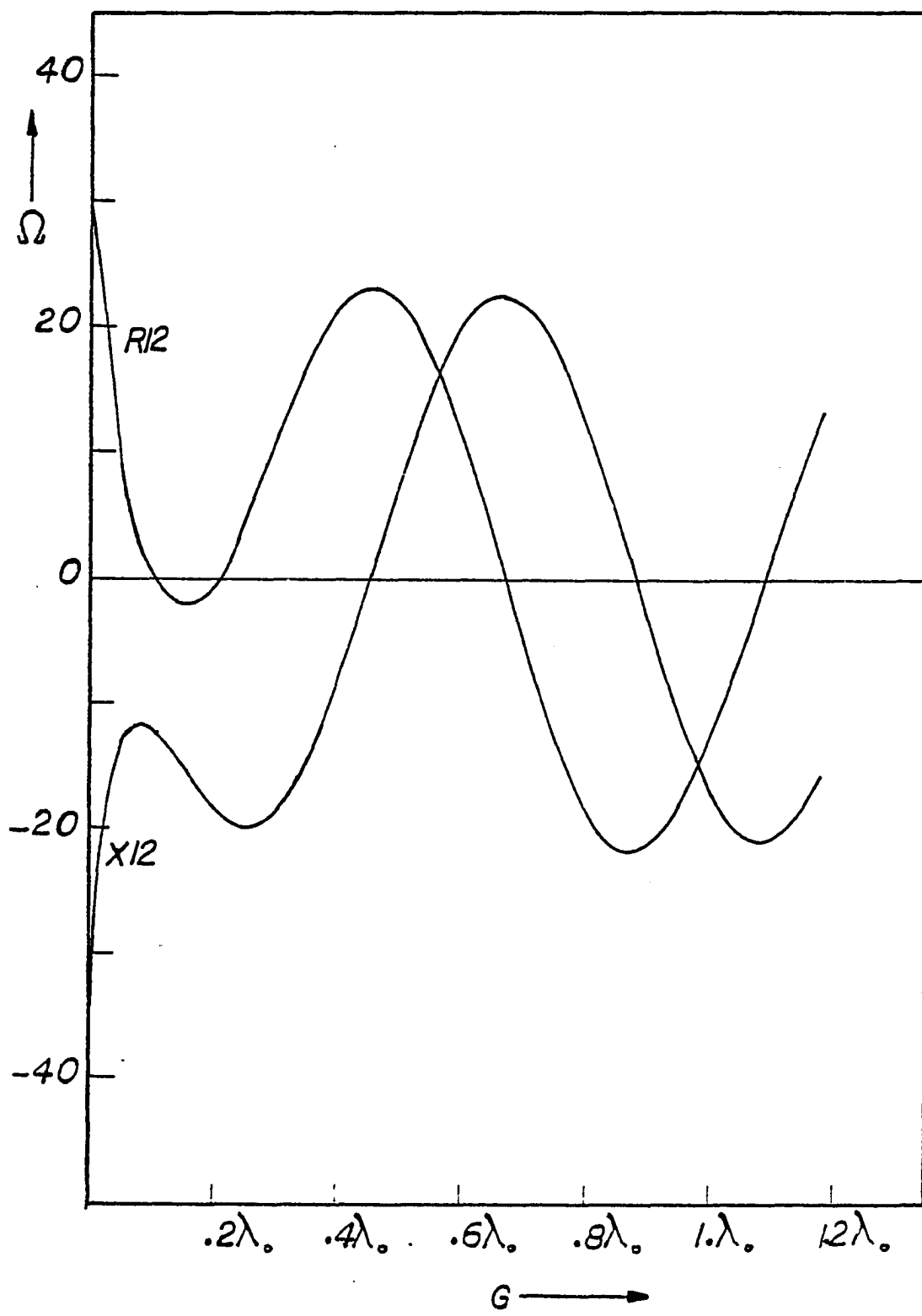


Fig. 27. Mutual Impedance between two Collinear Dipoles vs G (in λ_0), ($B=0.127\lambda_0$, $\epsilon_r=3.25$, $L=0.4\lambda_0$)

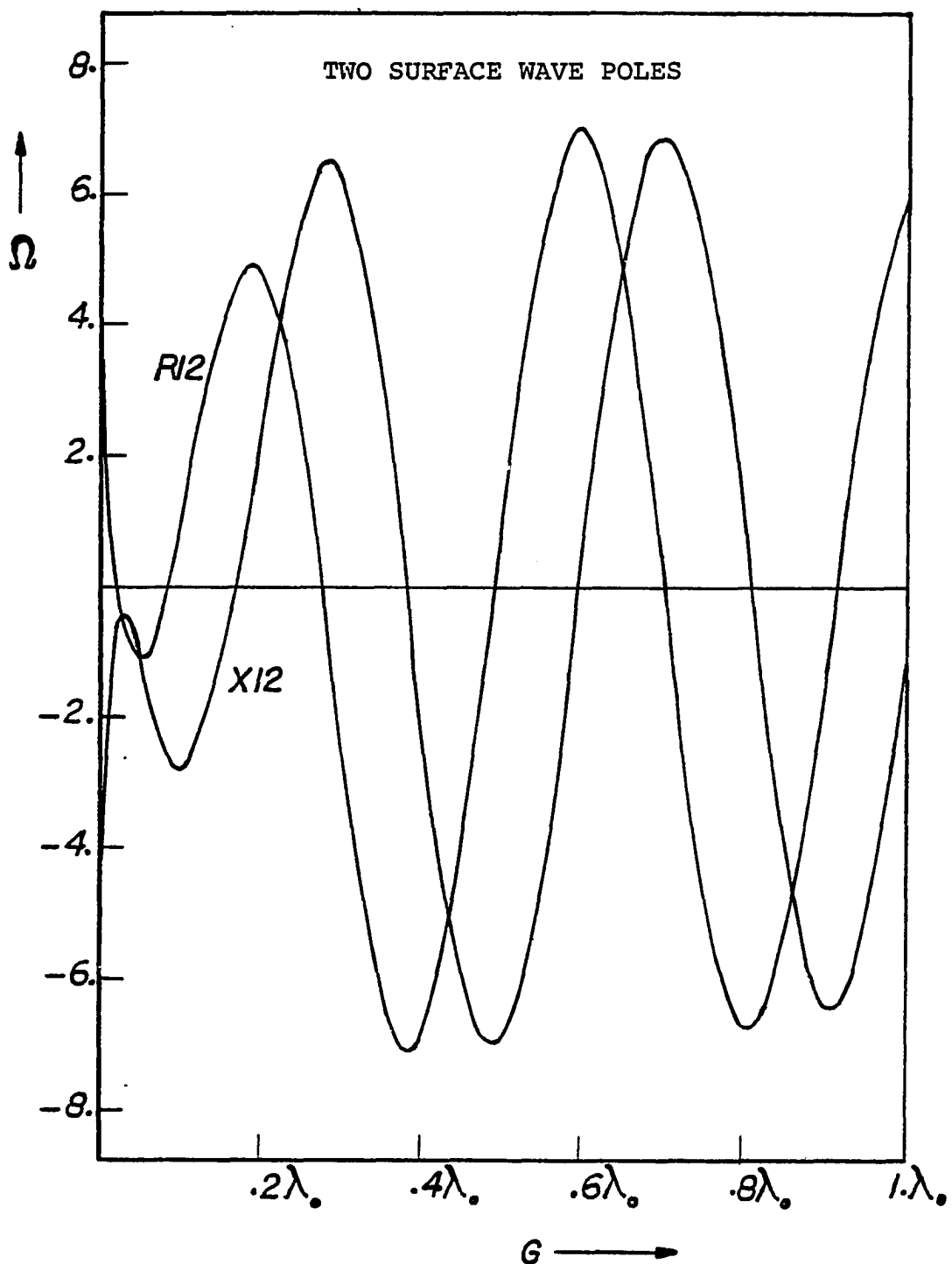


Fig. 28. Mutual Impedance between two Collinear Dipoles vs G (in λ_0), ($B=0.1016\lambda_0$, $\epsilon_r=8.5$, $L=0.25\lambda_0$)

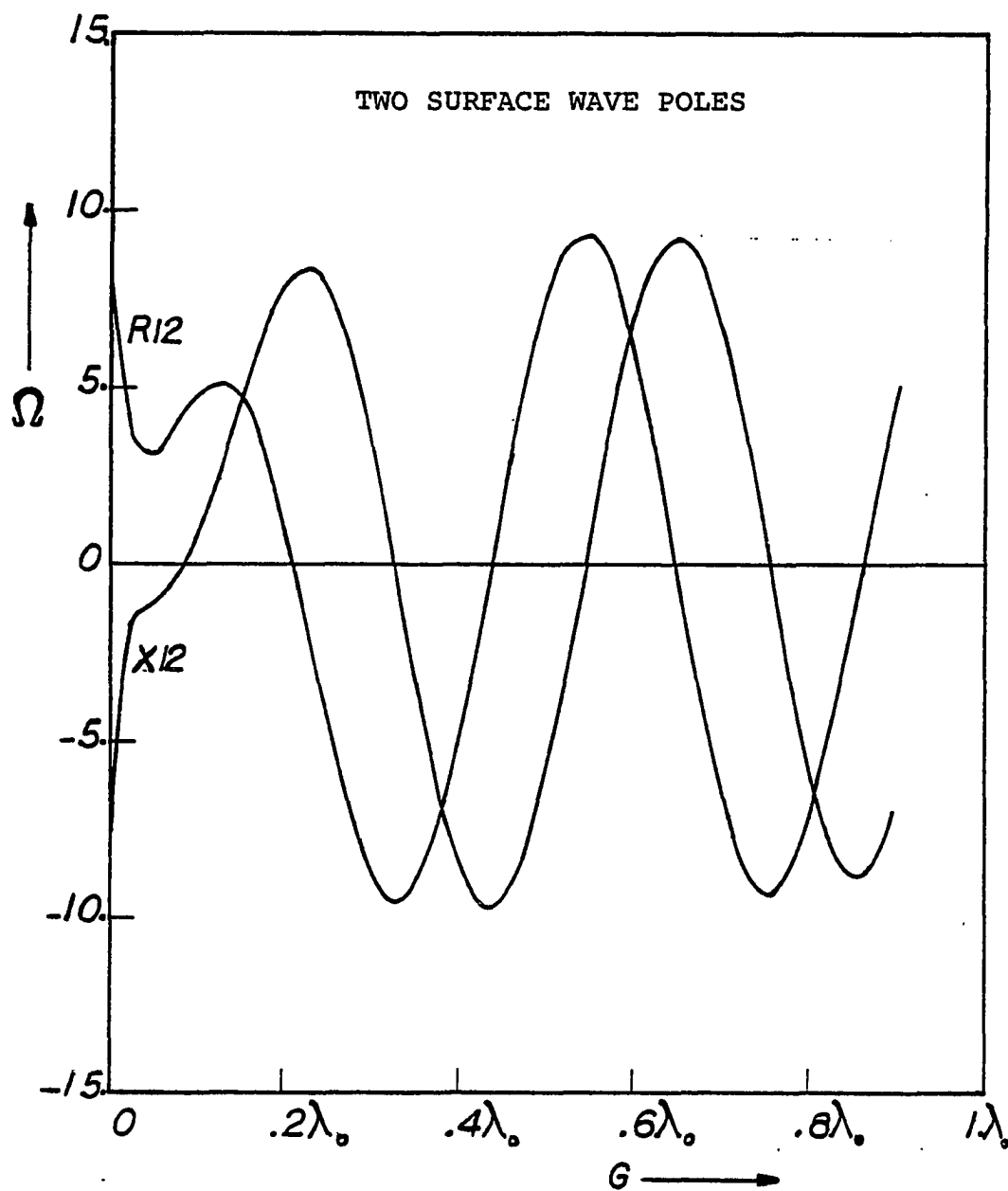


Fig. 29. Mutual Impedance between two Collinear Dipoles vs G (in λ_0), ($B=0.15\lambda_0$, $\epsilon_r=8.5$, $L=0.3\lambda_0$)

Next, two propagating surface wave modes are allowed by increasing the substrate thickness to $0.15\lambda_0$ and dielectric constant to 8.5. Computations for dipoles in broadside and collinear configuration are performed. The results for collinear arrangement for different dipole lengths are shown in Figs. 28 and 29. The following comments are in order:

- 1) The period of oscillation of the mutual impedance between two collinear dipoles as obtained from the graph is $0.42\lambda_0$, while the wavelength of the TM mode from the computer program, is $0.408\lambda_0$. This agreement is good and proves that the coupling in collinear arrangement is dominantly due to the TM mode of the surface waves.
- 2) Mutual coupling is small. This is due to the fact that most of the surface wave power carried by this mode, flows inside the dielectric substrate.

For the broadside situation the results are shown in Figs. 30 and 31. The following points are noted:

- 1) The mutual impedance plot oscillates with a period of $0.566\lambda_0$, which is close to the wavelength of the TE mode of the surface waves i.e., $0.553\lambda_0$. This proves that mutual impedance in the broadside configuration is mainly due to the TE mode of the surface waves.
- 2) The decay in coupling is rather rapid as compared to the collinear case.

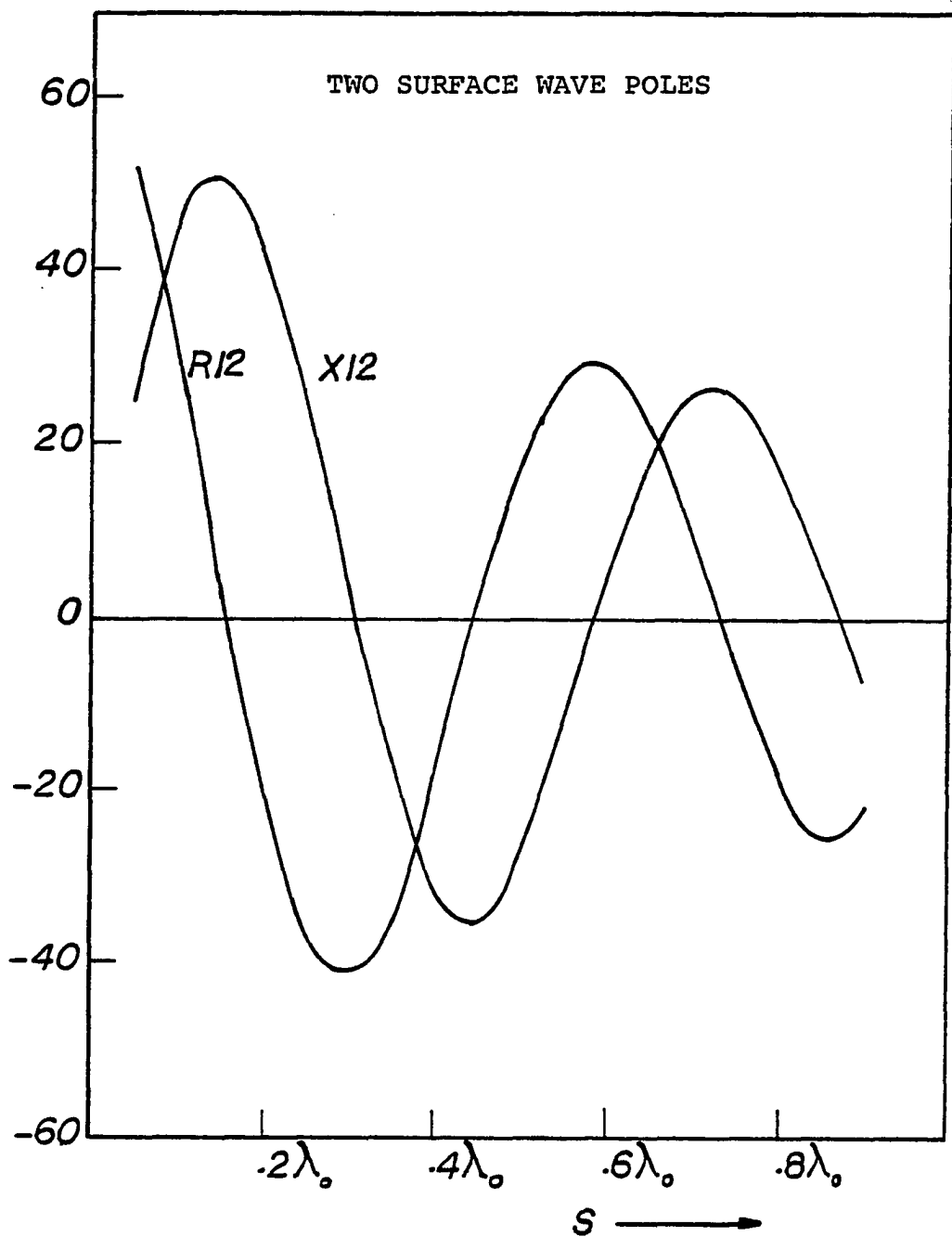


Fig. 30. Mutual Impedance between two Broadside Dipoles vs S (in λ_0), ($B=0.15\lambda_0$, $\epsilon_r=8.5$, $L=0.25\lambda_0$)

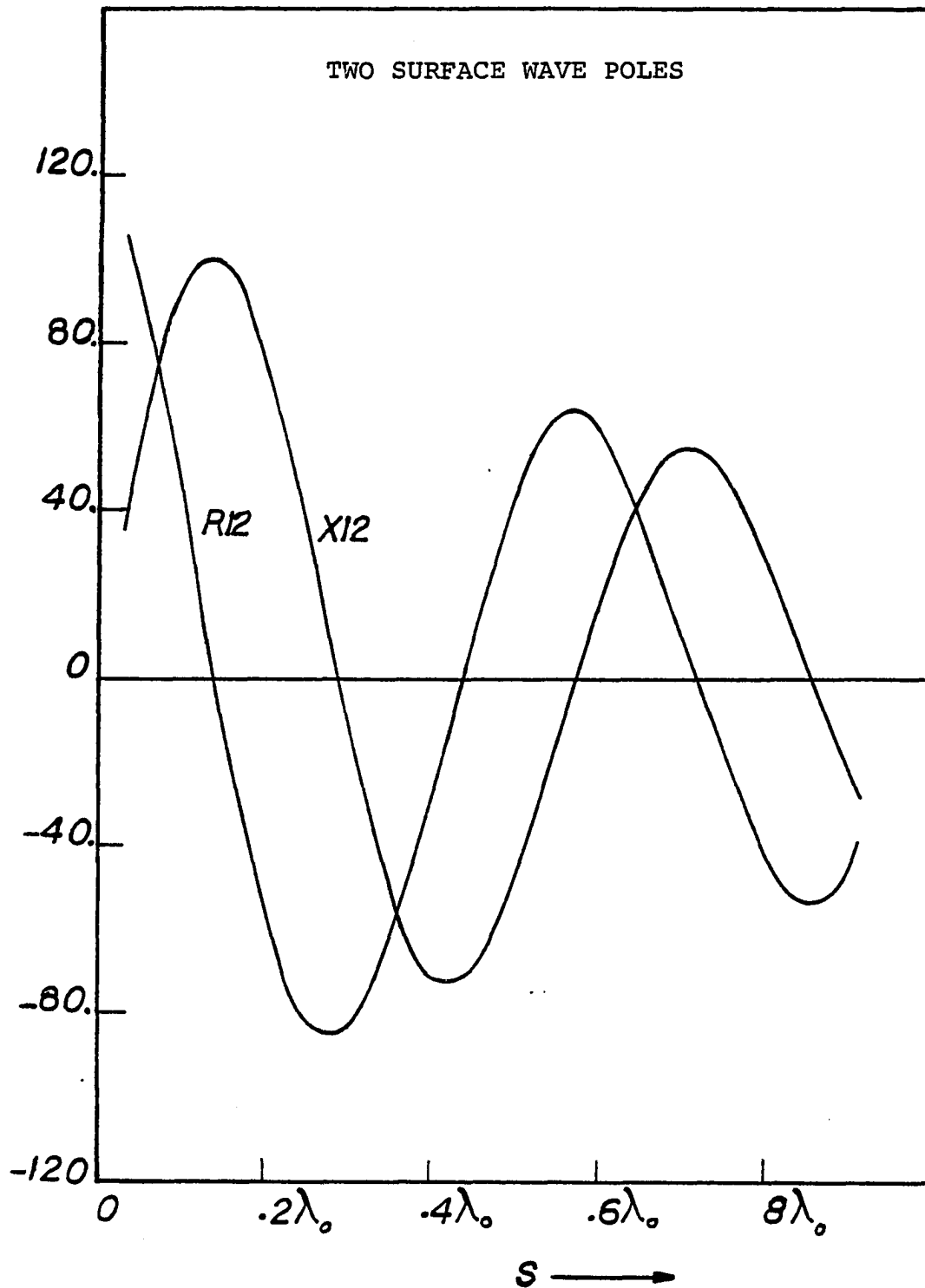


Fig. 31. Mutual Impedance between two Broadside Dipoles vs S (in λ_0), ($B=0.15\lambda_0$, $L=0.3\lambda_0$, $\epsilon_r=8.5$)

Chapter IV

PRINTED PARASITIC ARRAYS

When a dipole is printed on a grounded substrate, it is no longer as good a radiator as it is in free space. Looking at the radiation pattern of a printed dipole, shown in Fig. 13, it is obvious that the dipole radiates maximum power along $\theta = 0^\circ$ direction. Near the interface $\theta = \pm 90^\circ$ and $\phi = 90^\circ, 270^\circ$, the dipole excites direct, higher order and leaky waves (for single propagating mode). Along $\theta = \pm 90^\circ$ and $\phi = 0^\circ, 180^\circ$ planes, the dipole launches surface waves.

If another dipole is printed broadside to this dipole, direct, higher order and leaky wave modes couple energy with this parasitic dipole and some energy is also coupled by the surface wave. In order to couple more power from the surface wave, it is necessary to place the parasitic dipoles in collinearity with the driven dipole. Based on these two coupling mechanisms, two types of parasitic arrays (Printed Yagi-Uda array and Collinear array) are investigated in this chapter. The Printed Yagi-Uda array makes use of the direct, higher order and leaky wave modes coupling whereas in the Collinear array the coupling between the elements is dominantly due to the surface waves.

The technique described in Chapter II to treat the printed wire antenna is extended to analyze the Patch antenna. The current distribution on this class of printed antenna is of two dimensional nature and therefore a dyadic

Green's function is to be used. A brief list of the problems which can be solved by this methodology is also included.

4.1 PRINTED YAGI-UDA ARRAY:

The Yagi-Uda array in free space [23] has been very popular for the last fifty years. The printed Yagi-Uda array is of great practical importance especially where conformal antennas are needed. In this section, a design of a printed Yagi array has been presented.

Considerable insight about the printed Yagi array can be gained by considering the case of a broadside printed dipole pair a distance d apart. This arrangement is diagrammatically explained in Fig. 32. Dipole #1 is driven, while dipole #2 is acting as a parasitic. The radiation characteristics of the printed dipole pair are controlled by three parameters, i.e., the distance between the dipoles d and the lengths of the dipoles L_1 and L_2 . To obtain a first order estimate for d , it is assumed that $L_1 = L_2 = L_r$, where L_r is the resonant length of the dipole for a given B and ϵ_r .

The array factor $A(\theta)$ is given by,

$$A(\theta) = 1 + (I_2/I_1) \cdot \exp(-jk\sin\theta)$$

It is clear from the above equation that the shape of the pattern is controlled by the spacing d and by the ratio I_2/I_1 . Since the ratio I_2/I_1 is determined by d , therefore,

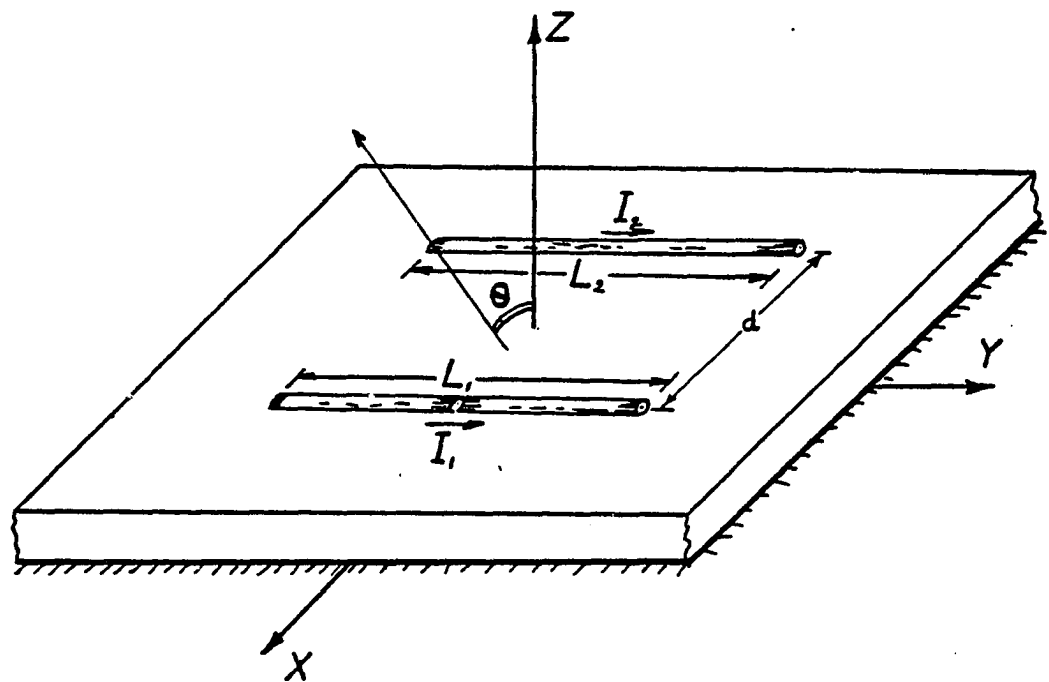


Fig. 32. Driven and Parasitic Dipole pair

using the method illustrated in Section 3.1, for a set of values of d , corresponding values of I_2/I_1 are computed. The thickness and dielectric constant of the substrate is chosen $0.1016\lambda_0$ and 3.25 respectively. The resonant length L_r of the printed dipole is found to be about $0.333\lambda_0$ as obtained from Fig. 9.

It is required that the pair should radiate more power in the forward direction ($0^\circ > \theta > -90^\circ$) than in the backward direction ($0^\circ < \theta < 90^\circ$). The H-plane radiation pattern of the printed dipole (see Fig. 13) shows two minima for $\theta = \pm 90^\circ$ and a maximum for $\theta = 0^\circ$. Thus, in order to increase radiation in the forward direction, a minimum must be placed at approximately $\theta = 45^\circ$. The final goal is to get the main beam close to $\theta = -90^\circ$ with low sidelobes. The magnitude and position of the minimum is given by,

$$A_{\min} = 1 - |I_2/I_1|$$

and

$$\theta_{\min} = \sin^{-1} [(I_2/I_1 - \pi)/kd]$$

respectively.

Table II shows the position of the minimum and front-to-back ratio for different values of the d . The positions of the corresponding maxima are in the imaginary plane. For comparison purposes, the magnitude of the array factor $A(\theta)$, is taken as a measure of forward fire and backward fire corresponding to the values of $\theta = -45^\circ$

TABLE II

Front to back ratio for different values of displacement d.

d	θ_{\min}	A_{\min}	$A_f = A(-45^\circ)$	$A_b = A(45^\circ)$	Ratio = A_f/A_b
$0.10\lambda_0$	9.55°	-16.45 dB	-5.65 dB	-9.21 dB	3.56 dB
$0.15\lambda_0$	17.05°	-10.04 dB	-1.78 dB	-6.95 dB	5.17 dB
$0.25\lambda_0$	26.20°	-5.09 dB	2.39 dB	-4.13 dB	<u>7.07 dB</u>
$0.30\lambda_0$	28.84°	-3.87 dB	1.97 dB	-3.25 dB	5.22 dB

and $\theta = 45^\circ$ respectively. The ratio of these values is taken as front-to-back ratio.

From the Table II it is clear that for $d = 0.1\lambda_0$, the minimum lies very close to broadside i.e., $\theta=0^\circ$. This results in two main beams near endfire ($\theta = \pm 90^\circ$) as is obvious from Fig. 33. By shifting the position of the minimum towards endfire, backfire is reduced and at the same time the forward beam starts moving towards broadside. It is not desirable for the minimum to be close to endfire ($\theta = 90^\circ$) because the element pattern has already a minimum for $\theta = 90^\circ$. An optimum position of the minimum should be close to $\theta = 45^\circ$.

It is also obvious from Table II that a maximum front-to-back ratio is obtained for displacement $d = 0.25\lambda_0$. Knowing a first order guess for d , the lengths are perturbed in order to obtain maximum value of front to back ratio, with the main beam pointing close to endfire i.e., $\theta = -90^\circ$. The use of method of moments is made to obtain optimum lengths for the obtained displacement i.e., $d = 0.25\lambda_0$. Accordingly, two dipoles of lengths $0.35\lambda_0$ each (the length being little over L_r), are chosen and each one is divided into 40 segments. The use of sinusoidal functions as current expansion, and the use of pulse functions as testing functions is made. Consequently, the impedance matrix is generated. By decreasing the number of segments each time

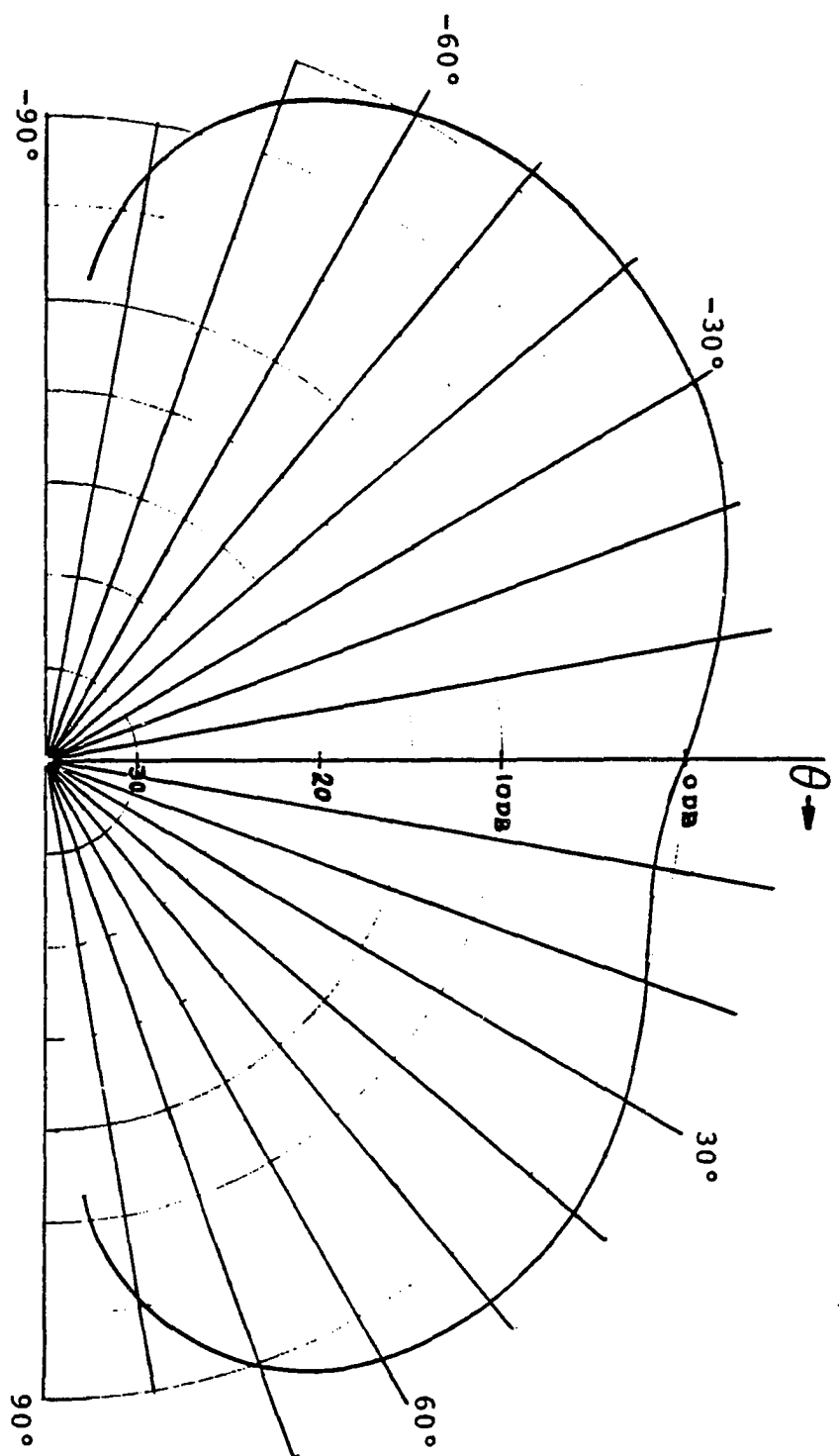


Fig. 33. H-plane Radiation Pattern of a Dipole Parasitic pair $0.1\lambda_0$ apart
 $(\epsilon_r = 3.25, L = 0.33\lambda_0, B = 0.1016\lambda_0)$

by two and inverting the resultant reduced matrix, the current distribution over the dipoles is obtained. Each computation of current distribution is followed by the calculation of the radiation pattern. As a result of this iteration, the following optimum lengths are obtained:

$$L_{exc} = 0.315\lambda_0 \quad L_{ref} = 0.3325\lambda_0$$

Front to back ratio = 7.25 dB

Position of the main beam = -33° .

Now it is required to look for an optimum director-exciter pair. Switching the position of the generator from dipole #1 to #2 and perturbing the lengths again while using the same impedance matrix, the following results are obtained:

$$L_{dir} = 0.2975\lambda_0 \quad L_{exc} = 0.315\lambda_0$$

Front to back ratio = 10.0 dB

Position of the main beam = -25° .

The director exciter and reflector are now put together keeping the distance between them $d=0.25\lambda_0$, and their lengths same as found above. A new impedance matrix is generated and the current distribution over the array is obtained which is shown in Fig. 34. The current distribution leads to the radiation pattern computations and the following results are noted:

Position of the main beam = -37° .

Front-to-back ratio = 14.4 dB.

Input impedance of the array = $28.41 + j4.5 \Omega$.

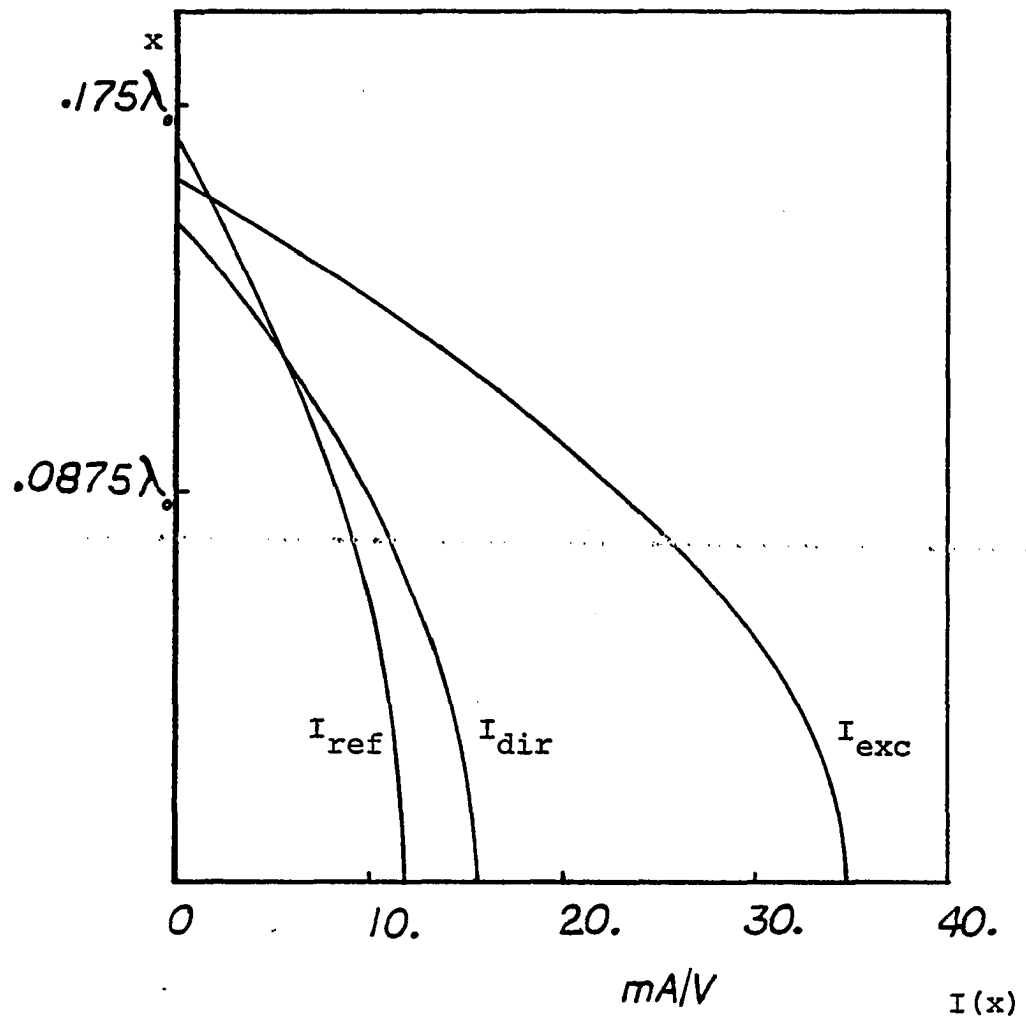


Fig. 34. Current Distribution on 3-element Yagi-Uda Array
vs x ($B = 0.1016\lambda_0$, $\epsilon_r = 3.25$)

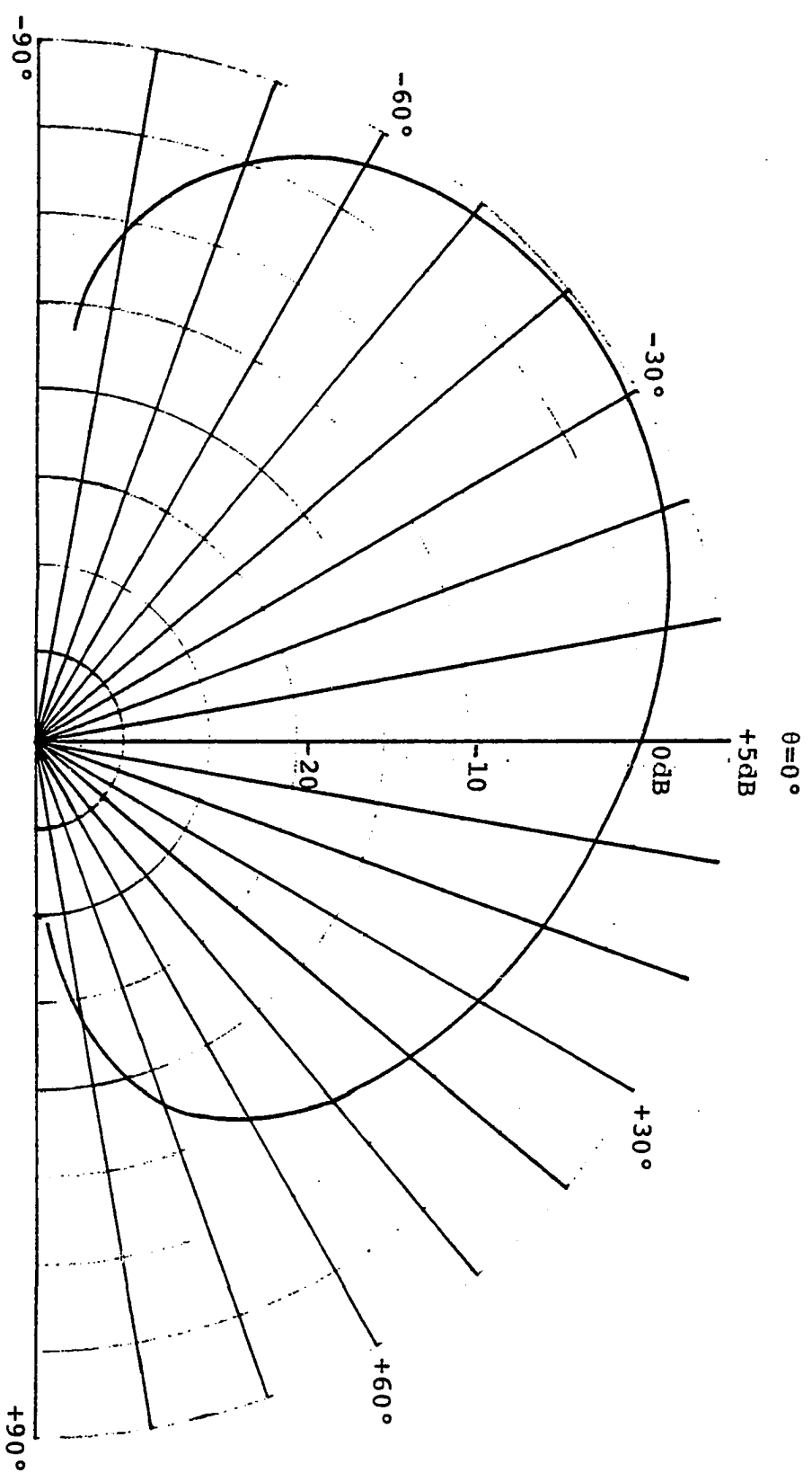


Fig. 35. Radiation pattern of 3-element Yagi-Uda Array, ($B=0.1016\lambda_0$, $\epsilon_r=3.25$)

The radiation pattern is shown in Fig. 35. The main beam is a little bit broader. This is because the element pattern has maximum for $\theta = 0^\circ$. Moreover the main beam is not close to endfire. To improve these shortcomings more directors are needed. Therefore one more director of length $0.28\lambda_0$ is added. The following results are noted:

Position of the main beam = -42° .

Front to back ratio = 11.3 dB.

Input impedance of the array = $26.66 + j1.85 \Omega$.

The radiation pattern of the 2-director array is shown in Fig. 36. The main beam moves by 5° towards endfire with the addition of one director. However, the front to back ratio has deteriorated by 3.1 dB. This can be improved by further optimizing the length and position of the reflector. A null in the radiation pattern also started to appear at about $\theta = 27^\circ$.

The addition of directors results in a surface wave generation which propagates down the array. Variations in the length and spacing of the directors results in change in the phase velocity of the surface wave. This could also be used as a design criterion [24].

The vector diagram for the 3-element and 4-element array are shown in Fig. 36. There is a marked improvement in the directivity of the dual director array as compared to the single director array. The vector diagram further shows that addition of more directors will increase the

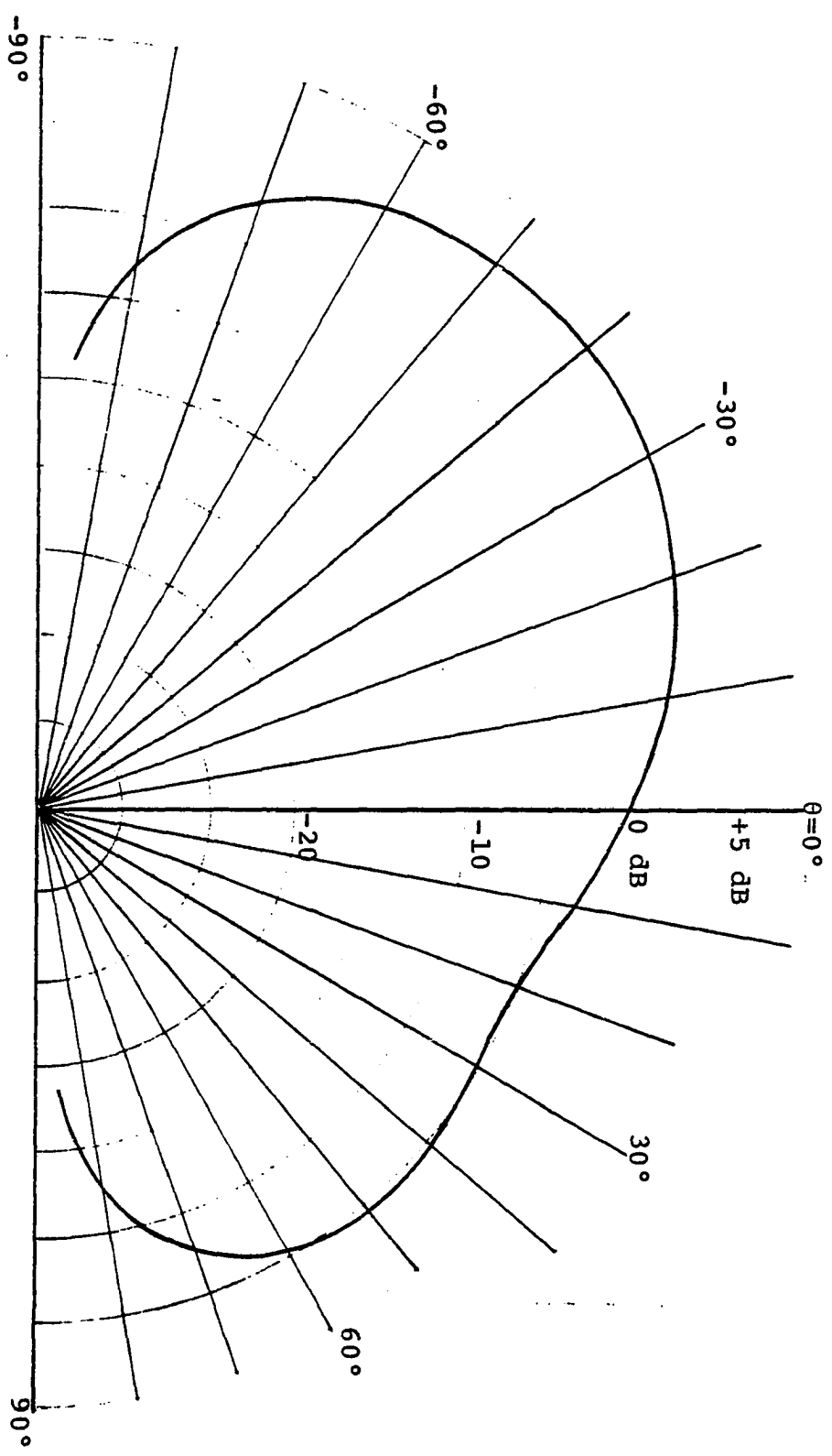


Fig. 36. Radiation pattern of 4-element Printed Yagi-Uda Array, ($B=0.1016\lambda_0$, $\epsilon_r=3.25$)

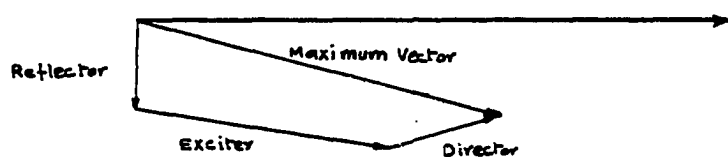


Fig. 37a. Vector Diagram of Single Director Printed Yagi

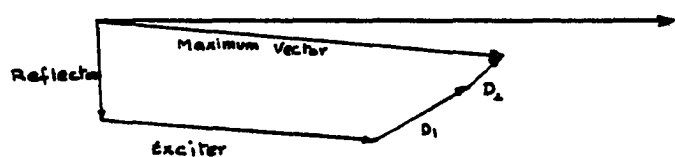


Fig. 37b. Vector Diagram of Double Director Printed Yagi

directivity. In order to improve the design further, the following suggestions are made:

- 1) The main drawback in getting a good endfire pattern is that the element pattern has a minimum in the endfire direction, while in broadside direction it has a maximum. Therefore, to improve forward fire the first director must be placed close to excitor. This will result in one minimum near broadside and two maxima in the endfire directions i.e., $\theta = -90^\circ$, and $\theta = 90^\circ$, as shown in Fig 33.
- 2) The reflector should not be placed closer than $0.2\lambda_0$.
- 3) As compared to a Yagi array in free space more directors are needed for a printed array.
- 4) More reflectors may be added to improve the front-to-back ratio.
- 5) The final taper in the array (as it is usually done in Yagi array in free space to reduce the reflection of surface wave) is not important; as, after leaving the array, the surface wave is still guided by the substrate. However, the taper at the edge of the substrate is desired as it determines the shape of the pattern.

4.2 COLLINEAR ARRAY:

Besides, being a radiator, the printed dipole acts as a surface wave launcher. The amount of power launched in surface waves depends upon the substrate thickness (i.e,

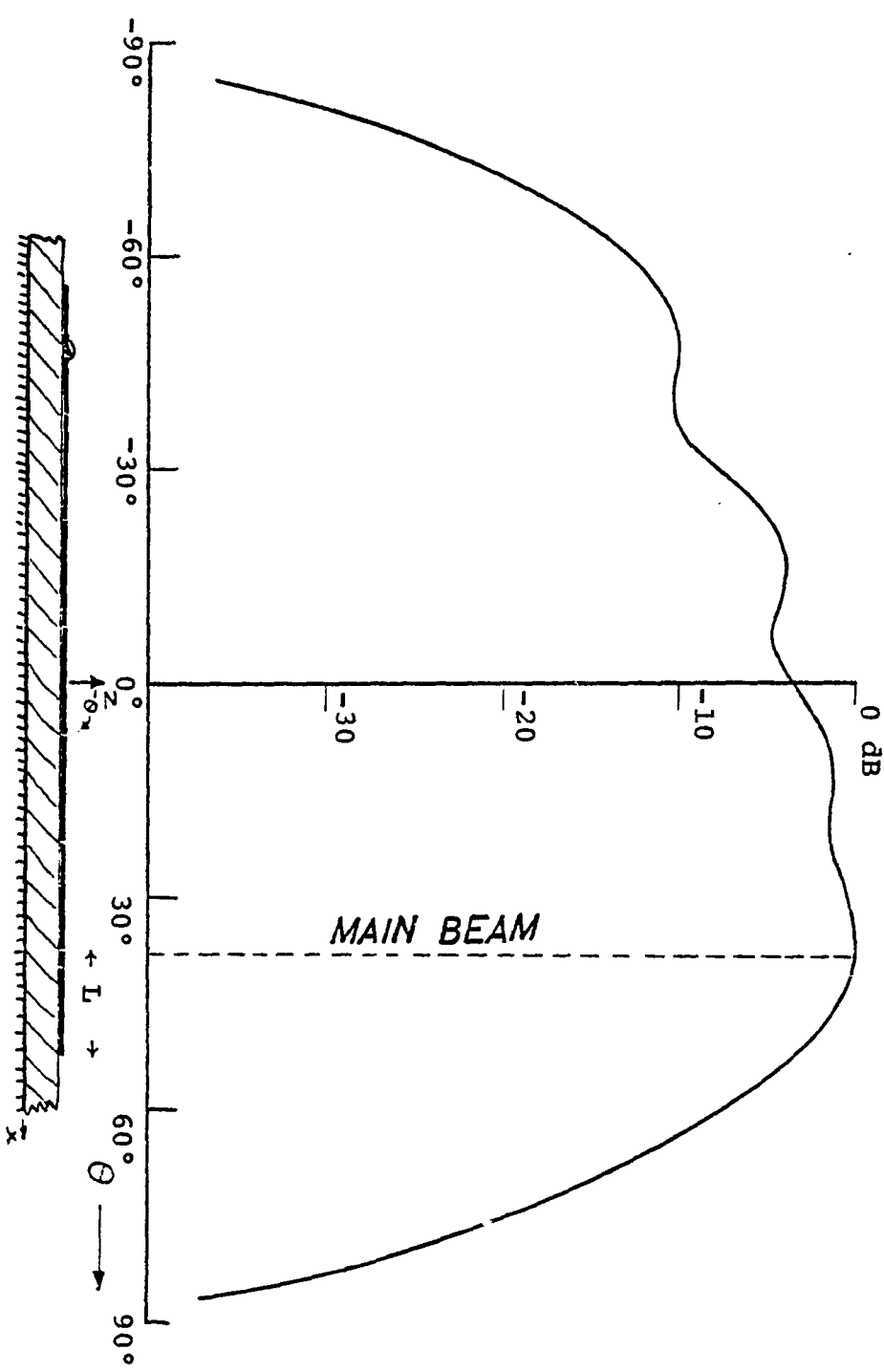


Fig. 38. Collinear Array and its Radiation Pattern, ($L=0.3\lambda_0$, $B=0.127\lambda_0$, $\epsilon_r=3.25$)

aperture size), substrate dielectric constant and operating frequency. As alluded to in Chapter I, in order to improve the radiation efficiency, bandwidth and power handling capability, substrate thickness should be increased. The increase in substrate thickness, although improves the above mentioned characteristics, yet it results in more power in the surface waves.

The radiation efficiency can further be improved by utilizing the power carried by the surface waves. In order to do that, parasitic dipoles are printed on the substrate. These elements couple power from the surface waves. The addition of the parasitics improves the radiation efficiency but radiation pattern is also modified. This has been exploited in this section to design an endfire array.

On the basis of these facts a printed parasitic array has been designed. To allow more surface wave power, the thickness and dielectric constant of the substrate have been chosen as $0.127\lambda_0$, and 3.25 respectively. All the parasitic dipoles are assumed to be equal in lengths, each being equal to $0.3\lambda_0$. In order to couple maximum power from the surface wave, all parasitics are placed end to end in collinear configuration as shown in Fig. 38. The radiation pattern with main beam at $\theta=39^\circ$, is obtained as shown in Fig. 38. It is observed that the main beam moves towards endfire by 2.5° per parasitic. The current distribution over the array is shown in Fig. 39. The phase variation

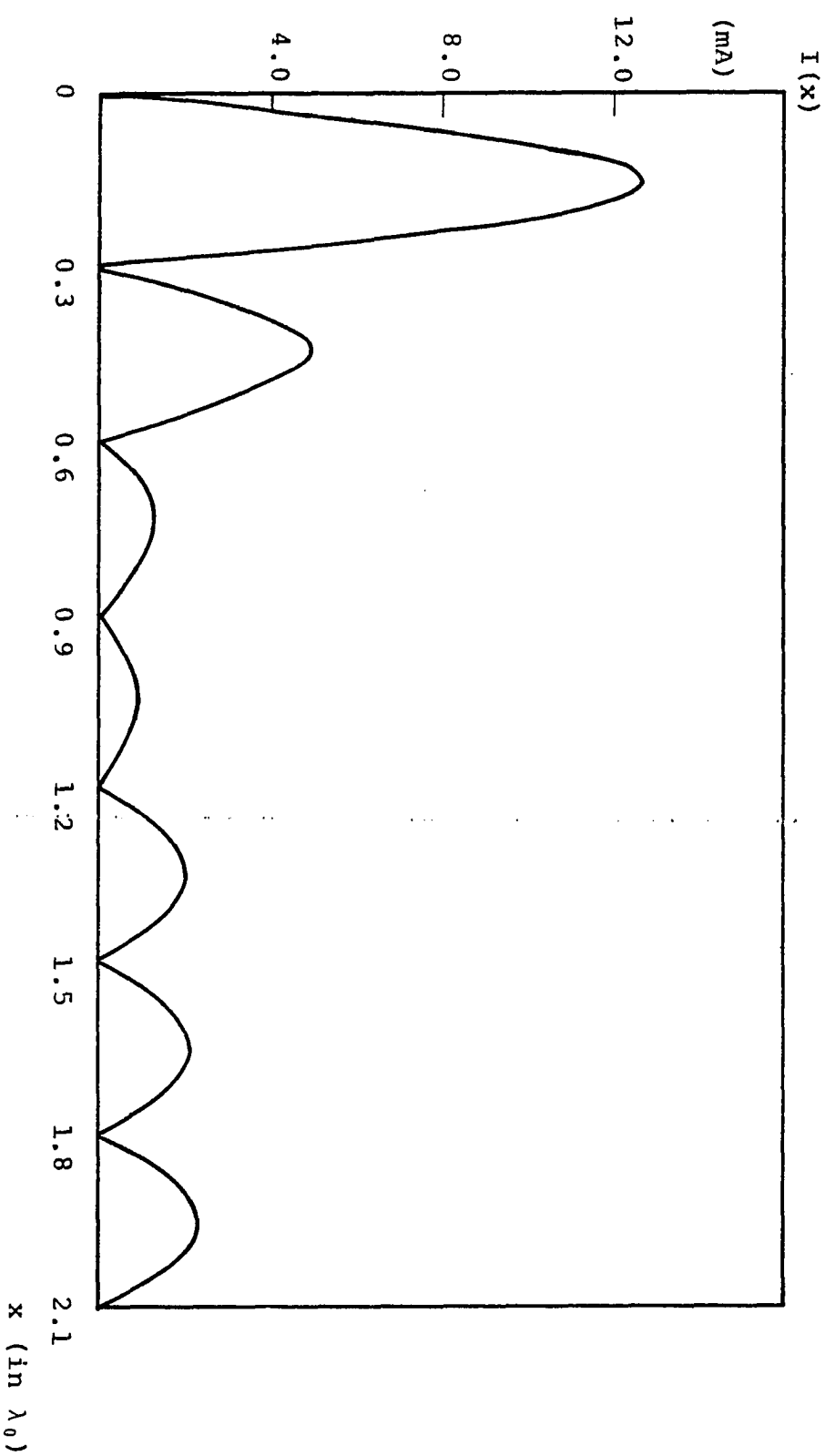


Fig. 39 Current Distribution on Collinear Array

is progressive in all parasitic dipole due to the travelling nature of the surface wave, while the driven dipole has stationary wave behavior. The dominant radiation is from the driven dipole. The superposition of progressive phase variation and stationary phase variation prevents deep nulls in the pattern. The radiation pattern has scalloped shape. This array needs more attention. Further study can be initiated along the following lines:

- 1) The lengths and spacing of the parasitic should be perturbed.
- 2) The parasitic should be printed on both sides of the driven dipole.

Another variation of the above antenna is the Franklin type of printed antenna. In this type, uniform aperture distribution is obtained by loading the printed wire or strip with the capacitors (see Jasik[25]). The addition of capacitors can be very easily incorporated in the impedance matrix to obtain the desired aperture distribution.

4.3 THE MICROSTRIP PATCH ANTENNA:

The Microstrip Patch belongs to a class of printed antennas where the current distribution is 2-dimensional in nature. This class contains a wide variety of shapes. The most popular shapes are, the rectangular patch antenna, the microstrip disc and the microstrip dipole antenna.

Due to the 2-dimensional nature of the current

distribution, a dyadic Green's function is needed. The Green's function developed in Section 2.1 can be extended to the dyadic form (see Appendix H). The integral equation for the unknown 2-dimensional vector surface current density J_s is formulated. The integral equation can be solved by the method of moments. The current distribution J_s can be modelled by the following techniques:

- 1) Wire grid modeling.
- 2) Surface patch modeling

In the first technique the surface is replaced by grid of wire dipoles. This method has been used by Richmond [26] in determining radiation and scattering characteristics of 3-dimensional objects in air. The numerical convergence of this technique is poor. The surface patch modelling has been used by Newman [27]. Two orthogonal and overlapping arrays of surface patch dipoles are placed on the surface. Thus 2-dimensional vector surface current distribution is modelled. The overlapping nature of the surface patch dipoles increases the complexity of the problem.

A new modeling technique is the Planar Triangular Patch modeling. This technique has been used by Wilton, Rao and Glission [28]. The printed patch antenna is approximated by planar triangular patches as shown in Fig. 40. Let the common side BC of an adjacent pair of triangles ABC and BCD, as shown in Fig. 39, be named as edge. With point A as reference, all points in triangle ABC are defined by

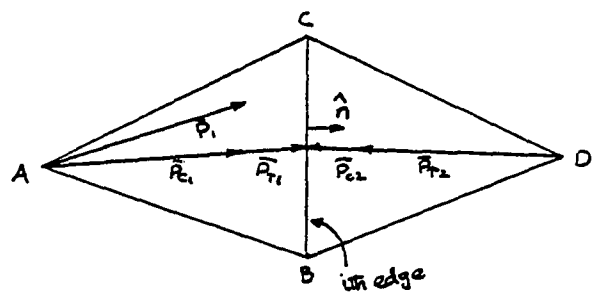


Fig. 40 Adjacent Triangles with common side BC

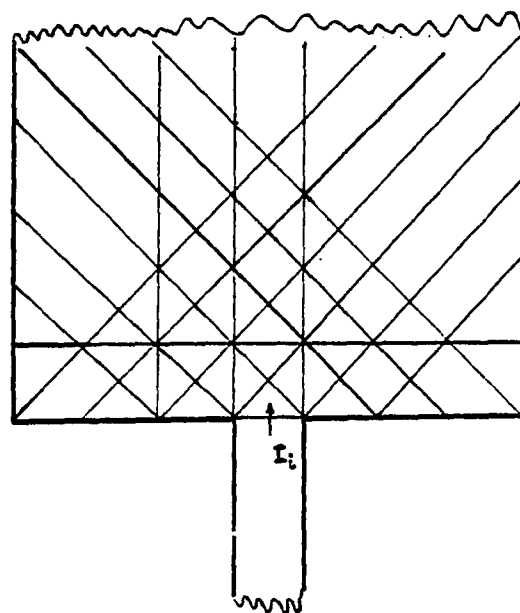


Fig. 41. Printed Patch Antenna approximated by Triangular Patches

position vector $\bar{P}_1(r)$. The position vector of the centroid of the triangle ABC and the vector joining centroid with the midpoint of side BC are defined by \bar{P}_{C_1} and \bar{P}_{T_1} , respectively. All the above definitions also apply to the corresponding vectors defined in triangle BCD. A set of basis function with respect to ith edge is defined by,

$$\bar{f}_i(r) = \begin{cases} \frac{\bar{P}_1}{\hat{n} \cdot (\bar{P}_{C_1} + \bar{P}_{T_1})}, & r \text{ in } \Delta ABC, \\ \frac{\bar{P}_2}{\hat{n} \cdot (\bar{P}_{C_2} + \bar{P}_{T_2})}, & r \text{ in } \Delta BCD \\ 0 & \text{otherwise.} \end{cases} \quad (69)$$

The surface current density \bar{J}_s is approximated with the basis functions as,

$$\bar{J}_s(r') = \sum_{i=1}^N I_i \cdot \bar{f}_i(r') \quad (70)$$

where N is the total number of edges and I_i is the component of the current normal to the ith edge. The edges defining the boundary of the printed patch are not included; as normal currents crossing all the boundary edges are zero. The integral equation of the electric type can be written in the form,

$$\bar{E}_t(r) = \int_S \bar{J}_s(r') \cdot \bar{\bar{G}}(r, r') ds' \quad (71)$$

where $\bar{\bar{G}}(r, r')$ is the dyadic Green's function derived in Appendix H. Pulse functions are used as testing functions.

They are defined as,

$$\bar{P}_i(r) = \begin{cases} \frac{\bar{P}_{\tau_1}}{|\bar{P}_{\tau_1}|}, & r \text{ in } \Delta ABC, \\ \frac{\bar{P}_{\tau_2}}{|\bar{P}_{\tau_2}|}, & r \text{ in } \Delta BCD, \\ 0, & \text{otherwise.} \end{cases} \quad (72)$$

Physically this means that the boundary condition $E_t = 0$ is forced along the line joining the centroids of the adjacent triangles. Thus the problem is reduced to the matrix form. The antenna excitation is taken into account by setting the current crossing normally the input edge (junction of the feeding microstrip line with the patch) as shown in Fig. 40, to unity. This technique offers many advantages [28]. A few are:

- 1) Triangular patches can model any arbitrary shape of printed antennas.
- 2) If the triangles are equilateral then the self term in the impedance matrix is zero, which means that the integral equation is no more singular. Due to symmetry, computational time is reduced.

4.4 FURTHER APPLICATIONS:

Following is the brief list of the problems in the area of Microwave Integrated Circuits and Printed Antennas which can be solved using this methodology:

- 1) Microstrip Power Feeding Network.
- 2) Printed Spiral Antenna.
- 3) Printed Strip Dipole Antenna.
- 4) Printed Dipole Feeding Structure.
- 5) Printed Franklin Antenna.

Chapter V

CONCLUSIONS

With regard to the theory and design of printed antennas the following conclusions now be stated:

- 1) The methodology presented in this dissertation has been successfully applied to Printed Wire Antennas, including arrays. The notable characteristics of the antennas such as input impedance, mutual impedance being known, the design of a printed array can be undertaken.
- 2) The dilemma of surface waves has been successfully answered in Chapter III. Although the analysis presented is pertinent to printed wire antennas, yet many useful results can be derived for other forms of printed antennas. The surface wave generation depends upon aperture size of the launcher. The equivalent aperture size for the printed wire is one dimensional in nature and is equal to the thickness of the substrate. On the other hand for rectangular patch (as an example), the aperture is two dimensional. Therefore one would suspect that surface waves launched by the patch will be much stronger than by the printed wire and hence the mutual coupling between patches will be stronger. The spatial dependence of the surface launching efficiency for the printed wire shows that the patch antenna will also show spatial dependence. However, this dependence will governed by the so called cavity mode excited by the patch antenna. Experimentally this has been verified by Carver [29].

- 3) The printed Yagi-Uda array shows very promising results. The printed Collinear array needs more attention, however.
- 4) The success with which printed wire antennas and wire arrays have been treated, suggests that the Printed Patch Antenna should be solved by this approach.

BIBLIOGRAPHY

1. Munson, R.E. "Conformal Microstrip Antennas and Microstrip Phased Arrays," IEEE Trans. Antennas Propagation (commun.), Vol. AP-22, pp 74-78, Jan. 1974.
2. Howell, J.E. "Microstrip Antennas," IEEE Trans. Antennas Propagat. Vol. AP-23, pp 90-93, Jan. 1975.
3. Derneryd, A.G. "A Theoretical Investigation of the Rectangular Microstrip Antenna Element," IEEE Transact. Antennas Propagat. Vol. AP-26, July 1978.
4. Lo, Y.T., Solomon, D. and Richards, W.F. "Theory and Experiment on Microstrip Antennas," IEEE Trans. Antennas Propagat. Vol. AP-27 pp 137-145, March 1979.
5. Agrawal, P.K. and Bailey, M.C. "An Analysis Technique for Microstrip Antennas," IEEE Trans. Antennas Propagat. Vol. AP-25, Nov. 1977.
6. Uzunoglu, N.K., Alexopoulos, N.G. and Fikioris, J.G. "Radiation Properties of Microstrip Antenna," accepted for publication in IEEE Trans. Antennas Propagat.
7. James, J.R and Hall, P.S "Microstrip Antennas and Arrays pt.2-New array design technique," Microwave, Optics and Acoustics, Vol. 1, No. 5 pp 175-181, Sept. 1977.
8. Derneryd, A.G. "Linearly Polarized Microstrip Antennas," IEEE Trans. Antennas Propagat. Vol. AP-24, pp 846-851 Nov. 1976.
9. Williams, J.C. "Cross Fed Printed Antennas,"

8th European Microwave Conference Proceedings,
pp 292-296.

10. Harrington R.F. "Field Computation by Moment Methods," The Macmillan Company, New York, New York.
11. Sommerfeld, A. "Partial Differential Equations in Physics," Vol.VI , Academic Press, New York.
12. Tulyathan, P. and Newman, P.K. "The Circumferential Variation of the Axial Component of Current in Closely Spaced Thin Wire Antennas," IEEE Trans. Antennas Propag. Vol. AP-27, Jan. 1979.
13. Schelkunoff, S.A. and Friis, H.T. "Antenna Theory and Practice," New York, Wiley, 1952, pp 370-401.
14. Klein, C.A. and Mittra, R. "The Effect of Different Testing Functions in the Moment Method Solution of Thin-Wire Antennas Problems," IEEE Trans. Antennas Propagat. Vol. AP-23, pp 258-261, March 1975.
15. Imbriale,W.A. and Ingerson, P.G. "On Numerical Convergence of Moment Method Solution of Moderately Thick Wire Antennas Using Sinusoidal Basis Functions," IEEE Trans. Antennas Propagat. Vol. AP-21, pp 363-366, May 1973.
16. Richmond, J.H. "Radiation and Scattering by Thin Wire Structures in a homogeneous Conducting Medium," IEEE Trans. Antennas Propagat. Vol. AP-22 Mar. 1975.
17. Rumsey, V.H. "The Reaction Concept in Electromagnetic Theory," Phys. Rev. sec. 2. Vol.94, pp 1483-1491, June 15, 1954.

18. Jones, D.S. "A Critique of the Variational Method in Scattering Problems," IRE Trans. Antennas Propagat. Vol. 4, pp 297-301, July 1956.
19. Kong, J.A., Tsang,L. and Simmons, G. "Geophysical Sub-surface Probing with Radio Frequency Interferometry," IEEE Trans. Antennas Propagat. Vol. AP-22, pp 616-620, July 1974.
20. Kantorovich, L. and Krylov, V. "Approximate Method of Higher Analysis," New York, Wiley, 1964, Ch. IV.
21. Bleistein, N. and Handelsman, R.A. "Asymptotic Expansion of Integrals," Holt, Rinehart and Winston New York. 1975, Ch. VII.
22. Felsen, L.B. and Marcuvitz, N. "Radiation and Scattering of Waves," Microwaves and Fields Series, Prentice Hall Englewood Cliffs, N.J, 1973.
23. Elliott, R.S. "An Introduction to Antenna Theory," Manuscript, to be published.

24. Theile, G.A. "Analysis of Yagi-Uda Type Antennas," IEEE Trans. Antennas Propagat. Vol. AP-17, pp 24-31, Jan.69.
25. Jasik, H. "Antenna Engineering Handbook," McGraw Hill Book Company, Inc., 1961.
26. Richmond, J.H. "A Wire Grid Model for Scattering by Conducting Bodies," IEEE Trans. Antennas Propagat. Vol. AP-14, pp 782-786 Nov. 1966.
27. Newman, E.H. and Pozar, D.M. "Electromagnetic modelling

- of Composite Wire and Surface Geometries," IEEE Trans. Antennas Propagat. Vol. AP-26 Nov. 1978.
28. Wilton, D.R., Rao, S.M. and Glisson, A.W. "Triangular Patch Modeling of Arbitrary Bodies- An Electric Field Integral Equation Approach for both Open and Closed Bodies," International Symposium Digest, AP, Vol.I June 18-22, 1979.
29. Private communication with Prof. Keith R. Carver, New Mexico State University, Las Cruces.
30. Stratton, J.A. "Electromagnetic Theory," McGraw Hill Book Company, Inc. 1941.
31. Compiled by Carmichael, R.D. and Smith, E.R. "Mathematical Tables and Formulas," Dover Publications, Inc., NY. pp 260.
32. Tai, C.T. "Dyadic Green's Function in Electromagnetic Theory," Intext Educational Publishers, San Francisco. 1971.
33. Courant, R. and Hilbert, D. "Methods of Mathematical Physics, Vol. II," Interscience Publishers N.Y. 1961.
34. Edited by Abramowitz, M. and Stegun, I.A. "Handbook of Mathematical Functions," Dover Publications, Inc., N.Y.

APPENDIX A

INTEGRAL REPRESENTATION OF Π_{xi} :

The wave incident on the substrate Π_{xi} , stimulated by horizontal Hertzian source is given by (14), as,

$$\Pi_{xi} = u \frac{e^{jk|\underline{r}-\underline{r}'|}}{|\underline{r}-\underline{r}'|}, \quad (A.1)$$

where

$$u = \frac{1}{j4\pi\epsilon_0\omega}.$$

It is desired to express (A.1), into the form of a superposition of eigen-modes. Since the boundary is open, the series is replaced by an integral. Defining a new co-ordinate system (ρ, ϕ, z) with point \underline{r}' as origin, then (A.1) becomes,

$$\Pi_{xi} = u \frac{e^{jkR}}{R}. \quad (A.2)$$

The Fourier-Bessel transform pair [30] is defined as,

$$f(\rho) = \int_0^\infty g(\lambda) J_0(\lambda\rho) \lambda d\lambda \quad (A.3)$$

and

$$g(\lambda) = \int_0^\infty f(\alpha) J_0(\alpha\lambda) \alpha d\alpha.$$

Let $f(\rho) = \frac{e^{jk\rho}}{\rho}$.

Therefore,

$$\frac{e^{jk\rho}}{\rho} = \int_0^\infty \lambda d\lambda J_0(\lambda\rho) \int_0^\infty e^{jka} J_0(a\lambda) da. \quad (A.5)$$

Replacing Bessel function $J_0(\alpha\lambda)$ by its integral representation [30], one gets,

$$\int_0^\infty e^{jka} J_0(\alpha\lambda) d\lambda = \frac{1}{2\pi} \int_{-\pi}^{\pi} d\beta \int_0^\infty d\alpha e^{j(k + \lambda \cos\beta)\alpha}, \quad (\text{A.6})$$

where k is the free space wave number.

In order to evaluate integral (A.6), it is assumed that k has a positive imaginary part so that the integrand vanishes at the upper limit. k is in fact real, but for purposes of integration the atmosphere can be assigned a very small conductivity which may be reduced to zero after the integral has been evaluated.

Therefore one gets,

$$\int_0^\infty e^{jka} J_0(\lambda\alpha) d\alpha = \frac{1}{2\pi j} \int_{-\pi}^{\pi} \frac{d\beta}{(k + \lambda \cos\beta)} . \quad (\text{A.7})$$

The right hand side of (A.7) is a standard integral, the solution of which is tabulated in mathematical tables [31]. Consequently (A.7) becomes

$$\int_0^\infty e^{jka} J_0(\lambda\alpha) d\alpha = \frac{1}{\sqrt{\lambda^2 - k^2}} . \quad (\text{A.8})$$

Substituting (A.8) in (A.5), one obtains,

$$\frac{e^{jk\rho}}{\rho} = \int_0^\infty \lambda d\lambda \cdot \frac{J_0(\rho\lambda)}{\sqrt{\lambda^2 - k^2}} . \quad (\text{A.9})$$

This represents the incident wave at all points on $z = 0$ plane excited by a source located at origion. For any

point (ρ, ϕ, z) , replacing by $R = \sqrt{\rho^2 + z^2}$ and making use of the identity,

$$J_0(\lambda R) = J_0(\lambda \rho) \cdot e^{-\sqrt{\lambda^2 - k^2} |z|}$$

one has,

$$\frac{e^{jkR}}{R} = \int_0^\infty \lambda d\lambda J_0(\rho\lambda) \frac{e^{-\mu|z|}}{\mu}, \quad \text{for all } z, \quad (\text{A.10})$$

where $\mu = \sqrt{\lambda^2 - k^2}$.

Shifting back the origin, the desired result

$$\frac{e^{jk|\bar{r}-\bar{r}'|}}{|\bar{r}-\bar{r}'|} = \int_0^\infty \lambda d\lambda J_0(\rho\lambda) \frac{e^{-\mu|z-z'|}}{\mu}, \quad \text{for all } z, \quad (\text{A.11})$$

is obtained.

APPENDIX B

SOMMERFELD'S PROOF:

Let,

$$\bar{\Pi} = \Pi_x \hat{x} \quad \text{region I} \quad (z > B) \quad (\text{B.L})$$

$$= \Pi_{xe} \hat{x} \quad \text{region II} \quad (B > z > 0) \quad (\text{B.2})$$

From (8) and (11) one obtains

$$E_x = k^2 \Pi_x + \frac{\partial^2 \Pi_x}{\partial x^2}, \quad E_y = \frac{\partial^2 \Pi_x}{\partial x \partial y} \quad z > B \quad (\text{b.3})$$

$$E_x = k_e^2 \Pi_{xe} + \frac{\partial^2 \Pi_{xe}}{\partial x^2}, \quad E_y = \frac{\partial^2 \Pi_{xe}}{\partial x \partial y} \quad B > z > 0 . \quad (\text{B.4})$$

E_y must be continuous at air dielectric interface $z=B$.

Thus,

$$\frac{\partial^2 \Pi_x}{\partial x \partial y} = \frac{\partial^2 \Pi_{xe}}{\partial x \partial y} . \quad (\text{B.5})$$

Integrating both sides with respect to y gives,

$$\frac{\partial \Pi_x}{\partial x} = \frac{\partial \Pi_{xe}}{\partial x} + C$$

and by differentiating with respect to x one gets,

$$\frac{\partial^2 \Pi_x}{\partial x^2} = \frac{\partial^2 \Pi_{xe}}{\partial x^2} . \quad (\text{B.6})$$

Matching the boundary condition for E_x component and using (B.6) it follows that,

$$k^2 \Pi_x = k_e^2 \Pi_{xe} \quad (\text{B.7})$$

(B.6) and (B.7) imply the equality of k and k_e , which is a contradiction.

Therefore

$$\vec{\Pi} = \Pi_x \hat{a}_x + \Pi_z \hat{a}_z \quad z > B \quad (B.8)$$

$$\vec{\Pi}_e = \Pi_{xe} \hat{a}_x + \Pi_{ze} \hat{a}_z \quad B > z > 0 \quad (B.9)$$

then (8), (9), (11) and (12) give

$$E_x = k^2 \Pi_x + \frac{\partial}{\partial x} (\vec{\nabla} \cdot \vec{\Pi}) \quad E_y = \frac{\partial}{\partial y} (\vec{\nabla} \cdot \vec{\Pi}) \quad z > B \quad (B.10)$$

$$E_x = k_e \Pi_{xe} + \frac{\partial}{\partial x} (\vec{\nabla} \cdot \vec{\Pi}_e) \quad E_y = \frac{\partial}{\partial y} (\vec{\nabla} \cdot \vec{\Pi}_e) \quad B > z > 0 \quad (B.11)$$

$$H_x = \frac{k^2}{j\omega\mu_0} \cdot \frac{\partial \Pi_z}{\partial y} \quad H_y = \frac{k^2}{j\omega\mu_0} \cdot \left(\frac{\partial \Pi_x}{\partial z} - \frac{\partial \Pi_z}{\partial x} \right) \quad z > B \quad (B.12)$$

$$H_y = \frac{k_e^2}{j\omega\mu_0} \cdot \frac{\partial \Pi_{ze}}{\partial y} \quad H_y = \frac{k_e^2}{j\omega\mu_0} \cdot \left(\frac{\partial \Pi_{xe}}{\partial z} - \frac{\partial \Pi_{ze}}{\partial x} \right) \quad B > z > 0 \quad (B.13)$$

From continuity of E_y at $z=B$ it follows that,

$$\vec{\nabla} \cdot \vec{\Pi} = \vec{\nabla} \cdot \vec{\Pi}_e \quad (B.14)$$

(B.14) and continuity of E_x at $z=B$ give

$$k^2 \Pi_x = k_e^2 \Pi_{xe} \quad (B.15)$$

Similarly continuity of H_x at $z=B$ requires that

$$k^2 \Pi_z = k_e^2 \Pi_{ze} \quad (B.16)$$

and continuity of H_y at $z=B$ yields the relation

$$k^2 \left[\frac{\partial \Pi_x}{\partial z} - \frac{\partial \Pi_z}{\partial x} \right] = k_e^2 \left[\frac{\partial \Pi_{xe}}{\partial z} - \frac{\partial \Pi_{ze}}{\partial x} \right] \quad (B.17)$$

Differentiating (B.16) with respect to x and substituting in (B.17) yields,

$$k^2 \frac{\partial \Pi_x}{\partial z} = k_e^2 \frac{\partial \Pi_{xe}}{\partial z} \quad (B.18)$$

Since $\frac{k_e^2}{k^2} = n^2$, therefore (B.15) and (B.16) can be written as,

$$\Pi_x = n^2 \Pi_{xe} \quad \text{and} \quad \frac{\partial \Pi_x}{\partial z} = n^2 \frac{\partial \Pi_{xe}}{\partial z} \quad (B.19)$$

(conditions for Π_x and Π_{xe}).

Similarly for Π_z and Π_{ze} two conditions are obtained from (B.14) and (B.16) as,

$$\Pi_z = n^2 \Pi_{ze} \quad \text{and} \quad \frac{\partial \Pi_z}{\partial z} - \frac{\partial \Pi_{ze}}{\partial z} = \frac{\partial \Pi_{xe}}{\partial x} - \frac{\partial \Pi_x}{\partial x}. \quad (B.20)$$

Next, it is desired to turn to the fabrication of Π_z component of Hertz vector Π . From (15) it is obvious that Π_x is composed of solutions of the form $J_0(\rho\lambda) \cdot e^{-\mu|z|}$.

Making use of (B.20) and (B.19) one obtains,

$$\frac{\partial \Pi_z}{\partial z} = -\frac{\partial \Pi_x}{\partial x} \sim -J'_0(\rho\lambda) \cdot \frac{x}{\rho} \cdot e^{-\mu|z|}$$

Integrating with respect to z one gets,

$$\Pi_z \sim J_1(\rho\lambda) \cdot \cos\phi \cdot e^{-\mu|z|},$$

where $\cos\phi = \frac{x}{\rho}$.

Therefore, Π_z component is constructed from the solutions containing Bessel function of order 1, while Π_x involves

Bessel function of order zero.

APPENDIX C

REDUCTION OF POCKLINGTON'S EQUATION (33) USING
SINUSOIDAL FUNCTIONS TO THE FORM (38):

Pocklington's equation (33) can be written as,

$$E_x = \int_L I(x') \left[k^2 \Pi_x + \frac{\partial^2 \Pi_x}{\partial x^2} + \frac{\partial^2 \Pi_z}{\partial x \partial z} \right] dx' . \quad (C.1)$$

$I(x')$ is approximated by a finite term series of sinusoidal expansion functions, i.e.,

$$I(x') = \sum_{i=2}^N I_i P_i \frac{\sin k(x' - x_{i-1})}{\sin kd} + P_{i+1} \frac{\sin k(x_{i+1} - x')}{\sin kd} \quad (C.2)$$

where

$$\begin{aligned} P_i(x') &= 1 & x_{i-1} < x' < x_i \\ &= 0 & \text{otherwise.} \end{aligned}$$

Substituting (C.2) in (C.1), one gets,

$$\begin{aligned} E_x &= \sum_{i=2}^N \frac{I_i}{\sin kd} \left[\int_{x_{i-1}}^{x_i} \sin k(x' - x_{i-1}) \cdot \left[k^2 \Pi_x + \frac{\partial^2 \Pi_x}{\partial x^2} + \frac{\partial^2 \Pi_z}{\partial x \partial z} \right] dx' + \right. \\ &\quad \left. \int_{x_i}^{x_{i+1}} \sin k(x_{i+1} - x') \cdot \left[k^2 \Pi_x + \frac{\partial^2 \Pi_x}{\partial x^2} + \frac{\partial^2 \Pi_z}{\partial x \partial z} \right] dx' \right] . \quad (C.3) \end{aligned}$$

Rewriting the first integral under the summation sign as:

$$I_1 = k^2 \int_{x_{i-1}}^{x_i} \sin k(x' - x_{i-1}) \Pi_x dx' + \int_{x_{i-1}}^{x_i} \sin k(x' - x_{i-1}) \frac{\partial^2 \Pi_x}{\partial x^2} dx' +$$

$$\int_{x_{i-1}}^{x_i} \sin k(x' - x_{i-1}) \frac{\partial^2 \Pi_z}{\partial x \partial z} dz' . \quad (C.4)$$

By using the identity $\frac{\partial}{\partial x'} = -\frac{\partial}{\partial x}$, the second integral in (C.4) can be integrated by parts as follows,

$$\int_{x_{i-1}}^{x_i} \sin k(x' - x_{i-1}) \frac{\partial^2 \Pi_x}{\partial x^2} dx' = -\frac{\partial \Pi_x}{\partial x} \cdot \sin k(x' - x_{i-1}) \Big|_{x_{i-1}}^{x_i} +$$

$$k \int_{x_{i-1}}^{x_i} \cos k(x' - x_{i-1}) \cdot \frac{\partial \Pi_x}{\partial x} dx' .$$

Integrating by parts again and simplifying one obtains;

$$\int_{x_{i-1}}^{x_i} \sin k(x' - x_{i-1}) \frac{\partial^2 \Pi_x}{\partial x^2} dx' = \sin kd \cdot \frac{\partial \Pi_x}{\partial x} \Big|_{x_i} - k \cos kd \cdot \Pi_x \Big|_{x_i} +$$

$$k \cdot \Pi_x \Big|_{x_{i-1}} - k^2 \int_{x_{i-1}}^{x_i} \sin k(x' - x_{i-1}) \cdot \Pi_x dx' . \quad (C.5)$$

Making use of the above mentioned identity, the third integral can be integrated by parts as follows,

$$\int_{x_{i-1}}^{x_i} \sin k(x' - x_{i-1}) \cdot \frac{\partial^2 \Pi_z}{\partial x \partial z} dz' = - \sin k(x' - x_{i-1}) \cdot \frac{\partial \Pi_z}{\partial z} \Big|_{x_i} +$$

$$k \cdot \cos k(x' - x_{i-1}) \cdot \Pi \left[\int_{x_{i-1}}^{x_i} \sin k(x' - x_{i-1}) \cdot \Pi \cdot dx' \right] + k^2 \int_{x_{i-1}}^{x_i} \sin k(x' - x_{i-1}) \cdot \Pi \cdot dx' ,$$

where

$$\Pi = \frac{\partial}{\partial z} \int \Pi_z \cdot dx' . \quad (C.6)$$

Further simplification yields,

$$\begin{aligned} & \int_{x_{i-1}}^{x_i} \sin k(x' - x_{i-1}) \cdot \frac{\partial^2 \Pi_z}{\partial x \partial z} dx' = - \sin kd \cdot \frac{\partial \Pi_z}{\partial z} \Big|_{x_i} + k \cdot \cos kd \cdot \Pi \Big|_{x_i} - \\ & k \cdot \Pi \Big|_{x_{i-1}} + k^2 \int_{x_{i-1}}^{x_i} \sin k(x' - x_{i-1}) \cdot \Pi \cdot dx' . \end{aligned} \quad (C.7)$$

By substituting now (C.5) and (C.7) in (C.4) one gets,

$$\begin{aligned} I_1 &= - \sin kd \cdot \frac{\partial \Pi_x}{\partial x} \Big|_{x_i} - k \cdot \cos kd \cdot \Pi_x \Big|_{x_i} + k \cdot \Pi_x \Big|_{x_{i-1}} - \frac{\partial \Pi_z}{\partial z} \Big|_{x_i} + \\ & k \cdot \cos kd \cdot \Pi \Big|_{x_i} + k^2 \int_{x_{i-1}}^{x_i} \sin k(x' - x_{i-1}) \cdot \Pi \cdot dx' . \end{aligned} \quad (C.8)$$

Similary following the steps, it can be proved that the second integral I_2 in (C.3) simplifies to,

$$\begin{aligned} I_2 &= \sin kd \cdot \frac{\partial \Pi_x}{\partial x} \Big|_{x_i} - k \cdot \cos kd \cdot \Pi_x \Big|_{x_i} + k \cdot \Pi_x \Big|_{x_{i+1}} + \frac{\partial \Pi_z}{\partial z} \Big|_{x_i} + \\ & k \cdot \cos kd \cdot \Pi \Big|_{x_i} + k^2 \int_{x_i}^{x_{i+1}} \sin k(x_{i+1} - x') \cdot \Pi \cdot dx' . \end{aligned} \quad (C.9)$$

Substituting (C.8) and (C.9) back in (C.3) one obtains,

$$\begin{aligned}
 E_x(x, y, z) = & \frac{k}{\sin kd} \sum_{i=2}^N I_i \left[\Pi_x \Big|_{x_{i+1}} + \Pi_x \Big|_{x_{i-1}} - 2 \cos kd \cdot \Pi_x \Big|_{x_i} + \right. \\
 & 2 \cos kd \cdot \Pi \Big|_{x_i} - \Pi \Big|_{x_{i+1}} - \Pi \Big|_{x_{i-1}} + k \left[\int_{x_{i-1}}^{x_i} \sin k(x' - x_{i-1}) \cdot \Pi \cdot dx' + \right. \\
 & \left. \left. \int_{x_i}^{x_{i+1}} \sin k(x_{i+1} - x') \cdot \Pi \cdot dx' \right] \right], \quad (C.10)
 \end{aligned}$$

which is the desired result.

(C.6) can be rewritten as,

$$\Pi = \frac{\partial}{\partial z} \int \Pi_z \, dx' = \int \frac{\partial \Pi}{\partial z} \, dx', \quad (C.11)$$

where

$$\Pi_z = -2 \cdot (n^2 - 1) \int_0^\infty J_0(\rho\lambda) \cdot \cos\phi \cdot e^{-\mu(z-B)} \frac{\lambda^2 d\lambda}{D_e(\lambda) \cdot D_m(\lambda)}. \quad (C.12)$$

Differentiating (C.12) with respect to z and by substituting in (C.11) one obtains,

$$\Pi = 2 \cdot (n^2 - 1) \int_0^\infty J_1(\rho\lambda) \cdot \cos\phi \cdot e^{-\mu(z-B)} \frac{\lambda^2 \mu d\lambda}{D_e(\lambda) \cdot D_m(\lambda)}. \quad (C.13)$$

Exchanging the order of integration (it can be easily proved that this is proper) and by substituting $\cos\phi = \frac{x-x'}{\rho}$ in (C.13) one gets,

$$\Pi = -2 \cdot (n^2 - 1) \int_0^\infty d\lambda \cdot \frac{\lambda \mu \cdot e^{-\mu(z-B)}}{D_e(\lambda) \cdot D_m(\lambda)} \cdot dx' J'_0(\rho\lambda) \cdot \frac{x-x'}{\rho} \cdot \lambda. \quad (C.14)$$

The integrand is a complete differential of $J_0(\rho\lambda)$,

substituting, (C.14) simplifies to,

$$\Pi = -2 \cdot (n^2 - 1) \int_0^\infty J_0(\rho\lambda) \cdot \frac{\mu\lambda e^{-\mu(z-B)}}{D_e(\lambda) \cdot D_m(\lambda)} \cdot d\lambda. \quad (C.15)$$

APPENDIX D

PRINCIPAL VALUE INTEGRATION:

The integral

$$I = \int_{k}^{nk} \frac{f(\lambda)}{(\lambda - \lambda_0)} d\lambda \quad (D.1)$$

which is to be evaluated along the real λ -axis, does not have a Riemann value.

By deleting the segment $\lambda_2 - \lambda_1$, from the interval (k, nk) , where λ_2 and λ_1 are selected so that $|\lambda_2 - \lambda_0| = |\lambda_0 - \lambda_1| = \varepsilon$ ($\varepsilon \ll 1$), the principal value of integral (D.1) can be written as,

$$P.V \int_{k}^{nk} \frac{f(\lambda)}{(\lambda - \lambda_0)} d\lambda = \lim_{\varepsilon \rightarrow 0} \int_{k}^{\lambda_1} \frac{f(\lambda)}{(\lambda - \lambda_0)} d\lambda + \int_{\lambda_2}^{nk} \frac{f(\lambda)}{(\lambda - \lambda_0)} d\lambda. \quad (D.2)$$

Let C_ε denote the segment $\lambda_2 - \lambda_1$. Since $f(\lambda)$ satisfies Holder's condition [34], at $\lambda = \lambda_0$ therefore,

$$\int_{L-C_\varepsilon}^{nk} \frac{f(\lambda)}{(\lambda - \lambda_0)} d\lambda = \int_{L-C_\varepsilon}^{\lambda_1} \frac{f(\lambda) - f(\lambda_0)}{(\lambda - \lambda_0)} d\lambda + \int_{L-C_\varepsilon}^{\lambda_2} \frac{f(\lambda_0)}{(\lambda - \lambda_0)} d\lambda. \quad (D.3)$$

Consider now the integral

$$\lim_{\varepsilon \rightarrow 0} \int_{L-C_\varepsilon}^{\lambda_1} \frac{f(\lambda) - f(\lambda_0)}{(\lambda - \lambda_0)} d\lambda = \int_L^{\lambda_1} \frac{f(\lambda) - f(\lambda_0)}{(\lambda - \lambda_0)} d\lambda. \quad (D.4)$$

The above integral has a Riemann value, and hence can be evaluated numerically. Next,

$$\begin{aligned} \lim_{\varepsilon \rightarrow 0} \int_{L-C_\varepsilon}^{\lambda_1} \frac{f(\lambda_0)}{(\lambda - \lambda_0)} d\lambda &= \lim_{\varepsilon \rightarrow 0} f(\lambda_0) \cdot \left[\int_k^{\lambda_1} \frac{d\lambda}{(\lambda - \lambda_0)} + \int_{\lambda_2}^{nk} \frac{d\lambda}{(\lambda - \lambda_0)} \right] \\ &= \lim_{\varepsilon \rightarrow 0} f(\lambda_0) \left[\ln \left[\frac{nk - \lambda_0}{k - \lambda_0} \right] + \ln \left[\frac{\lambda_1 - \lambda_0}{\lambda_2 - \lambda_0} \right] \right]. \end{aligned} \quad (D.5)$$

In the evaluation of these logarithmic terms care must be taken as $\ln(z)$ is a multi-valued function. To insure single-valuedness of the function branch cut is drawn through λ_0 as shown in Fig. 42.

Now,

$$z - \lambda_0 = r e^{j\theta} \quad \theta \in (0, 2\pi)$$

$$\ln(z - \lambda_0) = \ln(r) + j\theta$$

$$\begin{aligned} \ln(\lambda_1 - \lambda_0) - \ln(\lambda_2 - \lambda_0) &= \ln(r) + j\theta_1 - \ln(r) - j\theta_2 \\ &= j(\theta_1 - \theta_2) \end{aligned}$$

Therefore,

$$\lim_{\epsilon \rightarrow 0} \frac{\ln \left[\frac{\lambda_1 - \lambda_0}{\lambda_2 - \lambda_0} \right]}{\epsilon} = -j\pi. \quad (\text{D.6})$$

Similarly,

$$\ln \left[\frac{nk - \lambda_0}{k - \lambda_0} \right] = \ln \left| \frac{nk - \lambda_0}{k - \lambda_0} \right| + j\pi. \quad (\text{D.7})$$

Substituting (D.6) and (D.7) in (D.5) and then combining with (D.2), one has

$$\text{P.V.} \int_k^{nk} \frac{f(\lambda)}{\lambda - \lambda_0} d\lambda = \int_k^{nk} \frac{f(\lambda) - f(\lambda_0)}{\lambda - \lambda_0} d\lambda + f(\lambda_0) \cdot \ln \left| \frac{nk - \lambda_0}{k - \lambda_0} \right|. \quad (\text{D.8})$$

Integrating along the path of integration as shown in the Fig. 42 one gets,

$$I = \lim_{\epsilon \rightarrow 0} \left[\int_{-k}^{\lambda_1} \frac{f(\lambda)}{\lambda - \lambda_0} d\lambda + \int_{\lambda_2}^{nk} \frac{f(\lambda)}{\lambda - \lambda_0} d\lambda + \int_C \frac{f(\lambda)}{\lambda - \lambda_0} d\lambda \right]. \quad (\text{D.9})$$

Making use of (D.2), (D.9) reduces to,

$$I = \text{P.V.} + \lim_{\epsilon \rightarrow 0} \int_C \frac{f(\lambda)}{\lambda - \lambda_0} d\lambda. \quad (\text{D.10})$$

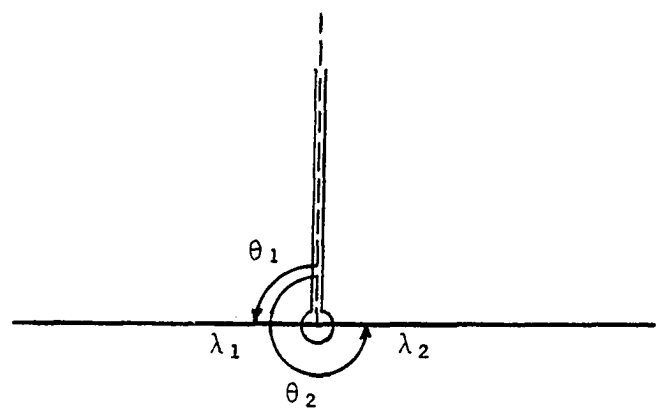
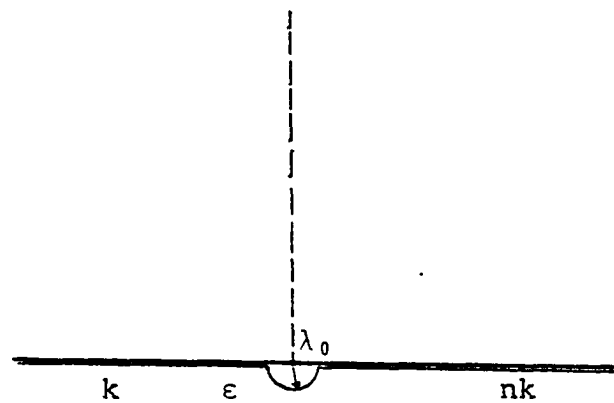


Fig. 42. Path of Integration for Integral (D.1)

From Fig. 42 it follows that

$$\lambda = \lambda_0 + \varepsilon e^{j\theta} . \quad (D.11)$$

Differentiating (D.11) and substituting in (D.10) one obtains,

$$I = P.V + j \left[\lim_{\varepsilon \rightarrow 0} \int_{-\pi}^0 f(\lambda_0 + \varepsilon e^{j\theta}) d\theta \right] . \quad (D.12)$$

By rewriting and using limiting process as follows,

$$I = P.V + j \left[\lim_{\varepsilon \rightarrow 0} \int_{-\pi}^0 f(\lambda_0) + \lim_{\varepsilon \rightarrow 0} \int_{-\pi}^0 [f(\lambda) - f(\lambda_0)] d\theta \right]$$

$$\lim_{\substack{\varepsilon \rightarrow 0 \\ \lambda \rightarrow \lambda_0}} \int_{-\pi}^0 [f(\lambda) - f(\lambda_0)] d\theta < \lim_{\substack{\varepsilon \rightarrow 0 \\ \lambda \rightarrow \lambda_0}} |f(\lambda) - f(\lambda_0)| \cdot \pi = 0$$

one has,

$$I = P.V + j \cdot f(\lambda_0) \cdot \pi . \quad (D.13)$$

Replacing P.V by (D.8) one is led to desired result,

i.e., $I = \int_k^{nk} \frac{f(\lambda) - f(\lambda_0)}{\lambda - \lambda_0} d\lambda + f(\lambda_0) \left[\ln \left| \frac{nk - \lambda_0}{k - \lambda_0} \right| + j\pi \right] .$

APPENDIX E

TWO SURFACE WAVE POLES

Let λ_{pm} and λ_{pe} be the two surface wave poles (T.M and T.E) such that

$$k < \lambda_{pe} < \lambda_{pm} < nk.$$

Then integral (40) over the interval (k, nk) can be represented by,

$$I = \int_k^{nk} \frac{f(\lambda)}{(\lambda - \lambda_{pm})(\lambda - \lambda_{pe})} d\lambda \quad (E.1)$$

where,

$$f(\lambda) = \frac{J_0(\lambda\rho)\mu\lambda(\lambda - \lambda_{pe})(\lambda - \lambda_{pm})}{(\mu + \mu_e \operatorname{Coth} \mu_e B)(\mu n^2 + \mu_e \operatorname{Tanh} \mu_e B)} \quad (E.2)$$

(E.1) can be written as,

$$I = \frac{1}{(\lambda_{pm} - \lambda_{pe})} \left[\int_k^{nk} \frac{f(\lambda)}{(\lambda - \lambda_{pm})} d\lambda - \int_k^{nk} \frac{f(\lambda)}{(\lambda - \lambda_{pe})} d\lambda \right] \quad (E.3)$$

As illustrated in Appendix D one can write each integral in the above equation as,

$$\int_k^{nk} \frac{(f(\lambda) - f(\lambda_{pm}))}{(\lambda - \lambda_{pm})} d\lambda = \int_k^{nk} \frac{(f(\lambda) - f(\lambda_{pm}))}{(\lambda - \lambda_{pm})} d\lambda + f(\lambda_{pm}) \left[\ln \frac{nk - \lambda_{pm}}{\lambda_{pm} - k} + j\pi \right] \quad (E.4)$$

and

$$\int_k^{nk} \frac{(f(\lambda) - f(\lambda_{pe}))}{(\lambda - \lambda_{pe})} d\lambda = \int_k^{nk} \frac{(f(\lambda) - f(\lambda_{pe}))}{(\lambda - \lambda_{pe})} d\lambda + f(\lambda_{pe}) \left[\ln \frac{nk - \lambda_{pe}}{\lambda_{pe} - k} + j\pi \right] \quad (E.5)$$

where

$$f(\lambda_{pm}) = \lim_{\lambda \rightarrow \lambda_{pm}} f(\lambda) \quad (E.6)$$

and

$$f(\lambda_{pe}) = \lim_{\lambda \rightarrow \lambda_{pe}} f(\lambda) . \quad (E.7)$$

Using L'Hospital's rule one obtains,

$$f(\lambda_{pm}) = \frac{J_0(\lambda_{pm}) \mu_m^2 \mu_{em} (\lambda_{pm} - \lambda_{pe})}{[\mu_m + \mu_{em} \coth \mu_{em} B] \cdot (n^2 \mu_{em} + \mu_m \tanh \mu_{em} B + B \mu_{em} \mu_m)} \frac{(1 - \tanh^2 \mu_{em} B)}{(1 - \coth^2 \mu_{ee} B)} \quad (E.8)$$

and

$$f(\lambda_{pe}) = \frac{J_0(\lambda_{pe}) \mu_e^2 \mu_{ee} (\lambda_{pe} - \lambda_{pm})}{[\mu_e n^2 + \mu_{ee} \tanh \mu_{ee} B] \cdot (\mu_{ee} + \mu_e \coth \mu_{ee} B + B \mu_{ee} \mu_e)} \frac{(1 - \coth^2 \mu_{ee} B)}{(1 - \coth^2 \mu_{ee} B)} \quad (E.9)$$

$$\text{where } \mu_m = \sqrt{\lambda_{pm}^2 - k^2}, \quad \mu_{em} = \sqrt{\lambda_{pm}^2 - n^2 k^2}$$

$$\mu_e = \sqrt{\lambda_{pe}^2 - k^2} \quad \text{and} \quad \mu_{ee} = \sqrt{\lambda_{pe}^2 - n^2 k^2} .$$

Substituting (E.4) and (E.5) in (E.3) one obtains,

$$I = \frac{1}{(\lambda_{pm} - \lambda_{pe})} \left[\int_{\lambda_{pm}}^{\lambda_{pe}} \frac{f(\lambda) - f(\lambda_{pm})}{(\lambda - \lambda_{pm})} d\lambda - \int_{\lambda_{pe}}^{\lambda_{pm}} \frac{f(\lambda) - f(\lambda_{pe})}{(\lambda - \lambda_{pe})} d\lambda + f(\lambda_{pm}) \cdot \ln \frac{n k - \lambda_{pm}}{\lambda_{pm} - k} + f(\lambda_{pe}) \cdot \ln \frac{n k - \lambda_{pe}}{\lambda_{pe} - k} + \pi j \left[f(\lambda_{pm}) + f(\lambda_{pe}) \right] \right], \quad (E.10)$$

where $f(\lambda)$, $f(\lambda_{pm})$ and $f(\lambda_{pe})$ are defined by (E.2), (E.8) and (E.9), respectively.

APPENDIX F

TAIL CONTRIBUTION OF INTEGRALS (39) AND (40):

Integral (39) can be written in the form,

$$\Pi_x = 2 \cdot u \int_0^{\infty} J_0(\rho\lambda) \left(\frac{\lambda d\lambda}{\mu + \mu_e \coth \mu_e B} \right) \quad (F.1)$$

Breaking $(0, \infty)$ interval as,

$$= 2 \cdot u \int_0^A J_0(\rho\lambda) \left(\frac{\lambda d\lambda}{\mu + \mu_e \coth \mu_e B} \right) + 2 \cdot u \int_A^{\infty} J_0(\rho\lambda) \left(\frac{d\lambda}{\mu + \mu_e} \right) \quad (F.2)$$

where A is chosen so that $\left| \coth \mu_e B \right| \approx 1$ for $\lambda > A$.

Integration along the $(0, A)$ interval is performed numerically, while tail contribution i.e., integration from $A \rightarrow \infty$, can be computed analytically, as follows.

Since $\lambda > k$ and nk for $\lambda > A$, the radicals μ and μ_e can be expanded in a Binomial series as,

$$\mu = \sqrt{\lambda^2 - k^2} = \lambda \left[1 - \frac{k^2}{2\lambda^2} - \frac{k^4}{8\lambda^4} - \frac{k^6}{16\lambda^6} - \frac{k^8}{128\lambda^8} \dots \dots \right], \quad (F.3)$$

$$\mu_e = \sqrt{\lambda^2 - k^2 n^2} = \lambda \left[1 - \frac{k^2}{2\lambda^2} - \frac{k^4}{8\lambda^4} - \frac{k^6}{16\lambda^6} - \frac{k^8}{128\lambda^8} \dots \dots \right]. \quad (F.4)$$

Summing (F.3) and (F.4) one gets,

$$\mu + \mu_e \approx \lambda \left[1 - L \frac{k^2}{\lambda^2} - M \frac{k^4}{\lambda^4} - N \frac{k^6}{\lambda^6} - P \frac{k^8}{\lambda^8} \dots \dots \right] \quad (F.5)$$

where L, M, N and P are constants which are defined as,

$$L = \frac{n^2+1}{4} , M = \frac{n^4+1}{16} , N = \frac{n^6+1}{32} \text{ and } P = \frac{5(n^8+1)}{128}.$$

(F.5)

Dividing 2λ by (F.5) yields,

$$\frac{2\lambda}{\mu + \mu_e} = 1 + \frac{XL}{\lambda^2} + \frac{XT}{\lambda^4} + \frac{XC}{\lambda^6} + \frac{XB}{\lambda^8} + \dots \quad (\text{F.7})$$

where constants XL , XT , XC , and XB are defined as,

$$XL = Lk^2$$

$$XT = (L^2 + M)k^4$$

$$XC = (L^3 + 2LM + N)k^6$$

$$XB = (L(L^3 + 2LM + N) + M(L^2 + M) + LN + P)k^8$$

Substituting (F.6) in the second integral in (F.2), one writes tail contribution as,

$$\text{TAILX} = u \int_A^\infty J_0(\lambda\rho) \left[1 + \frac{XL}{\lambda^2} + \frac{XT}{\lambda^4} + \frac{XC}{\lambda^6} + \frac{XB}{\lambda^8} + \dots \right] d\lambda \quad (\text{F.9})$$

series is analytic, hence integrating term by term as follows,

$$\begin{aligned} \int_A^\infty J_0(\lambda\rho) d\lambda &= \int_0^\infty J_0(\lambda\rho) d\lambda - \int_0^A J_0(\lambda\rho) d\lambda \\ &= 1/\rho - I_0; \end{aligned} \quad (\text{F.10})$$

$$\int_A^\infty \frac{J_0(\lambda\rho)}{\lambda^2} d\lambda = \rho \left[J_0(D)/D - J_1(D) - 1 \right] + I_0 \rho^2, \quad (\text{F.11})$$

$$\int_A^\infty \frac{J_0(\lambda\rho)}{\lambda^4} d\lambda = \frac{\rho^3}{3} \left[J_0(D)/D^3 - \left[J_1(D) \left[\frac{1}{D^2} - \frac{2}{3} \right] + J_2(D)/D - (J_3(D) + 1)/3 \right] \right] - I_0\rho^4/9 , \quad (F.12)$$

$$\int_A^\infty \frac{J_0(\lambda\rho)}{\lambda^6} d\lambda = \frac{\rho^5}{5} \left[J_0(D)/D^5 - \left[J_1(D)/D^4 - J_2(D)/D^3 - J_3(D)/D^2 - J_2(D)/3D + \left[J_5(D) + 2(J_3(D) + J_1(D)) + 1 \right]/15 \right] \right. \\ \left. /3 \right] + I_0\rho^6/225 \quad (F.13)$$

$$\int_A^\infty \frac{J_0(\lambda\rho)}{\lambda^8} d\lambda = \frac{\rho^7}{7} \left[J_0(D)/D^7 - \left[J_1(D)/D^6 - J_2(D)/D^5 - J_3(D)/D^4 - J_4(D)/3D^2 - J_5(D)/15D + \left[1 + 2(J_1(D) + J_3(D) + J_5(D)) + J_7(D) \right]/105 \right] \right] /3 /5 - I_0\rho^8/11025 , \quad (F.14)$$

where $D = A\rho$ and $I_0 = \int_0^A J_0(\lambda\rho) d\lambda$.

The integral I_0 can be evaluated numerically.

Next, substituting (F.10) through (F.14) in (F.9) one obtains the tail contribution of integral (F.1).

Similarly by breaking the interval $(0, \infty)$ of integral (40), one can write (40) as,

$$\Pi = 2(n^2 - 1) u \left[\int_0^A J_0(\lambda \rho) \frac{\mu \lambda d\lambda}{(\mu + \mu_e \coth \mu_e B)(\mu n^2 + \mu_e \tanh \mu_e B)} + \int_A^\infty J_0(\lambda \rho) \frac{\mu \lambda d\lambda}{(\mu^2 n^2 + (n^2 + 1) \mu \mu_e + \lambda^2 - n^2 k^2)} \right] \quad (F.15)$$

By using Binomial expansions for μ and μ_e , and proceeding, one obtains the tail contribution of (F.15) as,

$$\text{TAILZ} = \frac{(n^2 - 1)}{(n^2 + 1)} u \int_A^\infty J_0(\lambda \rho) \left[1 + \frac{ZL}{\lambda^2} + \frac{ZT}{\lambda^4} + \frac{ZC}{\lambda^6} + \frac{ZB}{\lambda^8} + \dots \dots \right] d\lambda \quad (F.16)$$

where constants ZL , ZT , ZC , and ZB are defined by,

$$ZL = (R - 0.5)k^2$$

$$ZT = (R(R - 0.5) + S - 0.125)k^4$$

$$ZC = (S(R - 0.5) + T - 0.0625 + R^2(R - 0.125) + R(S - 0.125))k^6$$

$$ZB = (T(R - 0.125) + U - 5/128 + 2RS(R - 0.5) + S^2 - S/8 + RT - R/16 + R^3(R - 0.5) + R^2(S - 0.125))k^8$$

(F.17)

with

$$R = \frac{n^4 + 6n^2 + 1}{4(n^2 + 1)}, \quad S = \frac{1 + n^4 + n^2}{16}, \quad T = \frac{n^6 - n^4 - n^2 + 1}{32}$$

and $U = \frac{5(n^8 + 1)}{256} - \frac{n^4}{128} - \frac{n^6}{64} - \frac{n^2}{64}$. (F.18)

APPENDIX G

FAR ZONE FIELDS

The Green's function for region I can be written as,

$$\Pi_x = u \int_0^\infty J_0(\rho\lambda) \cdot e^{-\mu(z-B)} \frac{\lambda d\lambda}{D_e(\lambda)} \quad (G.1)$$

$$\Pi_z = 2 \cdot (1-n^2) u \int_0^\infty J_0(\rho\lambda) \cdot e^{-\mu(z-B)} \frac{\cos\phi \cdot \lambda^2 d\lambda}{D_e(\lambda) \cdot D_m(\lambda)} \quad (G.2)$$

where $\mu = \sqrt{\lambda^2 - k^2}$.

The path of integration is shown in Fig. 4. By analytical continuation into the complex λ -plane one obtains,

$$\Pi_x = u \int_{-\infty}^\infty H_0(\rho\lambda) \cdot e^{-\mu(z-B)} \frac{\lambda d\lambda}{D_e(\lambda)} \quad (G.3)$$

and

$$\Pi_z = u(1-n^2) \int_{-\infty}^\infty H_1(\rho\lambda) \cdot e^{-\mu(z-B)} \frac{\cos\phi \cdot \lambda^2 d\lambda}{D_e(\lambda) \cdot D_m(\lambda)} \quad (G.4)$$

The cylindrical to spherical coordinate transformations, with source point (x', y', B) as origin, are given by,

$$\rho = R \sin\theta \quad \text{and} \quad z-B = R \cos\theta \quad (G.5)$$

By using (G.5), (G.3) and (G.4) reduce to,

$$\Pi_x = u \int_{-\infty}^\infty H_0(\lambda R \sin\theta) \cdot e^{-\mu R \cos\theta} \frac{\lambda d\lambda}{D_e(\lambda)} \quad (G.5)$$

$$\Pi_z = u(1-n^2) \int_{-\infty}^\infty H_1(\lambda R \sin\theta) \cdot e^{-\mu R \cos\theta} \frac{\cos\phi \cdot \lambda^2 d\lambda}{D_e(\lambda) \cdot D_m(\lambda)} \quad (G.6)$$

Making use of λ -plane to α -plane transformation i.e.,
 $\lambda = k \sin \alpha$, radical factors μ and μ_e become as,

$\mu = -\sqrt{k^2 \sin^2 \alpha - k^2} = -jk \cos \alpha$ (-ve sign is chosen in order to satisfy conditions (47)), and

$$\mu_e = jk \sqrt{n^2 - \sin^2 \alpha} .$$

Substituting above in (30) and (31) one obtains,

$$D_e(\lambda) = -jk(\cos \alpha + j\sqrt{n^2 - \sin^2 \alpha} \cdot \cot kB \sqrt{n^2 - \sin^2 \alpha}) , \quad (G.7)$$

$$D_m(\lambda) = jk(-n^2 \cos^2 \alpha + j\sqrt{n^2 - \sin^2 \alpha} \cdot \tan kB \sqrt{n^2 - \sin^2 \alpha}) . \quad (G.8)$$

By using λ to α -plane transformations integral (G.5) can be written as,

$$\Pi_x = u \int_{-\infty}^{\infty} H_0(R \sin \theta \sin \alpha) \cdot e^{jkR \cos \alpha \cos \theta} \frac{k^2 \cos \alpha \sin \alpha}{D_e(\alpha)} d\alpha . \quad (G.9)$$

For far zone fields $Rk \gg 1$ and $\theta < 90^\circ$, therefore by using large argument asymptotic approximation for Hankel function [33], (G.9) becomes as,

$$\Pi_x \approx u \int_{-\infty}^{\infty} f(\alpha) \cdot e^{jkR \cos(\alpha - \theta)} d\alpha , \quad (G.10)$$

where

$$f(\alpha) = \frac{k \cos \alpha \sin \alpha}{D_e(\alpha)} \cdot e^{-j\pi/4} \cdot \sqrt{\frac{2}{R \sin \alpha}} . \quad (G.11)$$

For $Rk \gg 1$, using stationary phase approximation asymptotic solution of (G.10) is given by,

$$\Pi_x \approx \left[\frac{2}{Rk} \right]^{\frac{1}{2}} \cdot f(\theta) \cdot e^{jkR + j\pi/4} , \quad (G.12)$$

where $\alpha = \theta$ is the stationary point.

Substituting (G.11) in (G.12) and simplifying one obtains,

$$\Pi_x = u \cdot \frac{1}{(1 + j \frac{S_{nt}}{\cos \theta} \cot(kB \cdot S_{nt}))} \cdot \frac{e^{jkR}}{R} \quad (G.13)$$

where

$$S_{nt} = \sqrt{n^2 - \sin^2 \theta}, \quad (G.14)$$

and

$$R = r - x' \sin \theta \cdot \cos \phi - y' \cdot \sin \theta \cdot \sin \phi - B \cdot \cos \theta. \quad (G.15)$$

Similarly by following the above step one can show that Π_z is given by,

$$\Pi_z = 2 \frac{(1-n^2)}{n^2} \frac{u \cdot \tan \theta \cdot \cos \phi}{\left[1-j \frac{S_{nt}}{\cos \theta} \tan(kB \cdot S_{nt})\right] \left[1+j \frac{S_{nt}}{\cos \theta} \cot(kB \cdot S_{nt})\right]} \frac{e^{jkR}}{R}. \quad (G.16)$$

For a linear current density $J_x(x', y') \cdot \hat{x}$ on the substrate one has,

$$\Pi = \int_{S'} J_x(x', y') \left[\Pi_x(r, r') \hat{x} + \Pi_z(r, r') \hat{z} \right] dx' dy' \quad (G.17)$$

The θ and ϕ component of Hertz vector Π can be written as,

$$\Pi_\theta = \int_{S'} J_x(x', y') \left[\Pi_x \cdot \cos \theta \cdot \cos \phi - \Pi_z \cdot \sin \theta \right] dx' dy', \quad (G.18)$$

$$\Pi_\phi = \int_{S'} J_x(x', y') \cdot -\Pi_x \cdot \sin \phi \cdot dx' dy'. \quad (G.19)$$

Substituting (G.13) and (G.16) in (G.18) and (G.19), and making use of (G.15) one gets,

$$\Pi_{\theta} = u \cdot \frac{e^{jkr}}{r} \cdot \frac{e^{-jkB\cos\theta}}{D_e(\theta, \phi)} \cdot \cos\phi \cdot \left[\cos\theta + \frac{(n^2 - 1) \cdot \tan\theta \cdot \sin\phi}{D_m(\theta, \phi)} \right] I_x, \quad (G.20)$$

$$\Pi_{\phi} = -u \cdot \frac{e^{jkr}}{r} \cdot \frac{e^{-jkB\cos\theta}}{D_e(\theta, \phi)} \cdot \sin\phi \cdot I_x, \quad (G.21)$$

where I_x is defined by,

$$I_x = \int_{S'} J_x(x', y') \cdot e^{-jk(x' \cdot \sin\theta \cdot \cos\phi + y' \cdot \sin\theta \cdot \sin\phi)} dx' dy'. \quad (G.22)$$

The electric field at any point is given by,

$$\bar{E} = (k^2 + \nabla \cdot \nabla) \bar{\Pi}. \quad (G.23)$$

In the far zone (source free region), $\bar{\Pi}$ satisfies,

$$\nabla^2 \bar{\Pi} + k^2 \bar{\Pi} = 0$$

$$\text{or } \nabla^2 \bar{\Pi} = -k^2 \bar{\Pi}. \quad (G.24)$$

By using vector identity $\nabla \cdot \nabla \cdot \bar{\Pi} = \nabla \times \nabla \times \bar{\Pi} - \nabla^2 \bar{\Pi}$, and (G.24), (G.23) reduces to

$$\bar{E} = 2 \cdot k^2 \bar{\Pi} + \nabla \times \nabla \times \bar{\Pi}$$

$\nabla \times \nabla \times \bar{\Pi}$ contributes to the near zone fields. Therefore the far zone components of electric field are given by,

$$E_{\theta} = 2 \cdot k^2 \Pi_{\theta} \quad (G.25)$$

and

$$E_{\phi} = 2 \cdot k^2 \Pi_{\phi} \quad (G.26)$$

where Π_{θ} and Π_{ϕ} are defined by (G.18) and (G.19).

APPENDIX H

DYADIC GREEN'S FUNCTION:

A horizontal Hertzian dipole oriented in an arbitrary direction held at point (x', y', z') over a grounded dielectric substrate is shown in Fig. 1. The dyadic Green's function $\bar{G}(\mathbf{r}, \mathbf{r}')$ is given by [32],

$$\bar{G}(\mathbf{r}, \mathbf{r}') = \bar{G}_x(\bar{\mathbf{r}}, \bar{\mathbf{r}}') \hat{\mathbf{x}} + \bar{G}_y(\bar{\mathbf{r}}, \bar{\mathbf{r}}') \hat{\mathbf{y}} \quad (\text{H.1})$$

where $\bar{G}_x(\bar{\mathbf{r}}, \bar{\mathbf{r}}')$ and $\bar{G}_y(\bar{\mathbf{r}}, \bar{\mathbf{r}}')$ are vector Green's functions with the Hertzian dipole oriented in x -axis direction and y -axis direction, respectively. The vector Green's functions satisfy,

$$\nabla \times \nabla \times \bar{G}_x(\bar{\mathbf{r}}, \bar{\mathbf{r}}') - k^2 \bar{G}_x(\bar{\mathbf{r}}, \bar{\mathbf{r}}') = \delta(\bar{\mathbf{r}} - \bar{\mathbf{r}}') \hat{\mathbf{x}} \quad (\text{H.2})$$

$$\nabla \times \nabla \times \bar{G}_y(\bar{\mathbf{r}}, \bar{\mathbf{r}}') - k^2 \bar{G}_y(\bar{\mathbf{r}}, \bar{\mathbf{r}}') = \delta(\bar{\mathbf{r}} - \bar{\mathbf{r}}') \hat{\mathbf{y}} \quad (\text{H.3})$$

The vector Green's functions are further related with their corresponding Hertz vector potentials by,

$$\bar{G}_x(\bar{\mathbf{r}}, \bar{\mathbf{r}}') = (1 + \frac{1}{k^2} \nabla \cdot \nabla) \bar{\Pi}_x, \quad (\text{H.4})$$

and

$$\bar{G}_y(\bar{\mathbf{r}}, \bar{\mathbf{r}}') = (1 + \frac{1}{k^2} \nabla \cdot \nabla) \bar{\Pi}_y, \quad (\text{H.5})$$

where Π_x and Π_y are Hertz vector potentials for Hertzian dipoles oriented in $\hat{\mathbf{x}}$ and $\hat{\mathbf{y}}$ directions. In Section 2.1, Hertz vector potential Π_x is derived and is given by (for

region I), as

$$\bar{\Pi}_x = \Pi_{xx} \hat{x} + \Pi_{zx} \hat{z} , \quad (H.6)$$

where

$$\Pi_{xx} = 2u \int_0^\infty J_0(\rho\lambda) \cdot e^{-\mu(z-B)} \frac{\lambda d\lambda}{D_e(\lambda)} \quad (H.7)$$

and

$$\Pi_{zx} = -2(n^2-1)u \int_0^\infty J_1(\rho\lambda) \cdot \cos\phi \cdot e^{-\mu(z-B)} \frac{\lambda^2 d\lambda}{D_e(\lambda) \cdot D_m(\lambda)} . \quad (H.8)$$

By inspection, the Hertz vector potential for a Hertzian dipole pointing in the y-direction is given by,

$$\bar{\Pi}_y = \Pi_{yy} \hat{y} + \Pi_{zy} \hat{z} , \quad (H.9)$$

where

$$\Pi_{yy} = 2u \int_0^\infty J_0(\rho\lambda) \cdot e^{-\mu(z-B)} \frac{\lambda d\lambda}{D_e(\lambda)} \quad (H.10)$$

and

$$\Pi_{zy} = -2(n^2-1)u \int_0^\infty J_1(\rho\lambda) \cdot \sin\phi \cdot e^{-\mu(z-B)} \frac{\lambda^2 d\lambda}{D_e(\lambda) \cdot D_m(\lambda)} . \quad (H.11)$$

Substituting (H.4) and (H.5) back in (H.1), one obtains the dyadic Green's function (for region I) as,

$$\bar{G}(\vec{r}, \vec{r}') = (1 + \frac{1}{k} \nabla \cdot \nabla) (\bar{\Pi}_x \hat{x} + \bar{\Pi}_y \hat{y}) \quad (H.12)$$

where $\bar{\Pi}_x$ and $\bar{\Pi}_y$ are defined by (H.6) and (H.9), respectively.

APPENDIX I
COMPUTER PROGRAM FOR CURRENT DISTRIBUTION AND INPUT
IMPEDANCE OF A PRINTED DIPOLE:

This program has been used to compute input impedance and current distribution of a printed wire dipole. The only additional subroutines required but not included here, are MMBSJ0 and MMBSJ1. These subroutines are available from IMSL subroutine package.

```

C THIS PROGRAM COMPUTES CURRENT DISTRIBUTION & INPUT IMPEDANCE OF A
C PRINTED WIRE DIPOLE USING SINUSOIDAL EXPANSION FUNCTIONS AND
C GALERKIN'S METHOD.
C WH=RADIUS OF THE WIRE.      DL=LENGTH OF THE WIRE DIPOLE
C ND=TOTAL NUMBER OF SEGMENTS OF THE WIRE DIPOLE.
C A=CONSTANT DEFINED BY EQUATION (52)
C B=THICKNESS OF THE SUBSTRATE.   DC=DIELECTRIC CONSTANT OF THE
C SUBSTRATE.          LENO=SURFACE WAVE MODE.
C THIS PROGRAM TAKES INTO ACCOUNT ONLY ONE SURFACE WAVE MODE.
C ALL DIMENSIONS ARE NORMALIZED WITH RESPECT TO FREE SPACE
C NDN DEFINES THE POSITION OF THE GENERATOR ON THE WIRE DIPOLE.
C COMPLEX*16 IPXX,IPZZ,WX,WZ,WI,U,DETH,Z,ZIN
REAL*8 XF,X1,X2,DC,PI,AK,B,A,LEMO,SEGm,X,DL,AH,AKS,WH,YY,AS,XL,TBT
1,XN,YN,XT,XC,AKNS,ZR,ZH,ZN,ZL,ZT,ZC,XB,XP,ZU,CUR,AKN,ARG,TCOS
DIMENSION X(49),WX(49),WZ(49),WI(49),Z(47,47),CUR(11),WI(11),MI(11
1)
COMMON WH,YY,AK,A,B,DC,PI,XL,XN,YN,IT,IC,AKS,ZR,ZH,ZN,ZL,ZT,ZC,AKN
1S,XB,ZB,TBT,SEGm,AKN,AH
TBT=-66666666666667D+0
LEMO=0.713081200575861D+1
WH=0.0001D0
DL=0.5UD0
A=80.0D0
AH=A/2.
ND=20
NDL=ND-1
NDW=ND/2
PI=3.14159265358979D0
DC=3.25D0
B=0.1016D0
AK=PI*2.D0
SEGm=DL/ND
AKN=AK*DSQRT(DC)

```

Appendix I (continued)

```

AKS=AK**2
AKNS=AKS*DC
YY=WH**2
AS=A**2
XL=(1.D0+DC)/4.D0
XW=(1.D0+DC**2)/16.D0
YN=(1.D0+DC**3)/32.D0
XP=(DC*XH-(DC-1.D0)/32.D0)*0.625D0
XT=(XL**2+XH)*AKS
XC=((XT+XH*AKS)*XL+XH*AKS)*AKS
XB=AKS*(YC*XL+(XL*(XL*XN+YN)+XH**2+XP))*AKS**2)
ZR=(DC**2+6.D0*DC+1.D0)/(4.D0*(DC+1.D0))
ZN=XH-DC/8.D0
ZN=XN-DC*XL/8.D0
ZL=ZR-0.5D0
ZT=(ZR*ZL+ZH-.125D0)*AKS
ZU=(XH*XL*(DC-1.D0)*5.D0-DC**2/32.D0-DC*XN)/4.D0
ZC=(ZN-.0625E0*ZL*(ZR**2+ZH)+ZR*(ZN-0.125D0))*AKS**2
ZB=((2.D0*ZN+ZH*ZB)*ZL+ZU-ZR/16.D0+ZN/2.D0)*AKS+ZT*(ZH**2+ZH))*AK
1S**2
ND=ND+1
DO 1 I=1,ND
  X(I)=(I-1)*SEGM
  WRITE(6,40) DC,B,WH,DL,ND
  40 FORMAT('0',5X,F6.3,5X,F5.4,5X,F5.2,5X,I3)
  ARG=AK*SEGM
  U=(0.D0,-0.3D0)/DSIN(ARG)**2
  TCO=2.D0*DCOS(ARG)
  NP=0
  X1=X(1)
  X2=X(2)
  NQ=0
  XP=X(.30)
  CALL VOLT(X1,X2,XF,IPXX,IPZZ,IPIZ,NQ,NP)

```

Appendix I (continued)

```

WX(30)=IPXX
WZ(30)=IPZZ
WI(30)=IPIZ
GO TO 420
DO 2 I=31,NDD
NQ=1
IF(I.GT.4) NQ=0
XP=X(I)
IF(I-NDD) 11,22,22
NP=1
CALL VOLT(X1,X2,XP,IPXX,IPZZ,IPIZ,NQ,NP)
WX(I)=IPXX
WZ(I)=IPZZ
WI(I)=IPIZ
N=2
DO 3 I=2,ND
J=I-1
Z(J,1)=WX(I+1)+WX(I-1+N)-TCOS*WX(I)-WZ(I-1+N)+TCOS*WZ(I
1)+AK*WI(I)
Z(1,J)=Z(J,1)
WRITE(7,29) Z(1,J)
N=0
FORMAT(T6,D21.14,T32,D21.14)
WRITE(6,39) (Z(I,I),I=1,NDL)
GO TO 420
DO 4 I=2,NDL
N=NDL-I+2
LA=I-2
DO 4 J=2,N
KA=J-2
Z(I+KA,J)=Z(1,1+LA)
Z(J,I+KA)=Z(1,1+LA)
CALL MINVCD(Z,NDL,NDL,DETH,NI,MI)
DO 5 I=1,NDL

```

Appendix I (continued)

```

5      CUB(I)=CDABS(Z(I,NDN))
      WRITE(6,39)CUB
      ZIN=1.D0/Z(NDN,NDN)
      WRITE(6,39)ZIN
      WRITE(6,39)(Z(NDN,I),I=1,NDL)
      FORMAT(2X,3(1X,D16.9,1X,D16.9))
      STOP
      END

C      **** FOLLOWING PROGRAM COMPUTES THE MATRIX ELEMENTS ZIJ OF THE
C      IMPEDANCE MATRIX
      SUBROUTINE VOLT(X1,X2,XF,IPXX,IPZZ,IPIZ,NQ,NP)
      COMPLEX*16 IPXX,IPZZ,IPIZ,QXX,QZZ,QIZ
      REAL*8 X1,X2,XF,WH,YI,AK,A,B,DC,PI,XL,IN,IN,XT,YC,AKS,ZR,ZH,ZN,ZL,
      1ZR,ZC,AKNS,XB,ZB,TBT,SEGm,LEHO,LENl,LEMf,QXI,QZI,QII,D,D1,D2,D3,TA
      1ILY,TAILz,TAIlA,AKN,SUM1,SUM2,SUM3,LEMx
      COMMON WH,YI,AK,A,B,DC,PI,XL,YN,YN,XT,YC,AKS,ZR,ZH,ZL,ZT,ZC,AKN
      1S,XB,ZB,TBT,SEGm,AKN,AH
      LEHO=0.'13081200575861D+1
      D=0.005D0
      D1=0.20D0
      D2=0.15D0
      D3=0.10D0
      SUM1=0.D0
      SUM2=0.D0
      SUM3=0.D0
      LENl=0.D0
      LEMf=AK-0.2D0
      L=LEMf/0.05D0
      NX=L*2
      CALL QUASIM(X1,X2,XP,LENl,LEMf,NX,QXX,QZZ,QIZ,QXI,QZI,-1,NP)
      SUM1=QX1
      SUM2=QZI

```

Appendix I (continued)

```

SUM3=QII
IPXX=QIX
IPIZ=QIZ
IPZZ=QZZ
LEMI=LEHF
LEMF=A
L=(LEMF-LEMI)/D
NI=L*2
CALL QUASMX(X1,X2,XF,LEM1,LEM2,NX,QXX,QZZ,QIZ,QI1,QI1,-1,NP)
SUM1=QXI+SUM1
SUM2=QZI+SUM2
SUM3=QII+SUM3
IPXX=QXI+IPXX
IPIZ=QIZ+IPIZ
IPZZ=QZZ+IPZZ
LEMI=LEHF
LEMF=A KN-1. D-6
L=(LEMF-LEMI)/0.05D0
NX=L*2
CALL SURPOL(X1,X2,XF,LEM1,LEM2,NX,QXX,QZZ,QIZ,QI1,QI1,LEM0,NP)
SUM1=QXI+SUM1
SUM2=QZI+SUM2
SUM3=QII+SUM3
IPXX=IPXX+QXI
IPIZ=IPIZ+QIZ
IPZZ=IPZZ+QZZ
LEMI=LEHF
LEMF=A
L=(LEMF-LEMI)/D2
NX=L*2
LEHX=A*XF
IP(LENX,LT,20,D0) GO TO 3
LEMF=AH
L=(LEMF-LEMI)/D2
NX=L*2

```

Appendix I (continued)

```

      CALL QUASMX(X1,X2,XP,LEMI,LEMF,NX,QXX,QZZ,QXI,QZI,QII,+1,NP)
      SUM1=QXI+SUM1
      SUM2=QZI+SUM2
      SUM3=QII+SUM3
      IPXX=IPXX+QXX
      IPIZ=IPIZ+QIZ
      IPZZ=IPZZ+QZZ
      LEMI=LEMF
      LEMP=A
      L=(A-LEMI)/D3
      NX=L*2
      CALL QUASMX(X1,X2,XP,LEMI,LEMF,NX,QXX,QZZ,QXI,QZI,QII,+1,NP)
      SUM1=QXI+SUM1
      SUM2=QZI+SUM2
      SUM3=QII+SUM3
      IPXX=IPXX+QXX
      IPIZ=IPIZ+QIZ
      IPZZ=IPZZ+QZZ
      CALL QUATXX(X1,X2,XP,TAIX,TAIZ,TAII,NIQ)
      IPXX=IPXX+TAIX+SUM1
      IPZZ=(DC-1.D0)*(IPZZ+(TAIZ+SUM2)/(DC+1.D0))
      IPIZ=(DC-1.D0)*(IPIZ+(TAII+SUM3)/(DC+1.D0))
      WRITE(6,39) IPXX,IPZZ,IPIZ
      FORMAT('0',5X,3(1X,D16.9,1X))
      RETURN
      END
      ..
      ..
      ..
      C
      SUBROUTINE QUASMX(X1,X2,XP,LEMI,LEMF,NX,QXX,QZZ,QXI,QZI,QII,N,N
     1F)
      C
      COMPLEX*16 QXX,QZZ,MU,MUE,MUEB,TANT,F,FX,FF,FZ,FI,SUMX,SUMZ,SUM
      1I
      REAL*8 B,DC,A,PI,LEN,LEMI,LEMF,LEN1,LEN2,F1,F2,F3,F4,F5,X1,X2,XR,TBT
      1,SUM3,SUM4,SUM5,H,XL,XH,XN,YI,AKS,AKNS,ZR,ZN,ZL,ZC,ZT,XB,

```

Appendix I

(continued)

```

1ZB,QXI,QZI,QII,WH,SEGMM,LEMS
COMMON WH,YY,AK,A,B,DC,PI,XL,XN,XR,XN,ZL,ZT,ZC,AKN
1S,XB,ZB,TBT,SEGMM
LEM=LENM
H=(LEMF-LEM)/NX
SUMX=(0.0D0,0.0D0)
SUMI=(0.0D0,0.0D0)
SUMZ=(0.0D0,0.0D0)
SUM3=0.0D0
SUM4=0.0D0
SUM5=0.0D0
NX=NX+1
DO 3 I=1,NXX
LEMS=LEM**2
II=I+1
NL=I/NAX
NL=(NXX-I)/NX
LL=HL+NL
L=II/2
K=L*2
KK=2*(II-K+1)/(I+LL)
CALL INTEL(X1,X2,XF,LEM,F1,F2,F3,F4,F5,NP)
NU=CDSQRT((LEMS-AKS)*(1.0D0,0.0D0))*N
NUE=(0.0D0,1.0D0)*CDSQRT((LEMS-AKNS)*(1.0D0,0.0D0))
MUEB=MUE*B
TANT=CD SIN(MUEB)/CDCOS(MUEB)
F=LEM/(NU+NU/E*TANT)
PP=P*NU/(NU*DC-MUE*TANT)
PY=F*F1
PI=PF*P2
F2=PP*P1
LEM=LEN+H
SUMI=SUMI+PI*K
SUMI=SUMI+F1*K
SUMZ=SUMZ+F2*K

```

Appendix I (continued)

```

      SUM4=SUM4+P4*KK
      SUM5=SUM5+P5*KK
      QXX=SUMX*H*TBT
      QIZ=SUMI*H*TBT
      QZZ=SUMZ*H*TBT
      QII=SUMJ*H/3.D0
      QXI=SUM4*H/3.D0
      QZI=SUM5*H/3.D0
      RETURN
END

C ..... THE FOLLOWING PROGRAM COMPUTES PRINCIPAL VALUE INTEGRATION DUE TO
C ..... SURFACE WAVE POLE
C ..... SUBROUTINES URPOL(X1,X2,XF,LEN1,LEN2,LEN3,LEN4,LEN5,LEN6,LEN7,LEN8)
C ..... 10,MP)
COMPLEX*16 QXX,QZZ,QIZ,IOTA
REAL*8 AK,A,B,PI,DC,AKS,LENP,LEMO,LENXP,LEN,LENX,F1,F2,F3,F4,F5,FL
1DP,AKNS,YY,IL,IN,XN,XT,XC,ZR,ZM,ZN,ZL,ZT,ZC,LEM1,MU,MUE,TANT,FP,FP
11,FP2,FL,SUM3,SUM4,SUM5,SUMX,SUMZ,SUMI,QXI,QZI,QII,XB,ZB,WH,TET,SE
1GN,X1,X2,XF,HUEB
COMMON WH,Y,Y,AK,A,B,DC,PI,XL,XM,XN,XT,XC,AKS,ZR,ZH,ZN,ZL,ZT,ZC,AKN
15,XB,ZB,TBT,SGNM
IOTA=DLOG((LENP-LEMO)/(LEMO-LEM1))+(0.D0,1.D0)*PI
CALL INTEL(X1,X2,XF,LEMO,F1,F2,F3,F4,F5,NP)
MU=DSQRT(LEMO**2-AKS)
HUE=DSQRT(AKNS-LEMO**2)
HUEB=HUE*B
TANT=DSIN(MUEB)/DCOS(MUEB)
FP=MU**2*MUE/(MU+MUE/TANT)*(MUE*DC+MU*TANT*B*MUE*(1.D0+TANT**2
1)) )
FP1=FP*F1
FP2=FP*F2
LEN=LEM1
H=(LENP-LEM1)/NT

```

Appendix I (continued)

```

NTT=NTT+1
SUM3=0.D0
SUM4=0.D0
SUM5=0.D0
SUMX=0.D0
SUMZ=0.D0
SUMI=0.D0
DO 4 I=1,NTT
  II=I+1
  NL=I/NTT
  ML=(NTT-I)/NT
  L=NL+ML
  K=I*I/2
  KK=2*(II-K+1)/(1+LL)
  CALL INTEL(X1,X2,XP,LEM,P1,F2,F3,F4,F5,NP)
  HU=DSQRT(LEM**2-ARS)
  HUE=DSQRT(ANS-LEM**2)
  HUEB=HUE*B
  TANT=DSIN(HUEB)/DCOS(HUEB)
  PLDP=LEM-LEM0
  P=LEM/(NU+NU/TANT)
  P2=P*HU*PLDP/(NU*DC-HUE*TANT)
  FX=P1*P
  P1=(PP*P2-PP2)/PLDP
  P2=(PP*P1-PE1)/PLDP
  SUMX=SUMX+PY*KK
  SUMI=SUMI+PI*KK
  SUMZ=SUMZ+F2*KK
  SUM3=SUM3+F3*KK
  SUM4=SUM4+F4*KK
  SUM5=SUM5+F5*KK
  LEM=LEM+H
  QXX=SUMX*H*TBT
  QIZ=SUMI*H*TBT+2*PP2*IOTA

```

Appendix I (continued)

```

OZZ=SUM2*H*TBT+2*PP1*IOTA
QII=SUM3*H/3.D0
QXI=SUM4*H/3.D0
QZI=SUM5*H/3.D0
RETURN
END

```

C C C

```

C
SUBROUTINE QUATXX(X1,X2,XP,TAIX,TAIZ,TAII,WMQ)
REAL*8B,DC,AK,A,PI,YY,XL,XN,XT,YC,SUM1,SUM2,TAII1,TAII2,
1BT,XX,BJ0,BJ1,BJ2,BJ3,AKS,BJ4,BJ5,HUBSJ0,HUBSJ1,AKNS,ZR,ZN,ZL,Z
1T,ZC,ARG,ROW,XB,ZB,ROWS,ARGS,WH,SEGM,X1,X2,XP,H,SUM3,SELP,SINE,AKH
COMMON WH,YY,AK,A,B,DC,PI,XL,XN,XM,XC,AKS,ZR,ZN,ZL,ZT,ZC,AKN
1S,XB,ZB,TBT,SEGK
SELP=0.D0
NX=50
NF=NX/2
H=SEGK+2.D0/NX
AKH=AK*H
NXK=NK+1
SUM1=0.D0
SUM2=0.D0
SUM3=0.D0
XX=XP-X2-SEGN
DO 40 I=1,NX
NA=I-NP-1
IP(NA)=1,1,2
SINE=DSIN(AKH*(NX-I))
1 GO TO 3
2 SINE=DSIN(AKH*(NX-I))
3 II=I+1
NL=I/NX
NL=(NX-I)/NX
LL=NL+ML

```

Appendix I (continued)

```

L=LI/2
K=2*L
KK=2*(LI-K+1)/(1+LL)
ROWS=XX**2+YY
ROW=DSQRT(ROWS)
ARG=A*ROW
ARGS=ARG**2
BJ0=MHSJ0(ARG,IER)
BJ1=MHSJ1(ARG,IER)
BJ2=2.D0*BJ1/ARG-BJ0
BJ3=4.D0*BJ2/ARG-BJ1
BJ4=6.D0*BJ3/ARG-BJ2
BJ5=8.D0*BJ4/ARG-BJ3
TAILX=ROW*AKS*(XL*(BJ0/ARG-BJ1-1.D0)+ROWS*(XT*(BJ0/(ARGS*ARG)-BJ1*
1(1.D0/ARGS-TBT)-BJ2/ARG*(BJ3+1.D0)/3.D0)/3.D0+ROWS*XC*(BJ0/(ARGS* *
12*ARG)-(BJ1/ARGS**2-BJ2/(ARGS*ARG)-BJ3/ARGS-BJ4/(3.D0*ARG)+(BJ5+2.*
1D0*(BJ3+BJ1)+1.D0)/15.D0)/3.D0)/5.D0)+1-NQ)/ROW
TAILZ=ROW*AKS*(ZL*(BJ0/ARG-BJ1-1.D0)+ROWS*(ZT*(BJ0/(ARGS*ARG)-BJ1*
1(1.D0/ARGS-TBT)-BJ2/ARG*(BJ3+1.D0)/3.D0)/3.D0+ROWS*ZC*(BJ0/(ARGS* *
12*ARG)-(BJ1/ARGS**2-BJ2/(ARGS*ARG)-BJ3/ARGS-BJ4/(3.D0*ARG)+(BJ5+2.*
1D0*(BJ3+BJ1)+1.D0)/15.D0)/3.D0)+1-NQ)/ROW
SUM1=SUM1+KK*TAILX*SINE
CALL QUATDI(X1,X2,XX,TAILL,NQ)
IF(NQ) 20,20,10
CALL SING(X1,X2,XX,SELF)
10 TAILI=TAILI+SELF
20 SUM3=SUM3+KK*TAILI*SINE
SUM2=SUM2+KK*TAIL2*SINE
40 XX=XX+H
SELF=0.D0
60 IF(NQ) 30,30,60
XX=X2-XF
AKH=XF-SEGK
CALL SING(AKH,XF,XX,SELF)
TAILX=SUM1*H/3.D0+SELF
30

```

Appendix I (continued)

```

TAILLZ=SUM 2*H/3*D0+SELF
TAILLI=SUM 3*H/3*D0
RETURN
END
C
C
SUBROUTINE QUATDI (X1,X2,XX,TAILLI,WQ)
REAL*8B,DC,AK,A,PI,YY,ARG,XL,XN,XT,XC,AKS,ROH,ARGS,XX,SUM,TAILLI
1,TBT,BJ1,BJ2,BJ3,BJ4,BJ5,ROWS,F1,F2,LX,RX,X1,X2,ZL,ZT,ZC,ZR,ZN,ZN,
1MMBSJ1,AKNS,XB,ZB,BJ0,MMBSJ0,SEGK,WH,XO
COMMON WH,YY,AK,A,B,DC,PI,XL,XM,XN,XT,XC,AKS,ZR,ZM,ZL,ZT,ZC,AKN
1S,XB,ZB,TBT,SEGK
NK=26
SUM=0.D0
X0=XX+X2
LX=X2
RX=X2
TAILLI=0.D0
H=(X2-X1)/NXX
NXX=NXX+1
DO 1 I=1,NXX
II=I+1
ML=I/NXX
NL=(NXX-I)/NXX
LL=NL+ML
L=II/2
K=2*L
KK=2*(II-K+1)/(1+LL)
ROWS=(X0-LX)**2+YY
ROW=DSCRT(ROWS)
ARG=A*ROW
ARGS=ARG**2
BJ0=MMBSJ0(ARGS,IER)
BJ1=MMBSJ1(ARGS,IER)
BJ2=2.D0*BJ1/ARGS-BJ0

```

Appendix I (continued)

```

BJ3=4. D0*BJ2/ARG-BJ1
BJ4=6. D0*BJ3/ARG-BJ2
BJ5=8. D0*BJ4/ARG-BJ3
F1=ROW*AKS*(ZL*(BJ0/ARG-BJ1-1.D0)+ROWS*(ZT*(BJ0/(ARGS*ARG)-BJ1*(1.
1D0/ARGS-TBT)-BJ2/ARG+(BJ3+1.D0)/3.D0)/3.D0+ROWS*ZC*(BJ0/(ARGS**2*A
1RG)-(BJ1/ARGS**2-BJ2/(ARGS*ARG)-BJ3/ARGS-BJ4/(3.D0*ARG)+(BJ5+2.D0*
1(BJ3+BJ1)+1.D0)/15.D0)/3.D0)+ (1-NQ)/ROW
ROWS=(X0-RX)**2+YY
ROW=DSQBT(ROWS)
ARG=A*ROW
ARGS=ARG**2
BJ0=MABSO(ARG,IER)
BJ1=MABSI1(ARG,IER)
BJ2=2.D0*BJ1/ARG-BJ0
BJ3=4.D0*BJ2/ARG-BJ1
BJ4=6.D0*BJ3/ARG-BJ2
BJ5=8.D0*BJ4/ARG-BJ3
F2=ROW*AKS*(ZL*(BJ0/ARG-BJ1-1.D0)+ROWS*(ZT*(BJ0/(ARGS*ARG)-BJ1*(1.
1D0/ARGS-TBT)-BJ2/ARG+(BJ3+1.D0)/3.D0)/3.D0+ROWS*ZC*(BJ0/(ARGS**2*A
1RG)-(BJ1/ARGS**2-BJ2/(ARGS*ARG)-BJ3/ARGS-BJ4/(3.D0*ARG)+(BJ5+2.D0*
1(BJ3+BJ1)+1.D0)/15.D0)/3.D0)+ (1-NQ)/ROW
TAILI=(F1+F2)*DSIN((LX-X1)*AK)
SUM=SUM+TAILI*KK
LX=LX-H
RX=RX+H
TAILI=SUM*B/3.D0
RETURN
END
.....
SUBROUTINE SINC(X1,X2,XX,F)
REAL*8 X1,X2,XP,WH,YI,SUB,F,XIR,XXL,RX,LX,H,AK,XX
COMMON WH,YY,AK
SUM=0.D0
XP=XX+X2
LX=X2

```

Appendix I (continued)

```

RY=X2
NX=120
NX=NX+1
H=(X2-X1)/NX
NX=NX+1
DO 1 I=1,NX
II=I+1
NL=I/NXX
NL=(NXX-I)/NX
LL=NL+NL
L=II/2
K=2*L
KK=2*(II-K+1)/(1+LL)
XXL=XP-LX
XXR=XP-RX
P=AK*DCOS(AK*(LX-X1))*DLOG((XXL+DSQRT(XXL**2+YY))/(
12+YY)))
SUM=SUM+KK*P
LX=LX-H
RX=RX+H
P=SUM*H/3.D0
RETURN
END
.....
```

F77

```

SUBROUTINE MINVCD(A,IA,MA,DETA,IR,IC)
IMPLICIT REAL*8(A-H,O-Z)
COMPLEX*16A(IA,IA),PIV,DETA,TEMP,PIV1
DIMENSION IR(MA),IC(MA)
DO 11 I=1,MA
IR(I)=0
IC(I)=0
DETA=(1.0D0,0.0D0)
S=0.0D0
R=MA

```

Appendix I (continued)

```

2      CALLSUBCD(A,IA,IA,MA,IR,IC,I,J)
      PIV=A(I,J)
      DETA=PIV*DETA
      Y=CDABS(PIV)
      IF(Y.EQ.0.) GOTO17
      IR(I)=J
      IC(J)=I
      PIV=(1.0D0,0.0D0)/PIV
      A(I,J)=PIV
      DO5K=1,MA
      IF(K.NE.J)A(I,K)=A(I,K)*PIV
      DO9K=1,MA
      IF(K.EQ.I)GOTO9
      PIV1=A(K,J)
      DO8L=1,MA
      IF(L.NE.J)A(K,L)=A(K,L)-PIV1*A(I,L)
      CONTINUE
      DO11K=1,MA
      IF(K.NE.I)A(K,J)=-PIV*A(K,J)
      S=S+1.0D0
      IF(S.LT.B)GOTO2
      DO16I=1,MA
      K=IC(I)
      B=IR(I)
      IF(K.EQ.I)GOTO16
      DETA=-DETA
      DO14L=1,MA
      TEMP=A(K,L)
      A(K,L)=A(I,L)
      A(I,L)=TEMP
      DO15L=1,MA
      TEMP=A(L,N)
      A(L,B)=A(L,I)
      A(L,I)=TEMP
      IC(B)=K

```

14

15

Appendix I (continued)

```

IR (K)=N
CONTINUE
RETURN
WRITE(6,18)
FORMAT(' MATRIX IS SINGULAR')
RETURN
END
SUBROUTINE SUBACD(A,IA,JA,NA,IR,IC,I,J)
IMPLICIT REAL*8 (A-H,O-Z)
COMPLEX*16 A (IA,JA)
DIMENSION IR (NA), IC (NA)
I=0
J=0
TEST=0.D0
DO 5 K=1,NA
  IF (IR (K) .NE. 0) GO TO 5
DO 4 L=1,NA
  IF (IC(L) .NE. 0) GO TO 4
X=CDABS (A (K,L))
IF (X.LT.TEST) GO TO 4
I=K
J=L
TEST=X
CONTINUE
RETURN
END
SUBROUTINE INTEL(X1,X2,XP,LBN,P1,P2,P3,P4,P5,NP)
REAL*8 P1,P2,P3,P4,P5,SUM1,SUM2,SUM3,SUM4,SUM5,SUM6,SUM7,BJ,HUBSJO
1,LBN,B,DC,AK,A,AKS,PI,YY,XL,XN,XH,XT,XC,
1XF,SEGm,TBT,H,ROW,ROW1,ROW2,X1,X2,ROW,SINE,XB,ZB,LENX,ARG
DIMENSION BJ (70), ROD (70), SINE (25)
COMMON WH,YY,AK,A,B,DC,PI,XL,XN,XH,XN,XT,YC,AKS,ZR,ZN,ZL,ZT,ZC,AKN,
1,XB,ZB,TBT,SEGm

```

Appendix I

(continued)

```

LENX=LEN*DSQRT(XF**2+YY)
NF=06
IF (LENX-5.D0) 1,1,2
IF (LENX-15.D0) 3,3,4
NP=12
GO TO 1
IF (LENX-25.D0) 5,5,6
NF=16
GO TO 1
NF=14
NFD=2*NF
NXI=NFD+1
SUM1=0.D0
SUM2=0.D0
SUM3=0.D0
SUM4=0.D0
SUM5=0.D0
H=SEGN/NF
DO 7 I=1,NFD
ROW=(XF+SEGN-H*(I-1))**2+YY
ROD(I)=ROW
ARG=LEN*DSQRT(ROW)
BJ(I)=NNBSJ0(ARG,IEB)
NFD=NFD+1
DO 8 J=1,NXX
II=J+NFD
ROW=(XF-SEGN-H*(J-1))**2+YY
ROD(II)=ROW
ARG=LEN*DSQRT(ROW)
BJ(II)=NNBSJ0(ARG,IEB)
SINE(NF+1)=0.D0
DO 9 K=1,NF
SINE(K)=DSIN(ARK*(X2-H*(K-1)))
NXX=NXX+NF
MM=+1

```

Appendix I (continued)

```

DO 10 I=2,NED
KK=J+NN
NN=-NN
NA=I-NPP
N=-1
1P (NA) 19,19,29
N=1
NC=NA*M+1
NB=NXP+1-I
ROW=ROD(NB)
P1=BJ(NB)*SINE(NC)
P4=-(1.00-ROW*AKS*(XL-ROW*(25.*XT-ROW*XC)/225.00))*P1
P5=-(1.00-ROW*AKS*(ZL-ROW*(25.*ZT-ROW*ZC)/225.00))*P1
SUMJ=0. DO
SUMF=0. DO
NN=1
JC=1
1P (NP) 100,100,200
DO 11 J=1,NF
NN=-NN
N1=NXP+2-J-I
N2=NXP+J-I
ROW1=ROD(N1)
ROW2=ROD(N2)
P2=(BJ(N1)+BJ(N2))*SINE(J)
P3=-P2+(ROW1*(ZL-ROW1*(25.*ZT-ROW1*ZC)/225.)*BJ(N1)+ROW2*(ZL-ROW2*
1(25.*ZT-ROW2*ZC)/225.)*BJ(N2))*AKS*SINE(J)
SUMJ=SUMJ+P2*JC
SUMF=SUMF+P3*JC
JC=3-NN
11
P2=SUMJ*SINE(NC)
P3=SUMP*SINE(NC)
SUM1=SUM1+P1*KK
SUM2=SUM2+P2*KK
SUM3=SUM3+P3*KK
200

```

Appendix I (continued)

```
      SUM4=SUM4+P4*KK  
      SUM5=SUM5+P5*KK  
      P1=SUM1*H/3. DO  
      P2=SUM2*H**2/9. DO  
      P3=SUM3*H**2/9. DO  
      P4=SUM4*H/3. DO  
      P5=SUM5*H/3. DO  
      RETURN  
      END  
//GO.FT07F001 DD SYSOUT=B,SPACER=(TRK,(1,1),BLSE),DCB=HALFPTRK
```

APPENDIX J

COMPUTER PROGRAM FOR MUTUAL IMPEDANCE BETWEEN TWO PRINTED DIPOLES:

This program makes use of the impedance matrix [z] data generated by the program listed in Appendix I, to compute the mutual impedance between two broadside printed wire dipoles. The program is written in Fortran IV.

```

C THE FOLLOWING PROGRAM COMPUTES MUTUAL IMPEDANCE BETWEEN TWO
C BROADSIDE PRINTED WIRE DIPOLES.
C ND=NUMBER OF SEGMENTS.
C COMPLEX*16 Z,ZIN,DETM,ZINO,ZO,Z12,V
REAL*8 CUR,DL
DIMENSION Z(18,18),ZO(17,17),CUR(18),NI(18),MI(18),V(18)
ND=10
NDR=ND/2
NDP=ND+NDW-1
ND2=ND-1
NDL=2*ND-2
ND0=NDL-1
DL=0.5 D0*ND/20
DO 3 I=1,NDL
RBAD(S,29) Z(I,I)
Z(I,1)=Z(1,I)
DO 4 I=2,NDL
N=NDL-I+2
LA=I-2
DO 4 J=2,N
KA=J-2
Z(I+KA,J)=Z(1,1+LA)
Z(J,I+KA)=Z(1,1+LA)
DO 5 J=2,ND2
N=NDL-J+1
DO 5 I=ND,N
KA=J+ND-1
LA=J+I-ND
Z(LA,I)=Z(1,KA)
Z(I,LA)=Z(1,KA)
DO 7 I=1,NDO
DO 7 J=1,NDO
K=I/NDP
H=J/NDP
L=I+K

```

3 4 5

Appendix J (continued)

```
N=J+M  
7   ZO(I,J)=Z(L,N)  
    CALL MINVCD(Z,NDL,NDL,DETM,NI,MI)  
    CALL MINVCD(ZO,NDQ,NDQ,DETM,NI,MI)  
DO 8 I=1,NDL  
8   V(I)=Z(I,NDN)+Z(I,NDP)  
DO 6 I=1,NDL  
6   CUR(I)=CDABS(V(I))  
ZIN=1.D2/Z(NDN,NDN)  
WRITE(6,40) ZIN,ND,DL  
ZIN=1.D2/V(NDN)  
ZINO=1.D2/ZO(NDN,NDN)  
Z12=ZIN-ZINO  
WRITE(6,39) Z12,ZINO  
WRITE(6,39) V  
WRITE(6,39) (ZO(I,NDN),I=1,NDQ)  
WRITE(6,39) CUR  
39  SFORMAT(5X,3(D16.9,1X,D16.9,1X))  
40  FORMAT(5X,D14.7,3X,D14.7,7X,I3,7X,D14.7)  
29  FORMAT(T6,D21.14,T32,D21.14)  
STOP
```